ABSTRACT

Title of Document: RADIATIVE FLUXES AND ALBEDO FEEDBACK IN POLAR REGIONS.

Xiaolei Niu, Doctor of Philosophy, 2011

Directed By: Professor, Dr. Rachel T. Pinker,
Department of Atmospheric and Oceanic Science

The Arctic is experiencing an unprecedented increase in surface temperature and decrease in sea ice extent. Discussion as to the causes that contribute to the Arctic warming is still ongoing. The ice-albedo feedback has been proposed as a possible mechanism for polar amplification of such warming. It states that more open water leads to more solar heat absorption, which results in more ice melting and more open water. In order to study this relationship there is a need for accurate information on the solar heat input into the Arctic Oceans. I have developed and improved inference schemes for shortwave radiative fluxes that respond to the needs of Polar Regions utilizing most recent information on atmospheric and surface states. A Moderate Resolution Imaging Spectroradiometer (MODIS) approach has been optimized for Polar Regions and implemented at 1° for 2002-2010 and at 5-km for 2007. A methodology was developed to derive solar fluxes from the Advanced Very High Resolution Radiometer (AVHRR) and implemented at 0.5° for 1983-2006. Evaluation against ground measurements over land and ocean at high latitudes shows that the MODIS shortwave flux estimates are in best agreement with ground observations as compared to other available satellite and model products, with a bias of -3.6 Wm^{-2} and standard deviation of 23 Wm^{-2} at a daily time scale. The AVHRR estimates agree with ground observations with a bias of -4.7 Wm^{-2} and a standard deviation of 41 Wm^{-2} at a daily time scale. The ice-albedo feedback was evaluated by computing the solar heating into the Arctic Ocean using the improved satellite flux estimates. A growth at a rate of 2 %/year in the trend of solar heating for 2003-09 was found at a 75 % confidence level; the trend for 1984-2002 was only 0.2 %/year at a 99 % confidence level. The ice retreat is correlated to the solar energy into the ocean at 0.7 at a 75 % confidence level. An increase in the open water fraction resulted in a maximum 300 % positive anomaly in solar heating in 2007 located where the maximum sea ice retreat is.

RADIATIVE FLUXES AND ALBEDO FEEDBACK IN POLAR REGIONS

By

Xiaolei Niu

Dissertation submitted to the Faculty of the Graduate School of the
University of Maryland, College Park, in partial fulfillment
of the requirements for the degree of
Doctor of Philosophy
2011

Advisory Committee:
Professor Rachel T. Pinker, Chair
Professor James Carton
Senior Research Scientist Semyon Grodsky
Professor Robert Hudson
Professor Xin-Zhong Liang
Professor Stephen D. Prince, Dean’s Representative

Acknowledgements

First, I wish to thank my advisor, Professor Rachel T. Pinker, for her great guidance, continuous support and unending patience throughout my study at the Department of Atmospheric and Oceanic Science. I was fortunate to have her as a mentor. Without her help, this work would have never been completed.

I would also like to express my thanks to the members of our research group: Drs. Yingtao Ma, Maggie Wonsick, Donglian Sun, to Eric Nussbaumer, and Chuan Li, for their great help and valuable advice during the study. Very special thanks to Lin Zhu, Hua Chen, Ying Zhang, and Ji-Sun Kang and many other friends for their constant help and encouragement.

I thank Drs. Jim Carton, Semyon Grodsky, Robert Hudson, Xin-Zhong Liang, Stephen D. Prince, and Ross Salawitch for agreeing to serve on my prospectus and/or dissertation defense committees. I also would like to thank the excellent staff of the Department of Atmospheric and Oceanic Science, especially Tammy Hendershot, June Sherer, and Sonja Junek, for their unconditional support during my stay in the Department.

Finally I wish to thank my husband, Chengjun Sun, my mother-in-law, and my parents. They are an unending source of love, encouragement and support during my study.

Table of Contents

List of Acronyms

ADM	Angular Distribution Model
ARM	Atmospheric Radiation Measurement
AVHRR	Advanced Very High Resolution Radiometer
BRDF	Bidirectional Reflectance Distribution Functions
BSRN	Baseline Surface Radiation Network
CALIPSO	Cloud-Aerosol Lidar and Infrared Pathfinder Satellite Observation
CERES	Clouds and the Earth's Radiant Energy System
CloudSat	CLOUD SATellite
DISORT	Discrete Ordinate Model
ECMWF	the European Center for Medium Range Weather Forecasts
ERBE	Earth Radiation Budget Experiment
EUMESAT	European Organisation for the Exploitation of Meteorological Satellites
FOV	Field of Views
GCM	General Circulation Models
GOES	Geostationary Operational Environmental Satellite
GEWEX	Global Energy and Water Cycle Experiment
GISS	Goddard Institute for Space Studies
GOCART	Global Ozone Chemistry Aerosol Radiation Transport
IPCC	Intergovernmental Panel on Climate Change
ISCCP	International Satellite Cloud Climatology Project

METEOSAT	Meteorological Satellite
MISR	Multi-angle Imaging Spectro-Radiometer
MODIS	Moderate Resolution Imaging Spectroradiometer
NASA	National Aeronautics and Space Administration
NCAR	National Center for Atmospheric Research
NCEP	the National Centers for Environmental Prediction
NESDIS	National Environmental Satellite Data and Information Service
NIR	Near-Infrared
NOAA	National Oceanic and Atmospheric Administration
NSIDC	National Snow and Ice Data Center
PAR	Photosynthetically Active Radiation
PSU	Penn State University
RMSE	Root Mean Spare Error
SBDART	Santa Barbara Discrete ordinate Atmospheric Radiative Transfer Model
SD	Standard Deviation
SEVIRI	Spinning Enhanced Visible Infrared Imager
SRB	Shortwave Radiation Budget
SSM/I	Special Sensor Microwave/Imager
SURFRAD	Surface Radiation Network
SWR	Shortwave Irradiance
SZA	Solar Zenith Angle
TOA	Top of the Atmosphere

TRMM	Tropical Rainfall Measuring Mission
UMD	University of Maryland
UTC	Coordinated Universal Time
VZA	Viewing Zenith Angle

List of Tables

List of Figures

Chapter 1: Introduction

1.1 Background

Surface warming in the Arctic has been almost twice as large as the global average over recent decades, known as the 'Arctic amplification' phenomenon. Associated with the warming in the Arctic, the Arctic sea ice cover has decreased dramatically. Acceleration in Arctic sea ice loss (both seasonal and perennial ice) has shifted from about -3.0% per decade in 1979-1996 to about -10.7% per decade in 1996-2007 (*Comiso et al., 2008*). Ice loss in 2007 was documented to exceed that in any previous year since the availability of sea ice observations. Faster loss of sea ice was experienced than the expected values predicted by the Intergovernmental Panel on Climate Change (IPCC) models *(Parry et al., 2007).* Increased precipitation, warming of soils and permafrost, and vegetation cover changes from tundra to shrubs has also been observed over the Polar Regions. It has been suggested that these changes are a consequence of long-term anthropogenic forcing and associated feedbacks (e.g., *Arctic Climate Impact Assessment, 2004*).

Understanding the feedbacks that alter greenhouse-gas forcing, such as ice-albedo feedback due to the reduction in snow/ice coverage, aerosol-cloud-radiation feedback, water vapor feedback, UV-ozone feedback, is also a major challenge in predicting the Polar Regions future climate state. Thin sheets of sea ice are very sensitive to the variations of solar inputs to the ice-ocean system. Reduced ice in spring and summer is important to the climate system because the timing coincides with strongest shortwave (solar) irradiance (SWR), of which ice is an excellent reflector. The ice melting is triggered by the formation of melt pools which will further decrease the ice albedo and consequently increases the absorption of SWR. The melt pool growth with SWR during the summer months will accelerate the ice melting. Ocean-atmosphere coupled models have simulated the effects of the ice-albedo feedback at high latitudes due to CO_2 doubling and the reduction in reflected SWR over north polar caps showing it to be more pronounced during spring and summer than in fall and winter *(Hall, 2004)*. Therefore, accurate estimates of SWR are needed for investigating causes of ice loss, especially during the extreme ice loss year of 2007.

Satellite estimates and model simulations of SWR at high latitudes agree less with ground observations than at other locations. Ground observations at these latitudes are scarce and observations taken during the International Polar Year (IPY) 2007-2008 were aimed to address this void. In this study, newly developed and updated methodologies will be applied to improve SWR estimates from satellite based observations at high latitudes. The ice-albedo feedback will be investigated by utilizing these new satellite-based products.

1.2 Climatic changes over Polar Regions

Records and model simulations show that climate change in the Arctic is more pronounced than in the mid-latitudes or tropical regions *(Houghton et al., 2001; Arctic Climate Impact Assessment, 2004)*. The greatest warming in Polar Regions has been documented both by current climate observations *(Serreze et al., 2000)* and paleoclimate reconstructions *(Overpeck et al., 1997)*. The Arctic region is expected to experience an enhanced and accelerated greenhouse-induced warming in comparison to other regions of the globe, largely, because of polar amplification due to feedback and interactions involving primarily the high albedo of snow and ice *(Manabe et al., 1992)*. Long-term surface station data indicate that upward trends of the annual average temperatures are exceeding 1-2° C/decade in northern Eurasia and northwestern North America during 1996-2003 *(Arctic Climate Impact Assessment, 2004)*. Satellite records covering the period of 1981-2001 exhibit statistically significant warming trends of 0.5° C/decade in Eurasia, and 1.06° C/decade in North America *(Comiso, 2003)*. Recent studies from the time series of anomalies relative to the 20th century average for annually averaged surface temperature (60° N-90° N) over land (*Figure 1.1*) show an apparent warming after 1990s, which most likely has an anthropogenic component *(Overland et al., 2007; Wang et al., 2007)*.

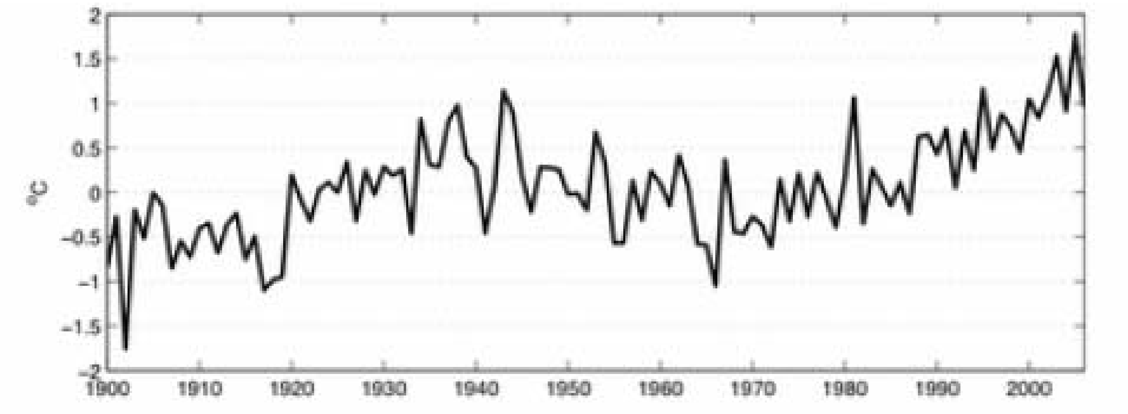

Figure 1.1 Arctic-wide annual average surface air temperature anomalies (60° N - 90° N) over land for 1990-2006 based on the CRU TEM2V monthly data set. Anomalies are relative to the 20th century average *(Overland et al., 2007)*.

Surface and satellite data of surface temperature of the Arctic peripheral seas during summer show that many areas cooled up to ~0.5° C per decade during 1930-

1965 and warmed during 1965-1995. Warming has been particularly pronounced since 2000, with an anomaly reaching 5° C in the summer of 2007 (*Steele et al., 2008*). The mean satellite-derived summer sea surface temperature for the period of 1982-2007 and the anomalies from this mean over 2005 and 2007 associated with the September-mean ice edge for 2005 and 2007 are shown in *Figure 1.2*. The warming anomalies in sea surface temperature correspond to the sea ice loss region.

The Arctic warming has been strongest in late fall and early winter (October-January) for the period of 1989-2009 *(Screen and Simmonds, 2010)* (*Figure 1.3*) while sea ice reduction and the direct ice-albedo feedback have been greatest in summer and early fall. The studies of *Screen and Simmonds (2010)* point out that the increase in the heat transfer from the Arctic Ocean to the atmosphere is the possible cause of the warming in the late fall and winter. The increase in such heat transfer is likely a combination of the direct response to fall/winter sea ice loss (the 'insulation' effect) and the indirect response to summer sea ice loss and increased summer ocean heating (the 'delayed warming').

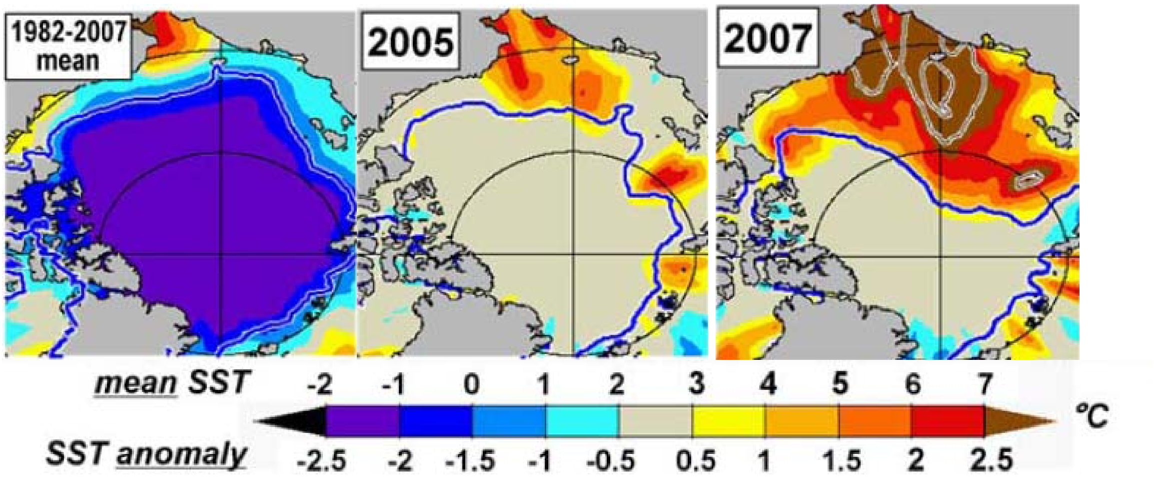

Figure 1.2 Mean satellite-derived summer sea surface temperature *(Reynolds et al., 2002)* and the anomalies from this mean over 2005 and 2007 (extra contours for 3° C and 4° C are provided). Also shown is the September-mean ice edge (blue contour) from the Hadley Center (1982-2006: http://badc.nerc.ac.uk/data/hadisst/) and from the National Centers for Environmental Prediction (2007: ftp://polar.ncep.noaa.gov/pub/cdas/) *(Steel et al., 2008)*.

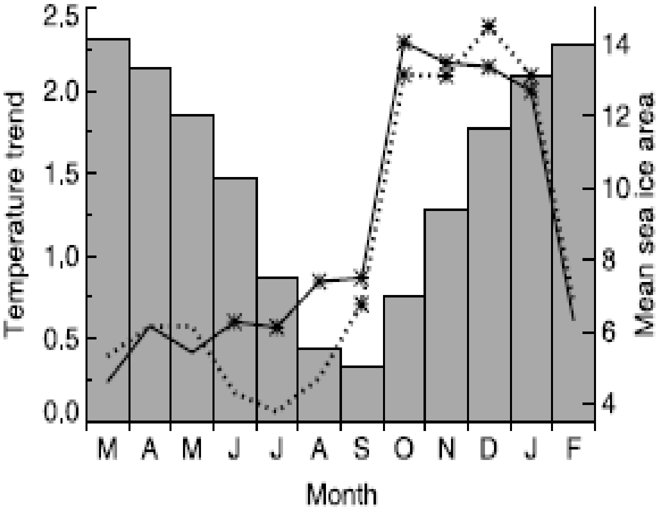

Figure 1.3 Annual cycle of surface temperature trends (° C per decade) for 1989-2009 averaged from meteorological stations north of 70° N (solid line) and ERA-Interim (dotted line). Gray bars are the annual mean sea ice areas (10^6 km^2) *(Screen and Simmonds, 2010)*.

With this large warming, the climate and ecosystems over the Polar Regions have been undergoing the most rapid and severe change on Earth. The areal extent of Arctic sea ice has decreased dramatically in recent decades. The annual mean sea ice extent derived from satellite observations has declined by about 3% per decade since 1979 *(Serreze and Francis, 2006)*. The time series of the anomalies for ice extent in March and September from Year 1979 to 2007 is exhibited in *Figure 1.4*. The negative trend is 2.8% per decade for March and 11.3% per decade for September (the month of the seasonal minimum) *(Menge et al., 2007)*. Acceleration in trends of the entire sea ice cover (seasonal and perennial ice) loss have shifted from about -3.0% per decade in 1979-1996 to about -10.7% per decades in the last 10 years (1996-2007). The latter trends are comparable to the high negative trends of -11.4% per decade for the perennial ice area for the period of 1979-2007 *(Comiso et al., 2008)* (*Figure 1.5*). The Arctic sea ice thickness and volume are also showing a declining trend *(Lindsay and Zhang, 2005)*, and the snow cover at high latitudes has exhibited some negative anomalies since the late 1980s *(Armstrong and Brodzick, 2001; Brown et al., 2010)*. Greenland has one-twentieth of the global ice and the ice on top of it is undergoing dramatic melting as documented by in-situ and space observations. However, the lack of long term, systematic, and broadly observed datasets limits our understanding and prediction to what extent the Greenland ice sheets have melted and if the “tripping point” has been reached so that the melted ice could not rebuild in future *(Witze, 2008)*.

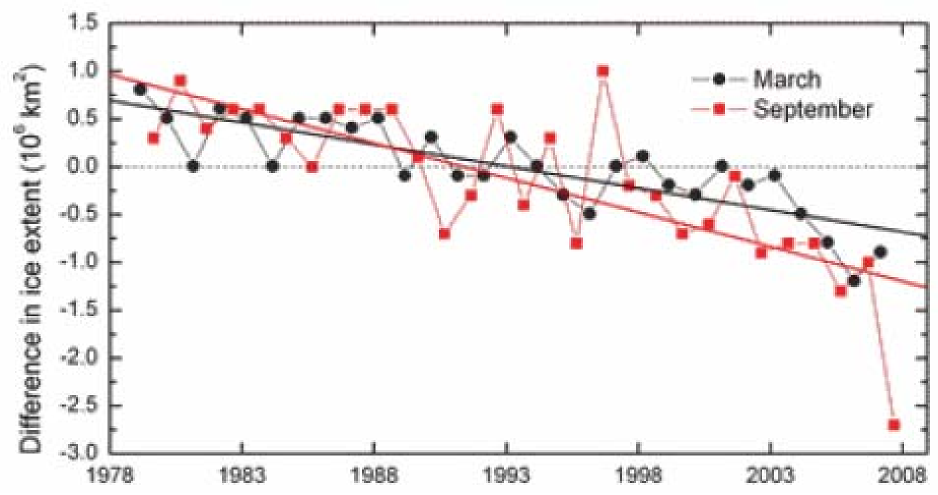

Figure 1.4 Time series of the difference in ice extent in March and September from the mean values for the time period 1979-2007 *(Menge et al., 2007)*.

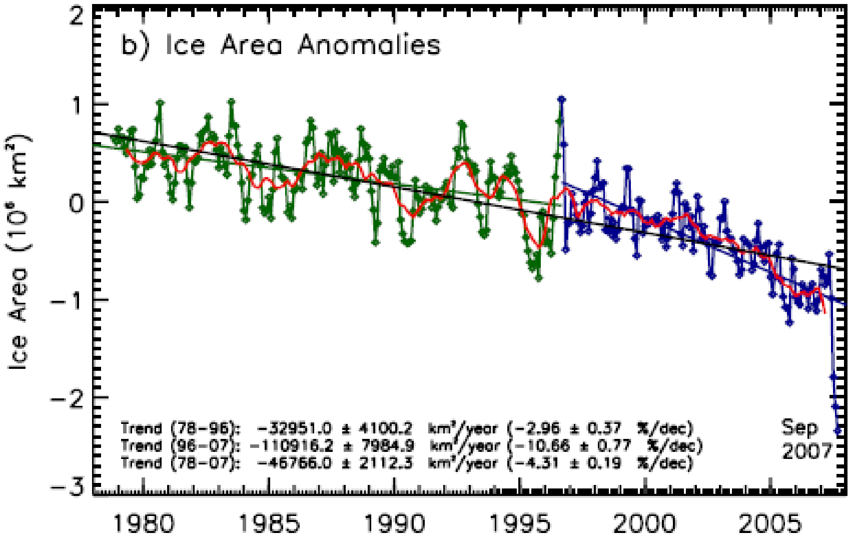

Figure 1.5 Arctic monthly ice area anomalies from November 1978 to September 2007 (green and blue), with the 12-month running average (red) and linear trend lines for the full record (black) and for 1978-1996 (green) and 1996-2007 (blue) *(Comiso et al., 2008)*.

The 2007 minimum sea ice extent over the Arctic represents a dramatic departure from the historical trend, 4.13 million km^2 on September 16, 2007, decreasing 43% from 1979 and 22% from the previous record in 2005. During 2007, large negative anomalies in ice extent persisted from July through September, mostly in the Pacific sector of the Arctic *(Stroeve et al., 2008)*. The 2008 September minimum was the second smallest extent on record (*Figure 1.6*). Including 2008, the linear trend in September ice extent over the satellite record is -11.7% per decade *(Serreze et al., 2009)*. The ice extent in 2009 and 2010 is between the lower record years of 2005 and 2007. The Arctic perennial sea ice extent (in March each year) has declined since the 1950s and became more rapid in the 2000s and significantly reduced between March 2005 and 2007 (a 23% loss) as observed from satellite and buoy-based model *(Nghiem et al., 2007)* (*Figure 1.7*). Such shift from perennial to thinner seasonal sea ice during winter contributes to a decrease in surface albedo allowing more solar heating input into the Arctic ice-ocean system during summer melt *(Nghiem et al., 2007; Perovich et al., 2002 and 2007)*. The seasonal cycle of Arctic ice cover variations shows that the 2007 Arctic ice cover was comparable to 2005 and 2006 through mid-June but then began a pronounced decline during the summer and early fall *(Comiso et al., 2008)* (*Figure 1.8*). The extreme low record of ice cover in September 2007 is illustrated in *Figure 1.9*; as seen, much of the reduction occurred in the extended region of the Beaufort Sea, Chukchi Sea, East Siberian Sea, Laptev Sea and Kara Sea *(Comiso et al., 2008)*. These regions are generally located in the Arctic marginal area. The study of *Linkin (2008)* also indicated that the main area of sea ice variation is in the Arctic marginal seas (70° N and 80° N) in the summer.

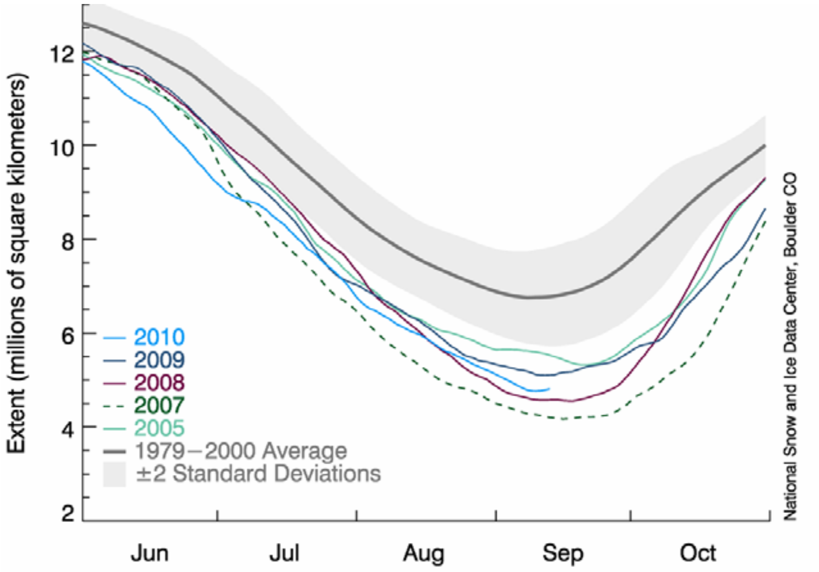

Figure 1.6 Arctic sea ice extent (area of ocean with at least 15% sea ice) (http://nsidc.org/arcticseaicenews/2010/091510.html from NSIDC).

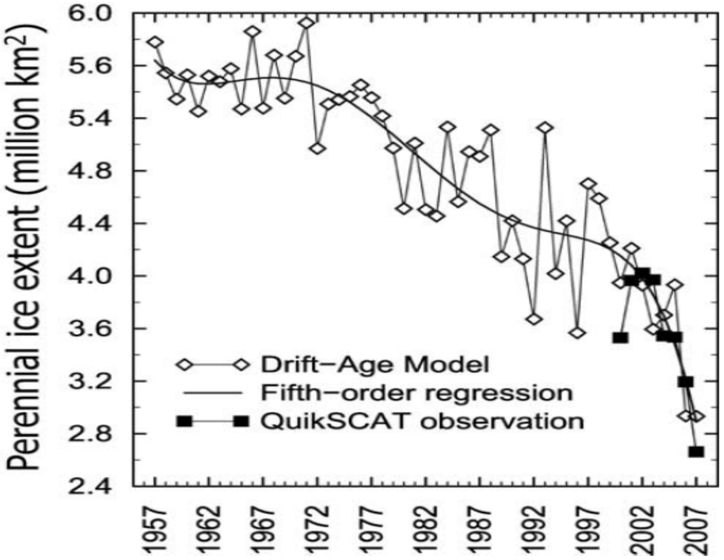

Figure 1.7 Time-series of Arctic perennial sea ice extent in March of each year estimated from the buoy-based Drift-Age Model and observed by QuikSCAT satellite scatterometer *(Nghiem et al., 2007)*.

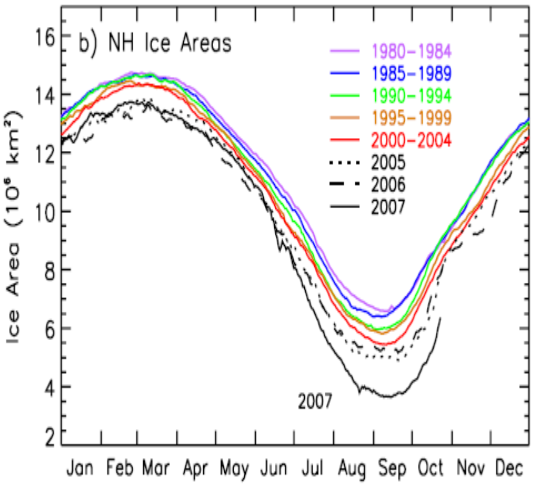

Figure 1.8 Daily ice areas for 2005, 2006, 2007, and averaged over 1980-84 and 2000-04 based on NASA's Scanning Multi-channel Microwave Radiometer (SMMR) and the Department of Defense Special Sensor Microwave Imager (SSM/I) *(Comiso et al., 2008)*.

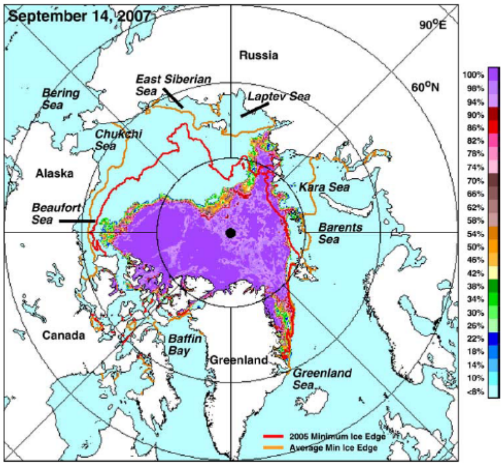

Figure 1.9 Daily Arctic ice concentrations from AMSR-E for 14 September 2007 (minimum extent). *Gold contour:* averaged ice edge over the period 1979-2006; *red contour:* ice edge in 2005, the previous record low *(Comiso et al., 2008)*.

1.3 Large-scale circulation contributing to climate change in the Arctic region

Due to these rapid and large climate changes over the Polar Regions, it is important to know their causes. For instance, there are strong correlations between surface temperature anomalies and climate indices such as the Arctic Oscillation (AO) index suggesting linkage between global climate change and Arctic climate change *(Wang et al., 2003)*. The positive phases of AO and El Niño Southern Oscillation (ENSO) produce similar ice changes in the western Arctic, but opposite ice changes in the eastern Arctic *(Liu and Curry, 2004)*. The AO has become more neutral in recent years, but the Arctic sea ice continues to decline rapidly. This discrepancy between the AO index and the loss of ice can be explained by other factors, such as ea level pressure patterns *(Maslanik et al., 2007)*, summer atmospheric circulations *(Ogi and Wallace, 2007)*, and anomalies of clouds and SWR *(Kay et al., 2008)*. In addition to the large scale circulations, the capability to capture the Arctic stable boundary layer is also important for models to realistically simulate present day Arctic climate. The Arctic winter inversion and vertical turbulent-exchange processes in the boundary layer will be better represented by fine vertical mesh *(Byrkjedal et al., 2008)*. Both the winter and summer circulation was favorable for a drastic sea ice loss in summer of 2007. Cyclonic anomalies during the winter of 2006-2007 and a strong anticyclone in the late spring and summer of 2007 led to Ekman drift in the marginal seas *(Ogi et al., 2007)* and thin ice growth and Ekman convergence to greatly reduce summer sea ice *extent (Linkin, 2008).*

1.4 Ice-albedo feedback

The initial theoretical proposal of ice-albedo feedback can be traced to *Croll (1875)*. The concept is that changes in surface albedo associated with changes in snow and ice cover as a result of temperature change may further change the temperature and give a positive feedback to climate change. For example, if enough ice is lost due to global warming, extra heat can be stored in these regions and remain through winter and reduce the ice thickness in the following spring. Based on a modeling study *(Jin et al., 1994)*, the sea ice has a significant impact on the absorption and partitioning of the SWR energy in the atmosphere, sea ice, and ocean system. Ice thickness becomes important to the energy distribution only when the ice is thin. The ice-albedo feedback results from the large contrast between the albedo of sea ice (>0.6) and open water (~0.07) which can accelerate the loss of ice. Model simulations suggest that in addition to ice extent, the duration of the snow cover, ice thickness, ice distribution, lead fraction, and melt pond characteristics could also significantly influence the strength of the ice-albedo feedback *(Curry et al, 1995)*.

The ice-albedo feedback may play a leading role for the recent continuing sea ice loss and warming in the Arctic. The trend of cloud and surface properties derived from satellites for the period of 1982 to 1999 shows that the Arctic has warmed and became cloudier in spring and summer but has cooled and became less cloudy in winter *(Wang et al., 2003)*. The increase in spring cloud amount radiatively balances changes in surface temperature and albedo, but during summer, fall, and winter, cloud forcing has tended toward increased cooling. Using the ERA-Interim reanalysis dataset, *Screen and Simmonds (2010)* have found that the changes in cloud cover have not contributed strongly to recent warming and that increase in atmospheric water vapor content may have enhanced warming in the lower part of the atmosphere during summer and early autumn. They also suggest that Arctic warming is strongest at the surface during most the year and consistent with reduction in sea ice cover, and that the reduction of sea ice has a leading role in recent Arctic temperature amplification because the retreating of snow and sea ice is expected to cause maximum warming at the surface as shown in *Screen and Simmonds (2010)* (*Figure 1.10*). Hypotheses, models and observations suggest that sea ice plays an important role in the state and variability of regional and global climate through the ice-albedo feedback, insulating effect, deep water formation and fresh water budget.

Investigations using field data from the Arctic Alaska *(Chapin et al., 2005)* indicate that a lengthening of the snow-free season associated with the vegetation and summer albedo changes has increased regional warming by about 3 W m^{-2} $decade^{-1}$. This is similar in magnitude to the effect of atmospheric CO_2 doubling over multiple decades. This heating more than offsets the cooling caused by increased cloudiness.

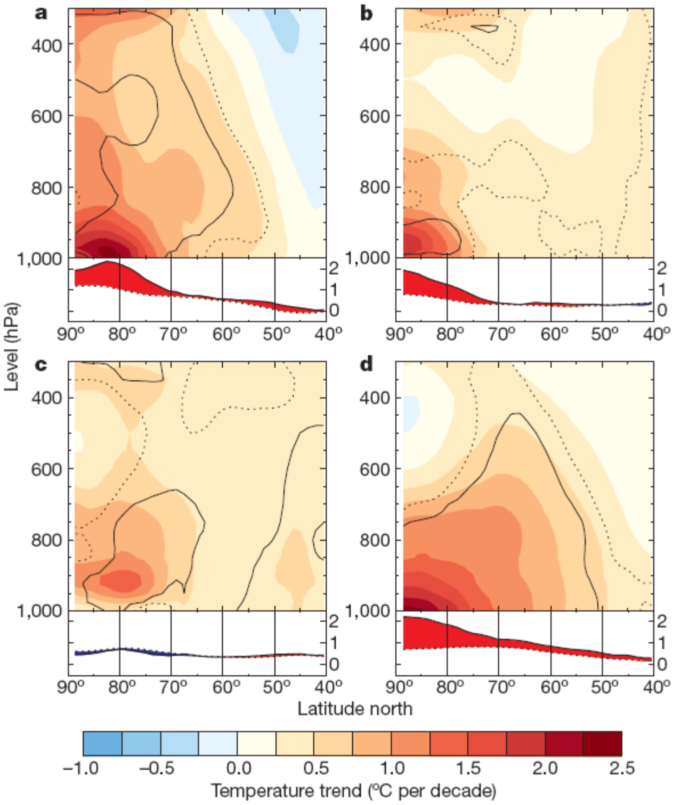

Figure 1.10 The vertical temperature averaged around circles of latitudes for (a) winter (Dec.-Feb.), (b) spring (Mar.-May), (c) summer (Jun.-Aug.), and (d) autumn (Sep.-Nov.) for 1989-2008 from ERA-Interim reanalysis data. The line graphs show temperature trends averaged over the lower part of the atmosphere (950-1000 hPa; solid lines) and over the entire atmospheric column (300-1000 hPa; dotted lines) *(Screen and Simmonds, 2010)*.

The ice-albedo feedback is viewed as a direct link between surface albedo and surface temperature; however, it is a much more complex process that varies at different temporal and spatial scales over land and ocean, and is still not well understood. *Francis and Hunter (2006)* gave the approximate locations and trends of mean perennial ice edges in six regions (*Figure 1.11*) and found that the location of the summer ice edge is strongly correlated to variability of downward long-wave flux. But in a warmer Arctic with thinner ice, clouds and shortwave radiation anomalies will play an increasingly important role in modulating summertime sea ice extent compared to longwave flux variation by examining years of 2006 and 2007 for the Western Arctic Ocean *(Kay et al., 2008)*. The looming question now is whether enough sea ice has melted to trigger the model-predicted ice-albedo feedback, as suggested by *Serreze and Francis (2006)* and *Lindsay and Zhang (2005)*.

The Arctic warming depends on how much energy gained during summer due to the sea ice albedo feedback and stored in the ocean may be carried through the winter months *(Serreze and Francis, 2006)*. The simulations from 14 coupled global climate models suggest that the changes in the net sea ice melt is significantly related to the changes in downward longwave and absorbed shortwave radiation *(Holland et al., 2008)*.

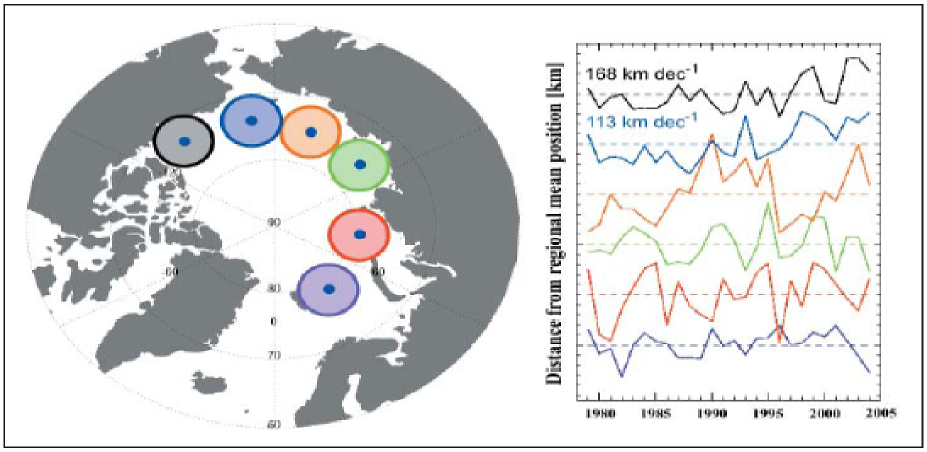

Figure 1.11 (Left) Approximate locations of mean perennial ice edge locations in six regions, and 400-kilometer-radius areas in which forcing anomalies are determined; (Right) Time series of anomalies in northernmost location of perennial ice edge. Dashed lines indicate zero anomalies relative to the 1979–2004 mean; ticks on the y-axis denote 100 kilometers *(Francis and Hunter, 2006)*.

1.5 Current estimates of radiative fluxes at high latitudes

Observations and model simulations of radiative flux estimates at high latitudes are not consistent. Field observations and buoy measurements provide only short data records for specific locations. An alternative source of information are data from reanalysis (e.g., the National Centers for Environmental Prediction (NCEP) or the European Center for Medium-Range Weather Forecasts (ECMWF)), or satellite observations of high spatial and temporal resolution. Recent studies *(Liu et al., 2005)* indicate that the surface downward SWR derived from satellites are more accurate than the two main reanalysis datasets (NCEP and ECMWF), due to better information on cloud properties. During the Surface Heat Budget and the Arctic Ocean (SHEBA) project *(Perovich et al., 1999)* it was shown that satellite-based analysis may provide downward SWR to within ~ 10-40 Wm^{-2} as compared to observations. The surface energy budget over the Arctic (70° N -90° N) from 20 coupled models in the IPCC fourth Assessment compared with 5 observationally based estimates and reanalysis results has shown large bias and the largest differences are located over the marginal ice zone *(Sorteberg et al., 2007)*.

Estimates of SWR from satellite observations disagree most at high latitudes. Present-day Arctic and Antarctic radiation budgets of the National Center for Atmospheric Research Community Climate Model version 3 (CCM3) *(Briegleb, 1998)* show that the summer Top-of-Atmosphere (TOA) absorbed shortwave radiation estimates in the Arctic and the Antarctic from 1985 to 1989 are 20 Wm^{-2} less than from ERBE (Earth Radiation Budget Experiment) data and the surface downward SWR estimates are smaller by 50-70 Wm^{-2} compared with one-dimensional model calculations based on *Curry and Ebert (1992)* and observational surface data. Comparison of surface SWR from different inference schemes based on satellite observations such as: the University of Maryland/Shortwave Radiation Budget (UMD/SRB) model driven with the International Satellite Cloud Climatology Project (ISSCP) DX data (UMD/DX) *(Ma and Pinker, 2011*), the NASA CERES model *(Wielicki et al., 1996)*, the NASA Langley model (GEWEX) *(Gupta et al., 2001; Stackhouse et al., 2004)*, and the NASA Goddard Institute for Space Studies (GISS) model (ISCCP-FD) *(Zhang et al., 1995; Zhang et al., 2004)*, show large differences in Polar Regions (*Figure 1.12*) with most notable differences found at the edges of coastlines (*Figure 1.13*). It is believed that the accuracy of SWR estimates in these regions can be improved by utilizing improved satellite observations (e.g. MODIS), updated inference schemes, and improved information on the atmosphere and the surface. In particular, data on surface condition have improved in recent years (such as ice extent), atmospheric information (such as aerosol and cloud properties) became available, inference schemes with realistic surface models and newly available bi-directional distribution functions (BRDF) (e. g., from CERES or MISR) have been developed.

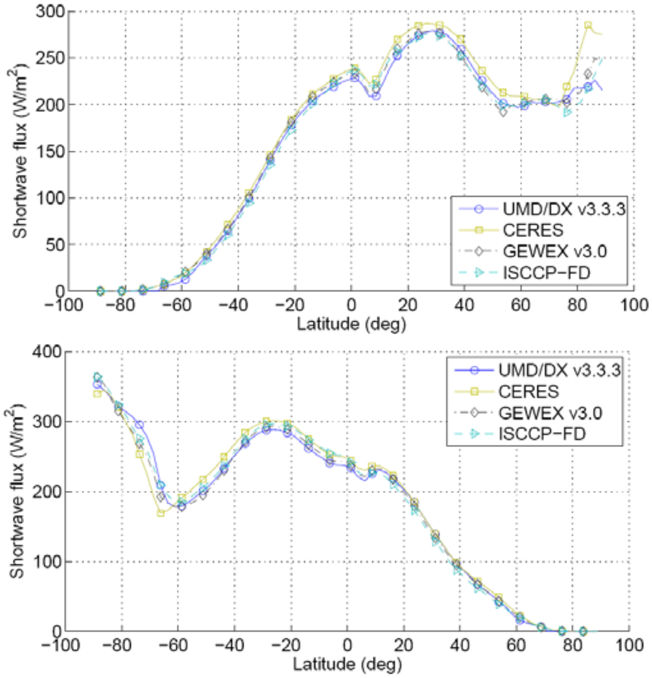

Figure 1.12 Zonally Mean all-sky surface downward SWR for Sep 2000-Aug 2005 as obtained from the UMD models with ISCCP DX inputs, CERES, GEWEX, and ISCCP-FD models: (top) for summer months (JJA); (bottom) for winter months (DJF) (courtesy of Y. Ma).

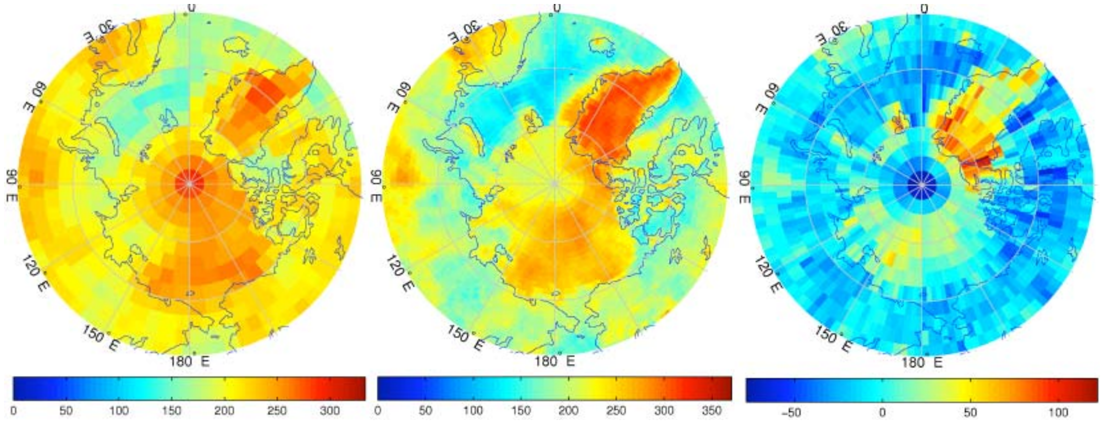

(a) (b) (c)

Figure 1.13 Monthly mean surface downward SWR from (a) ISCCP-FD and from (b) UMD_MODIS, and (c) the difference between the two products for North Polar Region for July 2005.

1.6 Research motivation and questions

The focus of this study is the development of improved satellite based information on shortwave radiative flux estimates at high latitudes so the ice-albedo feedback can be estimated over the entire polar region at improved accuracy. As yet, the issue which mechanism controlled the abrupt climate change in the Arctic regions during the past decades has not been resolved. Several studies based on model simulations suggest that the positive ice-albedo feedback may be the main contributor to the recent extreme sea ice retreat including 2007 (e.g., *Lindsay and Zhang, 2005; Perovich et al., 2007, 2008; Hwang et al., 2011; Stroeve et al., 2011*). The issue is challenging for model simulations because the individual mechanisms contributing to such changes are strongly coupled. Studies on the effect of solar heat input on sea ice extent using satellite estimates of radiative fluxes are limited. Addressing this issue is timely since new and/or improved information became available that provides an opportunity to revisit the inference schemes and the ice-albedo feedback at high latitudes. The following questions will be addressed:

- What is the accuracy of surface SWR estimates from satellites and models at high latitudes during recent years including the years of highest documented Arctic sea ice loss?
- What is the relationship between variation of surface SWR and sea ice at the Arctic Ocean?
- What are the trends of surface SWR absorbed by the open water at the Arctic Ocean and how do they relate to sea-ice loss?
- How do the higher temporal and spatial resolution satellite-based products (e. g., from MODIS) influence SWR estimates at high latitudes, especially at the Arctic marginal seas? To what level can it contribute to the melting of sea ice and warming the overlaying atmosphere?
- How much of the increase in heat input into the ocean is due to the reduction in sea ice observed in 2007 as compared to an average year?

1.7 Thesis organization

The thesis is divided into three main parts: development of improved inference schemes for SWR fluxes for high latitudes and implementation of the new inference schemes with relevant satellite observations; evaluations of the newly available information; and estimation of the ice-albedo feedback using the new information. *Chapter 2* focuses on the model improvements. *Chapter 3* presents an evaluation of the newly obtained satellite estimates against surface observations (land sites and buoys) at high latitudes. *Chapter 4* presents the calculations of the solar heat input into the Arctic Ocean or ice-ocean system using the new products and investigates the relationship between the solar heating of the Arctic Ocean and sea ice retreat in recent decades. Conclusions and future research plans are discussed in *Chapter 5*.

Chapter 2: Improved SWR estimates at High Latitudes

2.1 Research design

To address as yet, not fully understood issues related to high latitudes, there is a need for high quality, long term information on radiative fluxes at high spatial resolution. Available satellite estimates do not meet all the needs for high latitudes as described in *Chapter 1*. In this study we have developed tools that allow synthesizing information from numerous sources to better meet high latitude research needs.

The Moderate Resolution Imaging Spectroradiometer (MODIS) instrument onboard the Terra and Aqua satellites observes the earth at higher spatial and spectral resolution than earlier satellites, thus improving capabilities to detect atmospheric and surface properties with high accuracy. The MODIS observations have been extensively utilized to derive various parameters such as cloud, aerosol, and surface properties *(King et al., 2003; Moody et al., 2005, 2007)*. However, only limited attempts have been made to derive radiative fluxes from MODIS. *Wang and Pinker (2009)* developed a globally applicable methodology to derive shortwave radiative fluxes from MODIS observations at 1° and 5-km spatial resolution; it has been evaluated against numerous ground and oceanic observations *(Pinker et al., 2009; Niu et al., 2010; Niu and Pinker, 2011).* The methodology has not been optimized for high latitudes as will be discussed in detail in *Section 2.2*. The most suitable product from MODIS to address ice loss impacts is the 5-km one. However, implementation at such resolution is formidable in scope. Therefore, the 1° products from MODIS is used to derive the SWR for the longest available record (about 10 years) while the high resolution MODIS data at 5-km is applied for the summer months of 2007 with the extreme ice loss on record. This allows estimation of an error bar on the magnitude of the ice-albedo feedback due to spatial resolution of observations. Even the ten-year MODIS record is not sufficient to study the inter-decadal variations of ice-albedo feedback. Long term information over Polar Regions can be derived from the Advanced Very High Resolution Radiometer (AVHRR) sensors which is available from 1981 to present. AVHRR observations have been successfully utilized before, e.g. *Key (2002),* who produced a record of SWR at 25-km resolution for the period of 1982-2004. It is hypothesized that new information on atmospheric and surface conditions that became available since the *Key (2002)* publication as well as more recent updates in inference schemes, can improve radiative flux estimates at high latitudes.

Optimally, there should be an information overlap between all the MODIS and AVHRR products providing an opportunity for cross evaluation/calibration. To meet such an objective, the two years 2003-2004 were selected. There are unique advantages to each product, in particular, for establishing limits on the accuracy of satellite estimates over the Polar Regions. The MODIS and AVHRR inputs and outputs are listed in *Table 2.1* and further described in what follows.

Table 2.1 Input and output to MODIS and AVHRR inference schemes (based on *Wang and Pinker (2009) and Ma and Pinker (2011)*).

	Satellite sensor	Input data	Spatial resolution	Temporal resolution	Time period
UMD_MODIS	MODIS	MODIS Level-3 daily aerosol, water, cloud, surface parameters and Microwave sea ice	1°	Daily	2002-2010
	MODIS	MODIS Level-2 aerosol, cloud, water, surface parameters	5 km	about 7 per day	summer months of 2007
UMD_AVHRR	AVHRR	Spectral radiances from visible channel (0.58-0.68μm)	30 km	Twice daily over Arctic	1983-2006
Output Products	Hourly, daily, and monthly averaged SWR (0.2-4μm) upward/downward total and diffuse fluxes at TOA/surface and information on cloud and aerosol optical depth.				

2.2 *Inference scheme for MODIS (UMD_MODIS)*

2.2.1 Background

The UMD_MODIS inference scheme utilizes independently derived optical parameters from the MODIS multi-spectral satellite observations, (e. g., aerosol and cloud optical depths; precipitable water; ozone; cloud types and location *(King et al., 1992, 2003; Platnick et al., 2003).* Such information is needed to derive spectral SWR at both 1° (MODIS Level-3 Atmosphere Daily Global Product) and at 5-km scales (MODIS Level-2 Swath Product) (*Su et al., 2008; Wang, 2007; Wang and Pinker, 2009*).

The MODIS instrument has 36 spectral bands in a wide spectral range (0.41-14.24 µm), frequent global coverage (up to 7 observations per day at high latitudes), and high spatial resolution (250 m for two bands, 500 m for five bands and 1000 m for 29 bands) (*Table 2.2*). This permits global monitoring of atmospheric properties and surface conditions at higher accuracy and consistency than previous Earth Observation Imagers (*King et al., 1992*). Two versions of MODIS products have been used: (1) MODIS Level-3 global daytime data from both Terra (~10:30 local time overpass) and Aqua (~13:30 overpass) to produce SWR at 1° longitude/latitude resolution globally; (2) MODIS Level-2 swath products at 5-km resolution to produce SWR at 5-km resolution over Arctic regions (60° N-90° N). The MODIS Level-3 Atmosphere Daily Global Products (MOD08_D3 from Terra, MYD08_D3 from Aqua) provide global daily information on the atmosphere which are derived from MODIS Level-2 atmospheric products: aerosol (MOD04, MYD04), precipitable water (MOD05, MYD05), cloud (MOD06, MYD06), and atmospheric profiles (MOD07, MYD07), where MOD denotes data collected from Terra platform and MYD indicates data collected from Aqua platform (*King et al., 2003).*

MODIS (5-km) provides a unique opportunity to derive almost hourly SWR at high latitudes due to the multiple overpasses (up to 7 per day) form Terra and Aqua *(Figure 2.1 from Key et al., 2003)*. Cloud detection is challenging at high latitudes because of the low contrast between clouds and snow/ice both in solar wavelengths (similar spectral albedos) and in terrestrial wavelengths (small temperature difference between the clouds and the surface; also, clouds are often warmer than the surface at high latitudes). The MODIS cloud detection algorithm uses multiple spectral threshold tests (up to six) over snow and ice during daytime, which has improved the accuracy of distinguishing clouds from snow *(Wang, 2007)*.

Table 2.2 Spectral channel characteristics of MODIS (based on *Xiong and Barnes, 2006)*

Primary Use	Channel number	Central wavelength (nm)	Bandwidth (nm)	Spatial resolution (m)
Land / cloud / aerosols boundaries	1	645	620 - 670	250
	2	858.5	841 - 876	
Land / cloud / aerosols properties	3	469	459 - 479	500
	4	555	545 - 565	
	5	1240	1230 - 1250	
	6	1640	1628 - 1652	
	7	2130	2105 - 2155	
Ocean color / phytoplankton / biogeochemistry	8	421.5	405 - 420	1000
	9	443	438 - 448	
	10	488	483 - 493	
	11	531	526 - 536	
	12	551	546 - 556	
	13	667	662 - 672	
	14	678	673 - 683	
	15	748	743 - 753	
	16	869.5	862 - 877	
Atmospheric water vapor	17	905	890 - 920	
	18	936	931 - 941	
	19	940	915 - 965	
Surface / cloud temperature	20	3750	3660 - 3840	
	21	3959	3929 - 3989	
	22	3959	3929 - 3989	
	23	4050	4020 - 4080	
Atmospheric temperature	24	4465.5	4433 - 4498	
	25	4515.5	4482 - 4549	
Cirrus clouds / water vapor	26	1375	1360 - 1390	
	27	6715	6535 - 6895	
	28	7325	7175 - 7475	
Cloud properties	29	8550	8400 - 8700	
Ozone	30	9730	9580 - 9880	
Surface / cloud temperature	31	11030	10780 - 11280	
	32	12020	11770 - 12270	
Cloud top altitude	33	13335	13185 - 13485	
	34	13635	13485 - 13785	
	35	13935	13785 - 14085	
	36	14235	14085 - 14385	

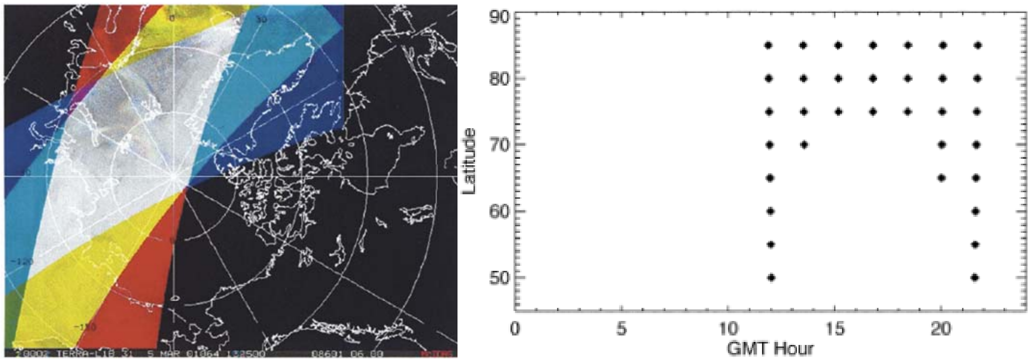

Figure 2.1 Left: Three successive MODIS orbits over the Arctic (red, green, blue) and the overlap of the orbits (whitish-gray shade); Right: MODIS (Terra) successive overpasses by latitude on September 1, 2000. Only overpasses with sensor view angles less than 50 are considered (*Key et al., 2003*).

The UMD_MODIS inference scheme is based on the delta-Eddington approximation to solve radiative transfer equations *(Wiscombe, 1977)*, which includes two main parts: Optical Properties Solver and Radiative Transfer Solver. The SWR is calculated in seven spectral intervals (0.2-0.4, 0.4-0.5, 0.5-0.6, 0.6-0.7, 0.7-1.19, 1.19-2.38, 2.38-4.0 μm) at specified pressure levels. The scheme takes into account all atmospheric constituents, both water and ice cloud properties (cloud particle effective radius and optical properties), and surface albedo. The spectral SWR is retrieved assuming a multi-layered structure which accounts for surface elevation effects and for the representation of the vertical distribution of atmospheric variables. In the scheme, the atmosphere is divided into more than 30 layers, depending on the aerosol profiles and on the presence of clouds and cloud layers *(Wang, 2007).* Details about the inference scheme are described in *Wang and Pinker (2009).* A flowchart of the scheme is shown in *Figure 2.2*. The 3-year monthly mean surface downward SWR for the North Polar Region and South Polar Region is shown in *Figure 2.3*.

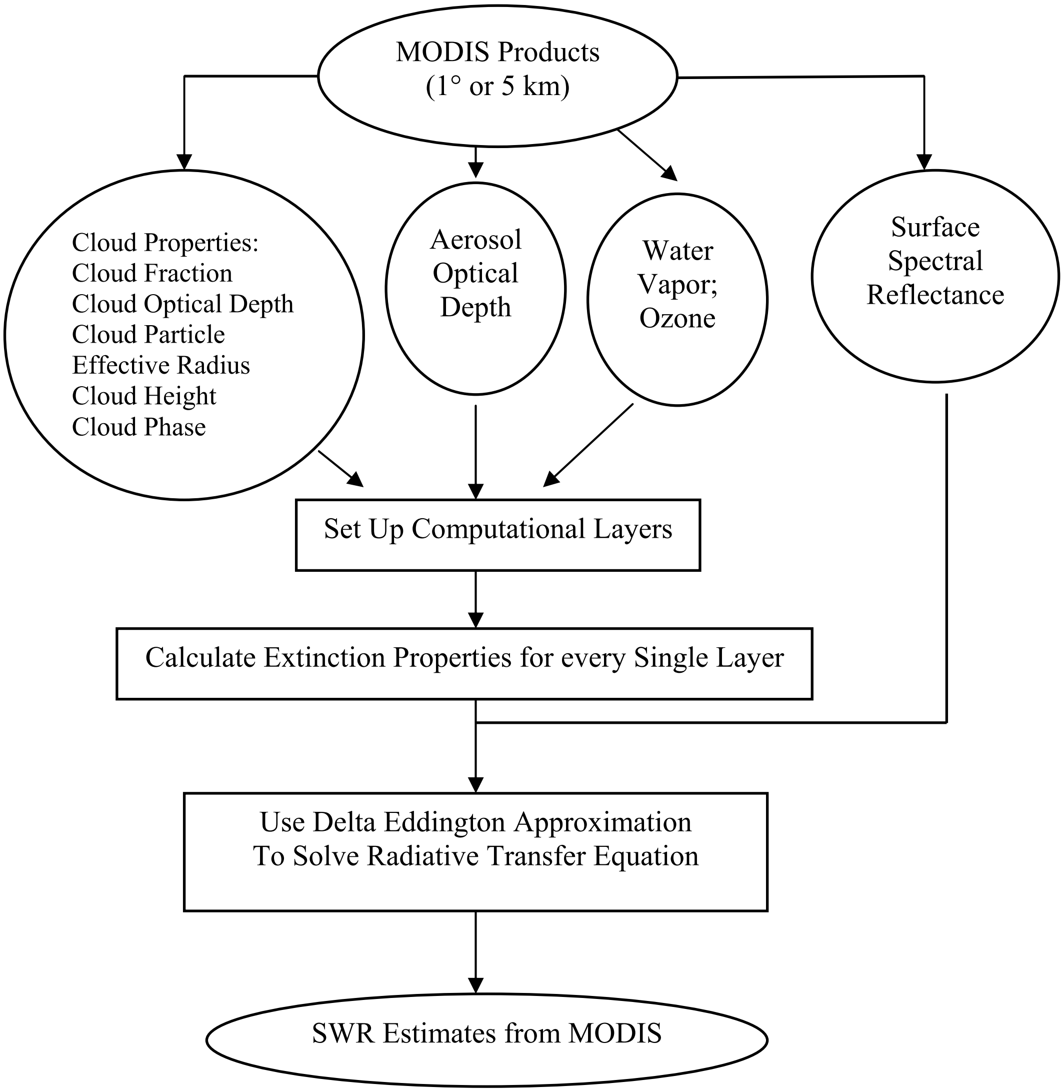

Figure 2.2 Flowchart of the framework to derive SWR estimates from MODIS (UMD_MODIS).

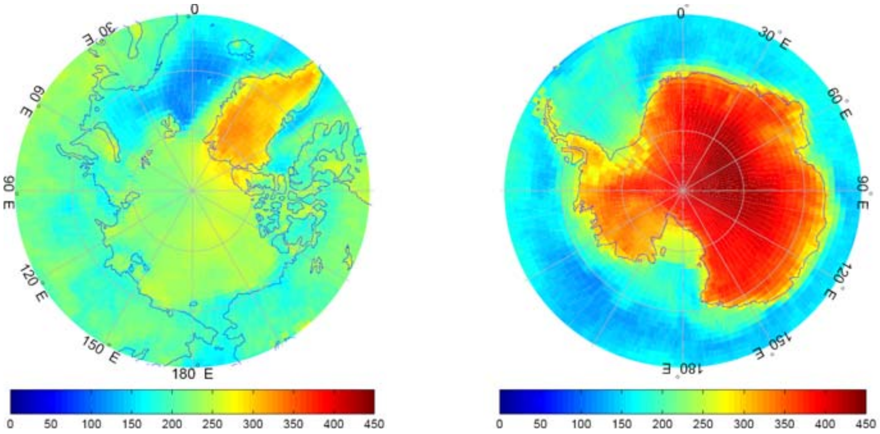

Figure 2.3 Monthly mean surface downward SW radiation estimated from UMD_MODIS (1°) for North Pole (left) for July and for South Pole (right) for January, both during (2003-2005) *(Niu and Pinker, 2010).*

2.2.2 Need for update to the MODIS inference scheme

The evaluations of the 1° UMD_MODIS products *(Wang and Pinker, 2009)* against ground observations have shown good agreement with ground observations over land and oceans at lower latitudes but surface SWR estimates were underestimated along the coastlines of high latitudes (e.g., at Barrow) *(Figure 2.4)*, possibly, due to the variable sea ice conditions that are difficult to account for. In this study updated information on surface properties for high latitudes was introduced to test possible improvements in the performance of the existing MODIS 1° framework. The methodology for using MODIS 5-km products to estimate SWR at high latitudes was also modified to allow the incorporation of high resolution information unique to polar environments as described in *Section 2.3*.

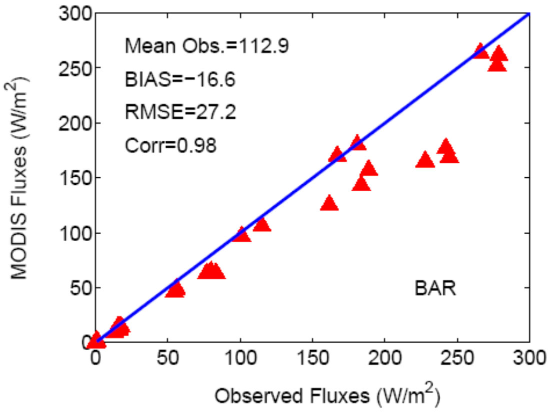

Figure 2.4 Evaluations of monthly mean surface downward SWR estimates from the previous version of UMD_MODIS (1°) against surface observations at Barrow, AK (72.32° N, 156.61° W) for 2003-05.

2.3 Improvements of UMD_MODIS model at high latitudes

2.3.1 High resolution snow cover and sea ice extent

In the original version of the UMD_MODIS *(Wang, 2007; Wang and Pinker, 2009)*, the MODIS daily global snow cover data at 0.25° were utilized (http://modis-snow-ice.gsfc.nasa.gov/). In the updated version, we use snow cover at 0.05° resolution at a daily time scale (MOD10C1 from Terra, MYD10C1 from Aqua), and utilize the monthly mean values from MOD10CM (Terra) and MYD10CM (Aqua) for gap filling in the daily product. The large number of missing values in the daily snow/ice cover dataset can result in the wrong identification of surface properties. Therefore, a temporal interpolation technique to fill missing values was introduced in this study. The daily mean snow/ice coverage at Barrow for year 2003 is illustrated in *Figure 2.5* for the original and the updated version.

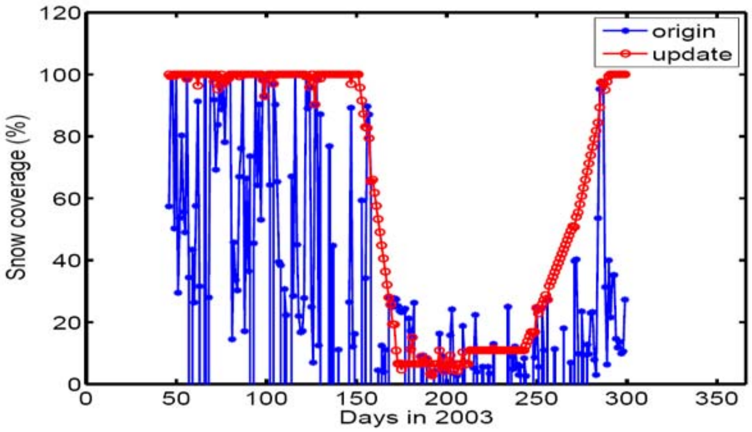

Figure 2.5 Daily snow coverage at Barrow, AK for year 2003 using the original data and the updated data by filling the missing values with monthly mean snow cover information.

The MODIS snow cover information is based on a snow mapping algorithm that employs several criteria such as the Normalized Difference Snow Index *(Hall et al., 2006)*. The information is available from the National Snow and Ice Data Center (NSIDC) (http://nsidc.org/data/modis/data_summaries/index.html). The monthly mean snow cover for June 2003 from the updated version and the difference in snow cover between the updated and the original versions are illustrated in *Figure 2.6*. There are large differences along the coastlines, which will translate to differences in the computation of the SWR from satellites.

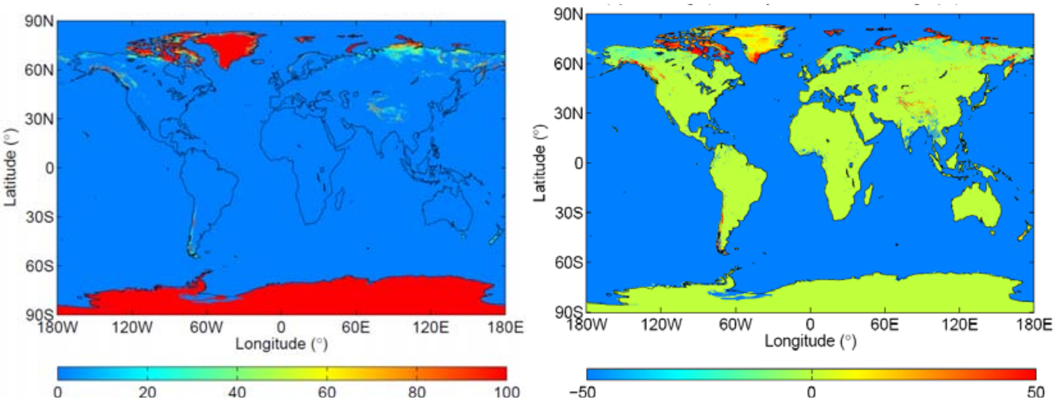

Figure 2.6 Monthly mean snow coverage (%) from the updated version (0.05°) (left), and the difference (updated version – original version) (right) for June 2003.

In the original SWR inference scheme *(Wang and Pinker, 2009),* the monthly mean sea ice extent at 1° grid cells based on the Special Sensor Microwave/Imager (NOAA/NESDIS National Climate Data Center (NCDC)) was used. The updated version uses the 25-km sea ice concentrations at both monthly and daily time scales as based on a NASA algorithm applied to the Nimbus-7 Scanning Multichannel Microwave Radiometer (SMMR) and the Defense Meteorological Satellite Program (DMSP) Special Sensor Microwave/Imager (SSM/I) radiances *(Cavalieri et al. 1996; updated in 2008)* (http://nsidc.org/data/nsidc-0051.html). The monthly mean sea ice extent from the original and updated versions for June 2003 is illustrated in *Figure 2.7.*

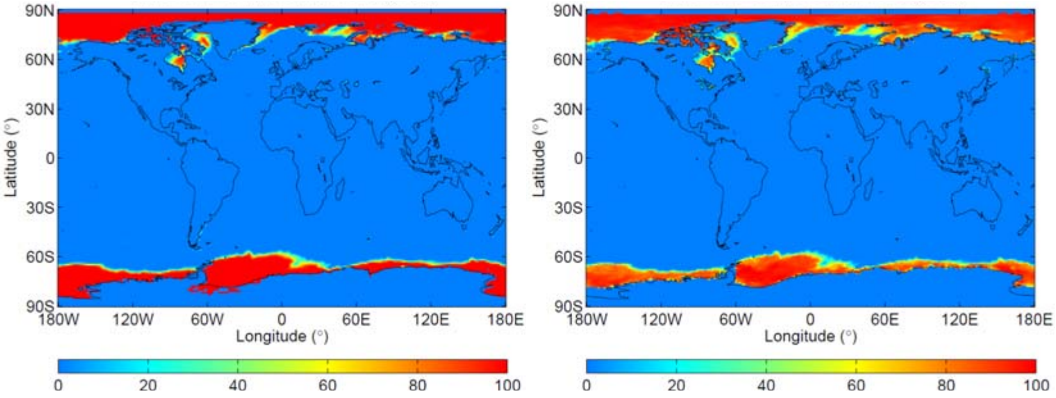

Figure 2.7 June 2003 monthly mean sea ice coverage (%) from the original version (1°) (left) and from the updated version (25-km) (right).

2.3.2 Surface spectral reflectance in presence of snow/ice

In the original scheme the spectral reflectance for a snow-covered surface was assumed to be constant at 0.9 for visible (VIS) and 0.6 for the near-infrared (NIR) part of the spectrum; for sea ice it was assumed to be 0.73 for the VIS and 0.33 for the NIR part of the spectrum. In the updated version, the surface spectral reflectance in presence of snow is derived from a combination of snow cover percentage and the MODIS surface reflectance products which provide a five-year (2000-04) statistics of spectral reflectance when the surface is covered by snow (the underlying surface types are aggregated according to the International Geosphere-Biosphere Program (IGBP) classification) *(Moody et al., 2007)*. For instance, in this dataset the white-sky reflectance (defined as reflectance in the absence of a direct component when the diffuse component is isotropic) at wavelength of 0.55 μm for snow-covered grassland, desert and permanent snow are 0.72, 0.87 and 0.94 *(Table 2.3)* (*Moody et al., 2007)*.

Table 2.3 Five-year (2000-04) averaged spectral white-sky surface albedo in the presence of snow aggregated by IGBP surface classifications for wavelengths of 0.55 μm, 1.24 μm, 0.3-0.7 μm, and 0.7-5.0 μm *(Moody et al., 2007).*

IGBP surface scene	White-sky snow albedo by wavelength (μm)			
	0.55	1.24	0.3-0.7	0.7-5.0
Evergreen needle forest	0.36	0.24	0.31	0.27
Evergreen broad forest	0.49	0.31	0.44	0.38
Deciduous needle forest	0.42	0.26	0.39	0.33
Deciduous broad forest	0.43	0.26	0.35	0.31
Mixed forest	0.39	0.25	0.32	0.29
Closed shrubs	0.48	0.29	0.42	0.36
Open shrubs	0.72	0.37	0.68	0.56
Woody savanna	0.46	0.28	0.44	0.37
Savanna	0.59	0.31	0.57	0.47
Grassland	0.72	0.39	0.70	0.59
Wetland	0.70	0.32	0.66	0.55
Cropland	0.76	0.40	0.69	0.58
Urban	0.54	0.30	0.50	0.42
Crop mosaic	0.66	0.36	0.59	0.50
Permanent snow	0.94	0.45	0.89	0.74
Barren/desert	0.87	0.42	0.78	0.65

The fixed values of spectral reflectance of sea ice in the original scheme have been updated for four distinct phases in the margin areas of the Arctic (winter stationary, spring melt season, summer stationary, and autumn freeze up) based on the work of *Zhang et al. (2003) and Belchansky et al. (2004).* Detailed information on the four classifications and surface reflectance during melt seasons will be described in the following section.

2.3.3 Surface spectral reflectance over sea ice during melt seasons

During the SHEBA project (October 30, 1997 through October 10, 1998) *(Perovich et al., 1999*), numerous studies were undertaken to analyze the surface heat budget of the Arctic *(Persson et al., 2002; Liu et al., 2005)* and to evaluate climate models against observations (*Inoue et al., 2006; Rinke et al., 2006).* A variety of parameters on the atmosphere, sea ice, and upper-ocean were collected and they included surface spectral reflectance over Arctic sea ice during the melt season. The SHEBA project provided the most comprehensive high quality information on surface properties and on surface SWR and longwave radiative fluxes in the Arctic. One of the largest across-model errors was in surface radiation flux simulations. Using the one-year SHEBA flux datasets (SWR, longwave, and turbulent), the analysis on the surface cloud forcing over the Arctic indicated that clouds warm the surface for most of the year, but have a brief cooling effect during early July *(Intrieri et al., 2002).*

Using 1-year of SHEBA observations, *Curry and Schramm (2001)* evaluated the snow/ice albedo parameterizations for model use and *Perovich et al. (2002)* provided a conceptual framework for the seasonal evolution of the albedo of multi-year Arctic sea ice. This relatively short-term data set obtained at a single location is limited in scope. In this thesis, a similar approach was applied to longer term satellite observations of SWR for the entire Arctic Ocean. As a first step there was a need to extend the specification of the spectral reflectance over sea ice to the entire Arctic

Ocean. Estimates on the melt onset dates, freeze onset dates, and the melt season duration and assignment of the corresponding spectral reflectance for these five phases (before melt, melt onset, during summer months, freeze onset, after freeze) were also needed. Based on previous studies *(Parkinson et al., 1992; Belchansky et al., 2004),* we have divided the Arctic Ocean into four regions according to melt and freeze onset dates as follows:

(1) Perennial ice: ice coverage is more than 50% during all months

(2) Annual ice: ice coverage is more than 50% in winter but less than 50% in September (the month with the minimum sea ice extent for a year)

(3) Low-latitude ice: ice coverage is less than 50% but more than 0% for all months

(4) Ocean: the ice coverage equals to 0% for all months.

For instance, the four regions in 2007 based on above definitions are illustrated in *Figure 2.8*. The melt and freeze Julian dates are then given for the four cases based on the work of *Belchansky et al. (2004) and Perovich et al. (2007)* as shown in *Table 2.4.*

Table 2.4 Julian dates of melt onset and freeze onset for Arctic perennial ice, annual ice, low-latitude ice, and ocean.

Ice cases	Melt onset date	Freeze onset date
Perennial ice	170	236
Annual ice	159	256
Low-latitude ice	90	273
Ocean	Missing value (-999.0)	Missing value (-999.0)

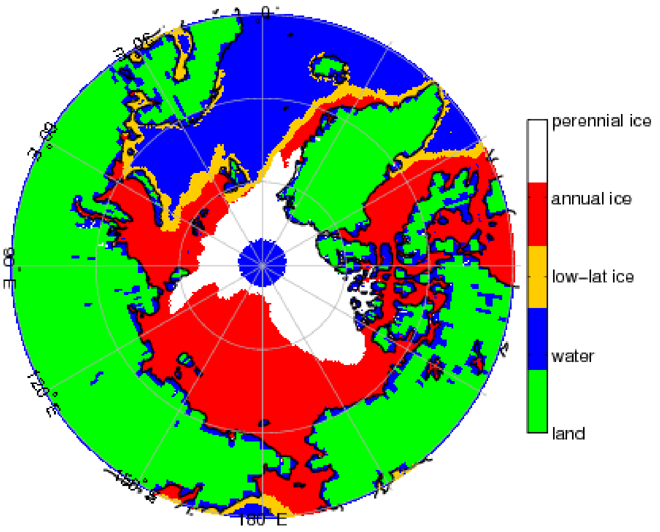

Figure 2.8 An example of Arctic region divided into perennial ice, annual ice, low-latitude ice, and water for year 2007 based on dates of sea ice melt onset and freeze up onset.

The following assumptions on the spectral reflectance in two bands (below 0.7 µm (VIS) and above 0.7 µm (NIR)) are made according to the timing of the five phases of sea ice as suggested by *Arnold et al. (2002)* and *Perovich et al. (2007):*

1. Before melt onset, the VIS reflectance has a constant value of 0.78 and the NIR reflectance is 0.4.
2. During 20 days since melt onset, the VIS reflectance linearly decreases from 0.78 to 0.5, and the NIR reflectance linearly decreases from 0.4 to 0.1.
3. During the summer months (20 days since melt onset till freeze onset), the VIS reflectance linearly decreases from 0.5 to 0.2 and the NIR reflectance remains at a value of 0.1.

4. During the 20 days since freeze onset, the VIS reflectance linearly increases from 0.2 to 0.78 and the NIR reflectance linearly increases from 0.1 to 0.4.

5. After 20 days since freeze onset, the VIS reflectance remains at a value of 0.78 and the NIR reflectance remains at 0.4.

The daily averaged surface SWR and albedo at Barrow for the year 2003 as derived from the original and updated versions of UMD_MODIS are shown in *Figure 2.9*. The downward fluxes are consistent for the two versions except during the melt seasons; there are large differences in the upward fluxes which affect the net fluxes, due to differences in surface albedo in the two versions. The surface albedo maintains a fixed value in the original version for the coastline, but the updated version can simulate the evolution of the albedo during ice melt and freeze.

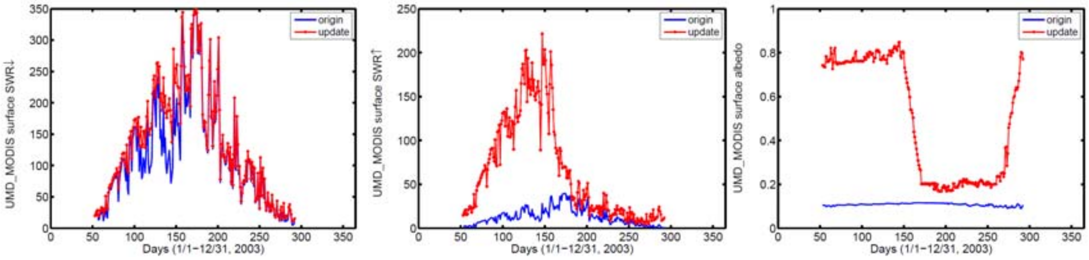

Figure 2.9 Daily averaged surface downward SWR, upward SWR, and albedo at Barrow for year 2003 derived from the original and updated version of UMD_MODIS.

2.3.4 Diurnal cycle and spatial gridding for UMD_MODIS 5-km data

The use of the high resolution MODIS (5-km) data is challenging, because the information is provided in swath format (up to 7 swaths per day at high latitudes). There is a need to merge swaths from different UTC times at the same day to get daily values. At the same time, the use of the swath information allows to capture the diurnal cycle of SWR at hourly time scale.

(1) Diurnal cycle representation

Terra and Aqua visit the Arctic Regions (north of 70° N) about 7 times each day (*Figure 2.1)* and represent well the diurnal variability of SWR at these latitudes. To fill for missing observations, we interpolate MODIS observations to obtain daytime SWR representative for each hour from sunrise to sunset. This approach uses an hourly averaged Solar Zenith Angle (SZA) to fill the missing data and to compute the hourly mean SWR.

The instantaneous UMD_MODIS SWR estimates from each swath were first corrected to the nearest central time of the local time intervals of 1 hour (referred as hour box) for each grid cell according to *Eq. 2.1* between sunrise and sunset.

$$F(t) = F(t_{obs})\mu(t)/\mu(t_{obs}) \tag{2.1}$$

Where t_{obs} is the time of observation, t is the nearest local central solar hour, $\mu(t_{obs})$ is the cosine of SZA at the observation time, $\mu(t)$ is the hourly mean cosine of SZA at time t, $F(t_{obs})$ are the instantaneous SWR estimates from UMD_MODIS model, and $F(t)$ are the hourly averaged SWR estimates for t.

In order to get SWR estimates when data were missing, filling was performed assuming constant cloud coverage between the missing hour box ($t_{missing}$) and the nearest hour box with values ($t_{nearest}$):

(a) if there was only one estimate available at the nearest hour box before or after the missing hour box, the SWR estimates at $t_{missing}$ ($F(t_{missing})$) were filled as the product of SWR at t_{nearest} ($F\ (t_{nearest})$) and the ratio of the cosine of SZA between the two hour boxes:

$$F(t_{missing}) = F(t_{nearest})\mu(t_{missing}) / \mu((t_{nearest}) \qquad (2.2)$$

(b) if there were two estimates available before and after the missing hour box, the $F\ (t_{missing})$ was produced by inversely weighting the two estimates by the time from the missing hour box.

$$F(t_{missing}) = \left(F(t_1)\left(t_2 - t_{missing}\right) + F(t_2)\left(t_{missing} - t_1\right)\right)/(t_2 - t_1) \qquad (2.3)$$

Where t_1 is the nearest hour box before missing hour box, t_2 is the nearest hour box after the missing hour box.

(c) if no estimate was available before or after the missing hour in a day, then $F\ (t_{missing})$ was set to a missing value.

A comparison between MODIS based hourly estimates of surface downward SWR within 5-km around the Barrow site against ARM observations for July 11-20, 2007 is shown in *Figure 2.10*. The black line represents the ground observations, and the red line represents the UMD_MODIS (5-km) SWR estimates. For July 10, 2007, the hourly averaged SWR estimates at all daylight hours from Terra (blue triangle), Aqua (green circle), MODIS hourly estimates using *Eqs. 2.2* and 2.3 (red), and ground observations (black) are illustrated in *Figure 2.11*. A scatter gram showing the performance of MODIS high resolution SWR estimates will be illustrated in *Chapter 3*.

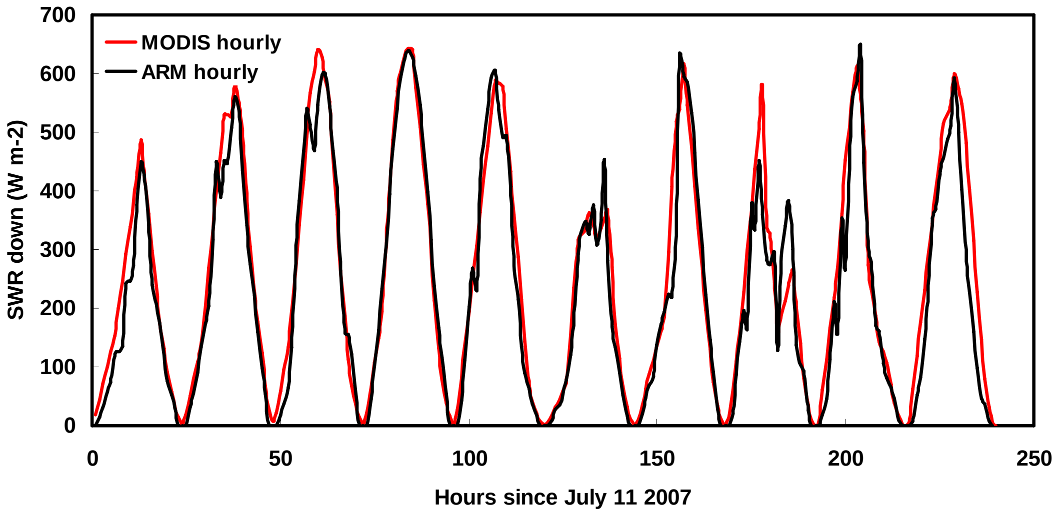

Figure 2.10 Hourly averaged surface downward SWR (Wm^{-2}) from UMD_MODIS estimates (5-km) with diurnal adjustment and from ARM surface observations for period of July 11-20, 2007 (UMD_MODIS: red line; ARM: black line).

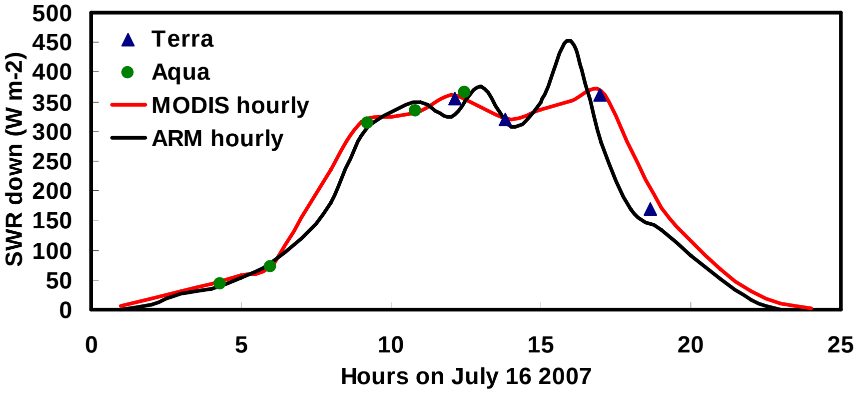

Figure 2.11 Hourly averaged surface downward SWR (Wm^{-2}) from UMD_MODIS estimates (5-km) and from ARM surface observations (Terra: blue triangle; Aqua: green circle; MODIS: red line; ARM: black line) for July 16 2007.

(2) Spatial gridding method

To merge all available swaths passing a given region, a spatial gridding method was implemented as a weighted average. For instance, an equal-area grid map at resolution of 0.25° (about 25-km at the equator) can be generated from the 5-km swath products as follows: for every grid cell, the first step is to search over the nearest region within a given radius (shown as R in *Figure 2.12*) e.g. 25-km around the center grid point. All the estimates found in the region are given a weight based on their distance to the center of the grid cell. The weighting is computed by using the *Cressman* interpolation scheme. For instance shown in *Figure 2.12*, there are three estimate points within the radius (R) around the center grid (i, j, and k), so the SWR value at the center grid is a linear combination of all the estimates at these three points and the corresponding weight, given by:

$$F = \frac{w_i F_i + w_j F_j + w_k F_k}{w_i + w_j + w_k} \tag{2.4}$$

Where *w* is a weight computed as:

$$w_i = \frac{R^2 - d_i^2}{R^2 + d_i^2}\,(d_i^2 \le R^2),\ w_i = 0\,(d_i^2 > R^2)$$

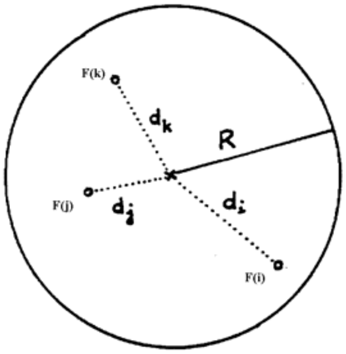

Figure 2.12 Demonstration of the gridding procedure. For instance, F (i) is the SWR estimates at the grid point (i), d_i is the distance from grid point (i) to the center grid, and R is the given radius of search.

For the instantaneous SWR estimates from UMD_MODIS, every swath was implemented according to the above gridding method. An example of UMD_MODIS (5-km) from two swaths for July 10, 2007 is illustrated in *Figure 2.13*. To derive the daily mean SWR values, the procedure to fill in the missing values at daytime hours as described above was applied for every grid cell. The daily mean SWR estimates for the whole Arctic Region for July 10, 2007 from UMD_MODIS (5-km and 1°) are shown in *Figure 2.14.* Such high-resolution SWR estimates are needed for high latitudes, especially for the marginal area, because the mixing of surface conditions (snow, ice, water, and land) along the coastlines cannot be well represented at lower resolution.

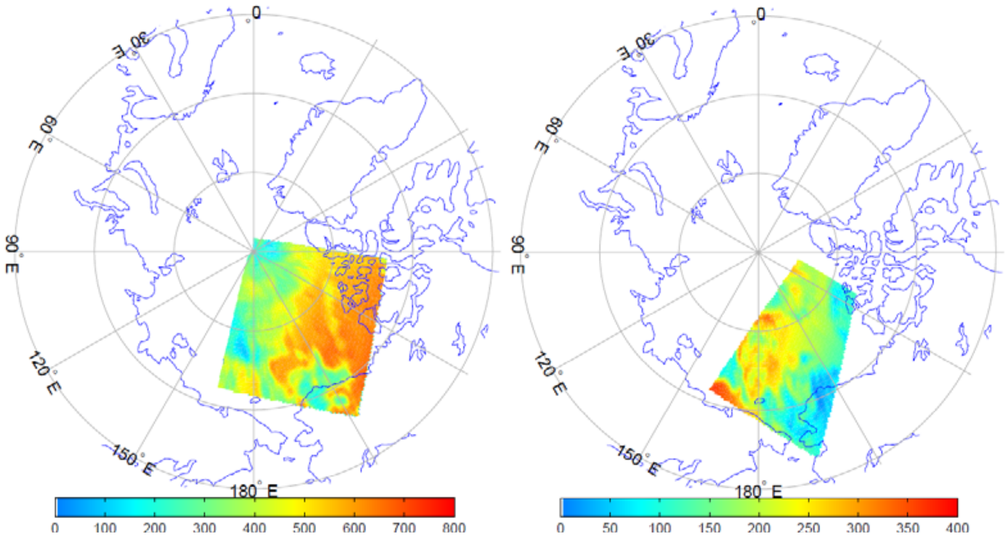

Figure 2.13 The instantaneous downward SWR (Wm^{-2}) estimated from UMD_MODIS Level-2 swath products (5-km) for the North Polar Regions from Aqua (UTC: 20:20) (left) and from Terra (UTC: 06:40) (right) for July 10, 2007.

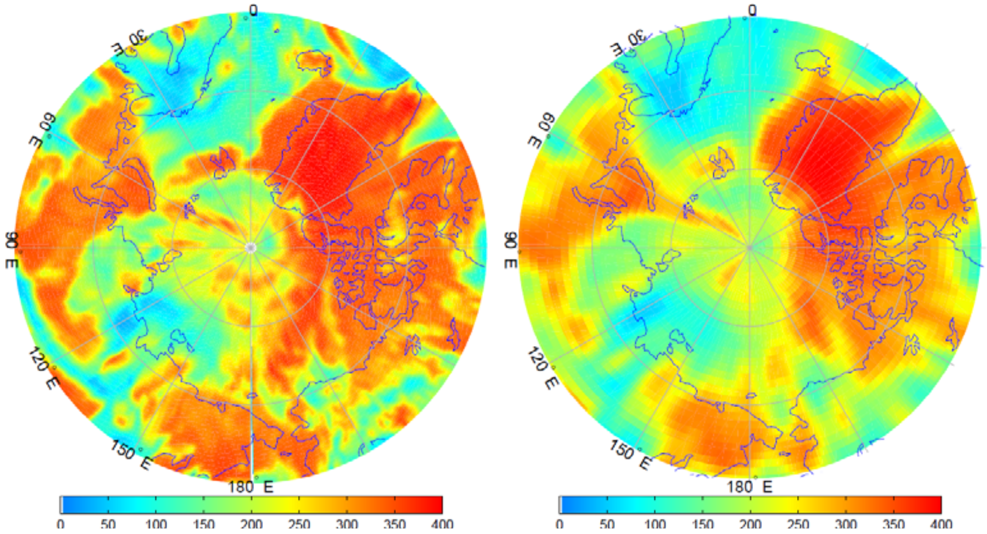

Figure 2.14 Daily mean surface downward SWR (Wm^{-2}) estimated from UMD_MODIS for the North Polar Regions at 5-km resolution (left) and at 1° resolution (right) for July 10, 2007.

2.4 Inference scheme for AVHRR (UMD_AVHRR)

2.4.1 The UMD_AVHRR inference scheme

Information on SWR from AVHRR on-board NOAA polar-orbiting satellites has been derived previously. Currently, there are several major AVHRR based SWR products. One is based on the Extended AVHRR Polar Pathfinder Project (App-x) *(Key and Schweiger, 1998; Key, 2001; Wang and Key, 2003, 2005).* The others are based on the International Satellite Cloud Climatology Project (ISCCP) observations *(Rossow and Shiffer, 1991).* The ISCCP observations are provided at global scale and are based on several geostationary satellites that cover the globe up to about 50°. The AVHRR sensor on polar orbiting satellites supplements the observations at higher latitudes. Therefore, all the various global products that use ISCCP observations are based on the AVHRR sensor at higher latitudes.

In this study we used the AVHRR narrowband radiances at TOA provided by ISCCP DX *(Rossow et al., 1996)* at a nominal resolution of 30-km every 3 hours that we gridded to an equal-area map about 50-km (about 0.5°) at the equator. We opted to use AVHRR observations from ISSCP instead of the App-x products because:

(1) ISCCP products provide improved cloud information including cloud optical depth (water cloud and ice cloud) than App-x.

(2) The App-x products are provided only until 2004; ISCCP based products are updated and continuing.

The implementation with AVHRR observations is based on the heritage of University of Maryland (UMD)/Shortwave Radiation Budget (SRB) model *(Pinker et al., 2007),* which has been developed and modified for use with different satellite observations (e.g., ISCCP D1, ISCCP DX, GOES, METEOSAT and GMS). The physical concept of this model differs with UMD_MODIS; while UMD_MODIS is applied in a forward mode, SWR from AVHRR will be derived in an inverse sense. Namely, the UMD_MODIS uses independently derived parameters to drive the inference scheme while calibrated radiances at the Top of the Atmosphere (TOA) are used as a starting point in the AVHRR case. The narrow-band satellite observations at the TOA need first to be transformed into broadband values (n/b) and corrected for bidirectional effects, before being used to derive partial information on the atmosphere. The general framework of the UMD_AVHRR model is illustrated in *Figure 2.15*. The critical elements of this inference scheme are:

(1) transformation from narrowband observations intro broadband values at TOA;

(2) correction for angular dependence of the observations by applying Angular Distribution Models (ADMs);

(3) derivation of aerosol and cloud optical depth (such information can also come from independent sources, such as MODIS, MISR, or GOCART (the Goddard Global Ozone Chemistry Aerosol Radiation and Transport model));

(4) information on surface albedo, detailed surface scenes (i.e., IGBP), and information on surface elevation.

The absolute radiometric values of ISCCP Stage B3 radiances have been normalized to that of the NOAA-9 AVHRR *(Brest and Rossow, 1992; Rossow et al., 1996)*. The AVHRR parameters from ISCCP DX data used in UMD_AVHRR model are: SZA and geometry angles, snow coverage, cloud fraction (for water and ice cloud phase), cloudy-sky radiance (for water and ice phase), clear-sky radiance, clear-sky composite radiance, cloud optical depth (for water and ice phase), and glint flag, as shown in *Table 2.5*. The spatial gridding procedure was also applied. For each grid cell, the program searched over a neighborhood of 100-km scale. All the observations found within such neighborhood were given a weight based on their distance to the center of the grid cell. The weighting curve is a Gaussian shape function with half width of grid size (equal to about 50-km (0.5°)) *(Ma and Pinker, 2011).*

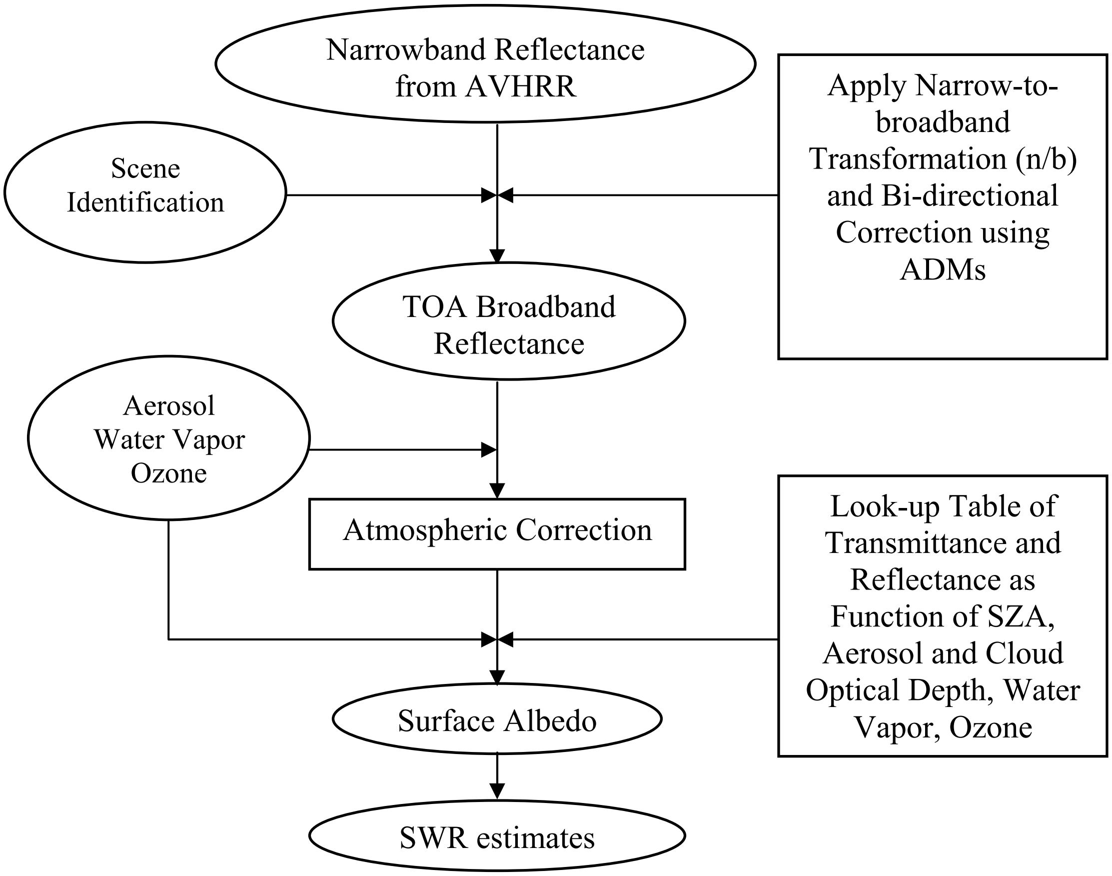

Figure 2.15 Flowchart of the inference scheme for deriving SWR estimates from AVHRR observations (UMD_AVHRR).

Table 2.5 Parameters from ISCCP DX used in UMD_AVHRR scheme.

Geometry and satellite information	**TOA radiance**
Cosine of solar zenith angle	Clear-sky radiance
Cosine of satellite zenith angle	Cloudy-sky radiance (water and ice phase)
Relative azimuth angle	Clear-sky composite radiance
Glint flag	
Cloud Fraction	**Atmospheric Auxiliary data**
Number of total pixels	Snow/ice coverage
Number of water cloud pixels	Column amount of water vapor
Number of ice cloud pixels	Column amount of ozone

2.4.2 Need for updates to UMD_AVHRR inference scheme

As shown in *Figure 2.16*, the time series of monthly mean surface downward SWR estimates from App-x and ISCCP-FD products underestimate the SWR in spring and overestimate the SWR in summer and autumn seasons when compared to surface measurements at Barrow, AK (BAR) (71.32° N, 156.61° W). The difference can reach 40~50 Wm^{-2}.

Newly developed n/b transformations and bi-directional corrections that account for high latitude conditions were implemented for the AVHRR observations. The improvements include: a) new n/b transformations using a detailed radiative transfer model; b) updates on surface information based on the International Geosphere/Biosphere Programme *(IGBP, 1993)* land use classifications; and c) improved bi-directional corrections based on simulations and CERES observations. The IGBP surface classifications are grouped into 12 types, which are based on IGBP surface classifications synthesized with University of Maryland land classification *(Hansen et al., 2000).* Studies have shown that the new CERES ADMs can greatly improve TOA instantaneous fluxes as compared to ERBE by up to+/- 50 Wm^{-2} with a strong dependence on scene type and viewing angle *(Wielicki, 2005*). The impact of the newly proposed methodologies was first tested with SEVIRI observations at low latitudes and was initially evaluated at the TOA (*Appendix A).*

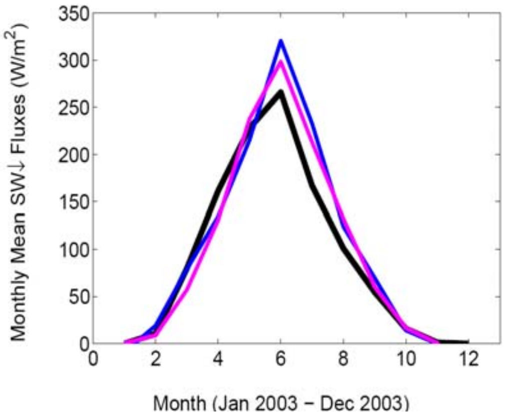

Figure 2.16 Monthly mean surface downward SWR estimates from satellites (blue: App-x products; magenta: ISCCP-FD products) and from ground measurements (black line) at Barrow, AK for year 2003.

2.5 Improvements to UMD_AVHRR inference scheme

2.5.1 MODTRAN_3.7 Simulations

Detailed models of atmospheric radiative transfer provide tools for simulating observations in both narrowband and broadband radiances. Relationships can be studied in a controlled way, because atmospheric, surface, and viewing geometry conditions can be varied systematically in the simulations, which is difficult to accomplish empirically.

In this study we used the MODTRAN_3.7 angularly dependent radiative transfer model *(Berk et al., 1983)* with 33 layers in the vertical, spectral range from 0 to 50000 cm^{-1} and a maximum resolution of 50 cm^{-1}. It provides direct, single-scattered, and multiple-scattered solar irradiance. Multiple scattering is accounted for with the use of the Discrete Ordinate Model (DISORT) *(Stamnes et al., 1988)*. In the simulations, 10 solar bins and 48 viewing bins (6 viewing zenith angles and 8 azimuth angles) are specified. The distributions of the Solar Zenith Angle (SZA), Satellite Viewing Zenith Angle (VZA), and Azimuth Angle (AZA) in MODTRAN_3.7 simulations are shown in *Table 2.6*. These viewing geometries were used to calculate spectral fluxes by integrating numerically using Gaussian quadrature points. The climatological profiles of temperature, ozone, water vapor grouped by season (20 profiles for each season) were used, which are derived from the TIROS Initial Guess Retrieval (TIGR) profiles *(Chedin et al., 1985)* modified with 4 years of rawinsond information from the Forest System Laboratory (FSL). For each season, the simulations utilize three visibilities (18, 23, and 28 km) to account for the variability of atmospheric aerosols with optical depth of about 0.33, 0.26, and 0.22 *(Bäumer et al., 2008).* For cloud simulations, the following six types of default clouds provided in MODTRAN_3.7 are used: cumulus, altostratus, stratus, stratocumulus, nimbostratus, and cirrus, which are stratified by Cloud Optical Depths (COD). Surface conditions are grouped into 12 classes based on the IGBP surface scenes *(Figure 2.17).* They include: Water, Needleleaf Forest, Broadleaf Forest, Mixed Forest, Woody Savannas, Savannas, Closed Shrubs, Open Shrubs, Grassland, Cropland, Bare Ground, and Snow/Ice.

Table 2.6 The distribution of SZA, VZA, and AZA in simulations.

SZA(°)	12.9	30.8	41.2	48.3	56.5	63.2	69.5	75.5	81.4	87.2
VZA(°)	11.4	26.1	40.3	53.8	65.9	76.3				
AZA(°)	1.91	9.97	24.18	44.02	68.78	97.55	129.31	162.89		

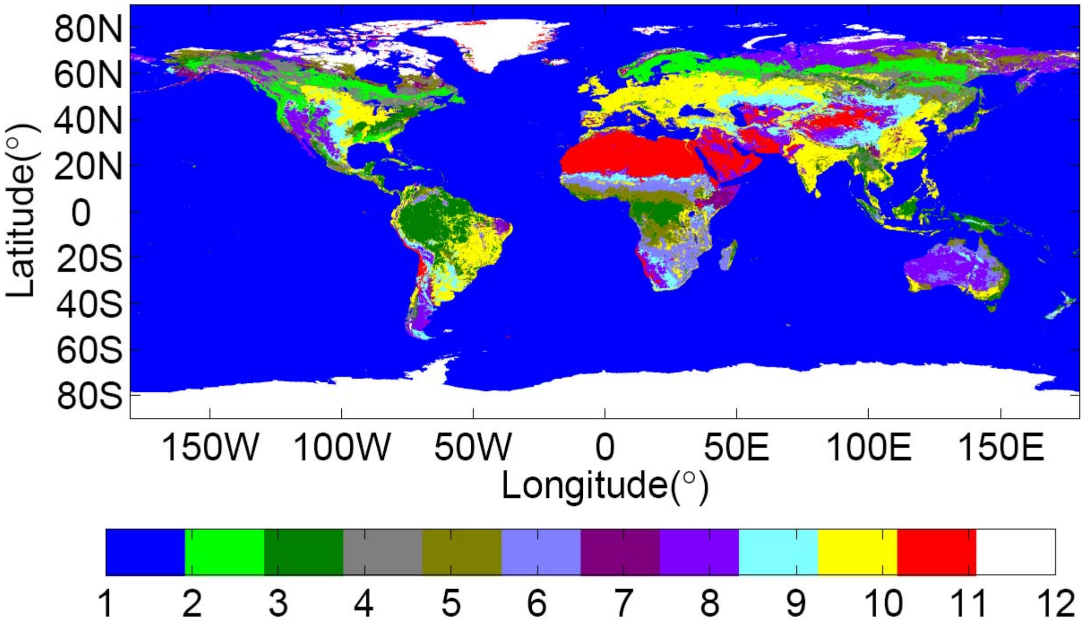

Figure 2.17 IGBP surface types used in simulations (the data are taken from IGBP surface classifications synthesized with University of Maryland land cover classification) and the scales represent the scene types:

1 =	Water	2 =	Needleleaf Forest	3 =	Broadleaf Forest
4 =	Mixed Forest	5 =	Woody Savannas	6 =	Savannas
7 =	Closed Shrubs	8 =	Open Shrubs	9 =	Grassland
10=	Crop/Mosaic	11=	Barren/Desert	12=	Snow/Ice

The spectral surface albedo is an important input for MODTRAN_3.7. In the simulation, there is a need to specify the spectral reflectance characteristics of the various surface types used. Such information is not readily available. In our simulations we used models developed by *Kassabova et al. (2002).* These spectral reflectance models are developed for the 12 IGBP surface classifications by using AVHRR channel 1 (0.58 to 0.68 μm) and channel 2 (0.725 to 1.1 μm) global monthly mean reflectance at the TOA from the *Briegleb et al. (1986)* albedo models updated with information from the Global Vegetation Index (GVI) dataset (*Gutman and*

Ignatov, 1998), and from the Advanced Space Thermal Emission and Reflection Radiometer (ASTER) library (*Gillespie et al., 1998),* thus introducing seasonality of spectral reflectance which as yet, has not been included in most available simulations. The ASTER spectral library is a compilation of almost 2000 spectra of natural and man-made materials from three different spectral sources: the Johns Hopkins University (JHU) Spectral Library, the Jet Propulsion Laboratory (JPL) Spectral Library, and the United States Geological Survey (USGS-Reston) Spectral Library. The spectral coverage is from 0.3 to 2.5μm *(Kassabova et al., 2002).* The output from simulations is TOA spectral reflected SW radiance at each viewing bin. The n/b transformation coefficients were derived based on these simulated radiances associated with the satellite response filter functions.

2.5.2 Updates on n/b transformation

The derivation of n/b transformation coefficients requires establishing a relationship between broadband and narrowband reflectance, which depend on the SZA, viewing geometry, surface and atmospheric conditions, clouds and spectral response of the satellite sensors. Three main computational steps are needed: (1) calculation of TOA spectral reflectance based on the simulated radiances for different surface types and cloud conditions for a range of solar and viewing angles; (2) calculation of narrowband reflectance and the simultaneous broadband reflectance at each viewing bin by convolution with the spectral response functions of satellite sensors; (3) establishment of n/b transformation relationships.

The TOA narrowband and broadband reflectances were calculated from the spectral radiance at each viewing configuration as simulated from MODTRAN_3.7 and the response functions of the satellite sensors, described in *Eq. (2.5)* and *Eq. (2.6)*:

$$\rho_{nb}(\theta_0,\theta,\phi)=\frac{\pi\int_{\lambda 1}^{\lambda 2} I(\lambda,\theta_0,\theta,\phi)G(\lambda)d\lambda}{\int_{\lambda 1}^{\lambda 2}\cos(\theta_0)S_0(\lambda)G(\lambda)d\lambda} \tag{2.5}$$

$$\rho_{bb}(\theta_0,\theta,\phi)=\frac{\pi\int_{0.2\mu m}^{4\mu m} I(\lambda,\theta_0,\theta,\phi)d\lambda}{\int_{0.2\mu m}^{4\mu m}\cos(\theta_0)S_0(\lambda)d\lambda} \tag{2.6}$$

Where, θ_0 is the Solar Zenith Angle (SZA); θ is the View Zenith Angle (VZA); φ is the Azimuth Angle (AZA); I (λ) is the reflected spectral radiance at wavelength λ; S_0 (λ) is the solar spectral irradiance; G (λ) are the spectral response functions of the satellite sensors; λ_1 and λ_2 are the spectral limits of the satellite spectral band.

The n/b transformation coefficients and offsets, c (θ_0, θ, φ) and d (θ_0, θ, φ), were obtained from linear regression of narrowband and broadband reflectance at each solar angular bin and viewing angular bin as follows:

$$\rho_{bb}(\theta_0,\theta,\phi)=c\ (\theta_0,\theta,\phi)\rho_{nb}\ (\theta_0,\theta,\phi)+d\ (\theta_0,\theta,\phi) \tag{2.7}$$

Where ρ_{nb} is the narrowband reflectance; ρ_{bb} is the broadband reflectance, c and d are the coefficients and offsets from regression.

The n/b transformation formulas were established dependent on both SZA and viewing angles.

2.5.3 Updates on bi-directional corrections

There is a need to synthesize the ADMs from CERES observations and model simulations. The CERES based ADMs used in the study only account for surface types in the Tropics which are not sufficient for high latitude applications, which will be mentioned in the following part. Also, there is an issue of under-sampling at high latitudes in the CERES ADMs needed to augment the empirical models with theoretical ones.

(1) CERES ADMs

The earth surface and cloud tops are not isotropic. The anisotropic factor R (θ_0, θ, φ) is introduced as:

$$R(\theta_0,\theta,\phi)=\frac{\pi I(\theta_0,\theta,\phi)}{F(\theta_0)} \tag{2.8}$$

where I (θ_0, θ, φ) is the reflected radiance at angle (θ_0, θ, φ); F (θ_0) is the irradiance.

The ADMs that were developed utilize the CERES models, which are derived from the multi-angle radiance measurements from the rotating azimuth plane scanning mode of CERES instruments onboard the Tropical Rainfall Measuring Mission (TRMM) and Terra and Aqua satellites *(Loeb et al., 2003, 2005).* In the CERES observing system, there are 5 instruments to provide angular sampling, using 3 channels per instrument: Shortwave (0.3-5.0 μm) – Reflected solar radiation; Total (0.3-200 μm) – Earth emitted radiation; Window (8-12 μm) – Thermal infrared emission. Collocated cloud and aerosol information was also derived from the MODIS observations.

Two ADM products are available from CERES: one is derived from nine months of TRMM observations (January to August of 1998 and March 2000) known as CERES-TRMM ADMs (*Loeb et al., 2003);* and the other one is derived from two years of Terra observations (March 2000 to February 2002) known as CERES-Terra ADMs *(Loeb et al., 2005).* The CERES-TRMM ADMs are provided in a tabular format at each viewing angle; the CERES-Terra ADMs are provided in tables only for surface type of snow/ice, which were constructed by the sorting-into-angular-bins (SABs) method (*Suttles et al., 1992; Loeb et al., 2003).* These data are available at CERES ADMs website (http://asd-www.larc.nasa.gov/Inversion/adm/adm.html). The CERES-Terra ADMs for situations other than snow/ice are generated as continuous functions of imager-based retrievals from CERES SSF (Single Scanner Footprint TOA/Surface Fluxes and Clouds developed by *Geier et al. (2003)* data within 1° latitude × 1° longitude equal area, which use analytical functions dependent on SZA and represent the CERES radiance dependent on scene type and a range of values of specific atmospheric parameters *(Loeb et al., 2005)* (not possible to put into a convenient tabular form as in TRMM ADMs). The CERES-Terra ADMs for snow/ice and the CERES-TRMM ADMs for other surface types and cloudy sky are utilized in this study. The CERES ADMs that are useful for various surface types found at high latitudes were used for obtaining bidirectional corrections at the TOA *(Figure 2.18).*

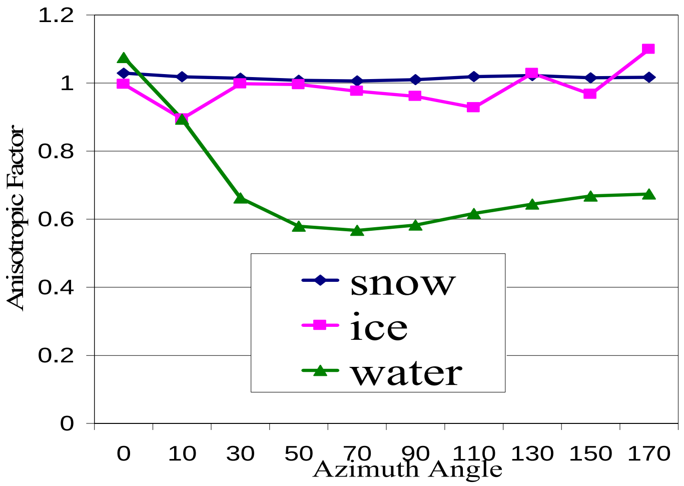

Figure 2.18 CERES ADMs for different surface types (clear sky) For Solar Zenith Angles: 40º-50º; Viewing Angles: 20º-30º.

For cloudy sky, the bi-directional corrections as based on CERES cloud ADMs *(Loeb et al., 2003, 2005)* are classified according to Cloud Optical Depth (COD) and cloud phase (liquid water cloud, ice cloud) over ocean, low-mod (low to moderate shrubs or trees) shrub/tree, mod-high shrub/tree (moderate to high shrubs or trees), desert, and snow/ice *(Table 2.7).* The CERES liquid water cloud ADMs over ocean are illustrated in *Figure 2.19* as a function of cloud optical depth, VZA, and AZA in an SZA interval of 50°-60°.

The CERES-TRMM clear-sky ADMs are generated by grouping the IGBP land classifications over the Tropics into four categories: Low-Mod Tree/Shrub, Mod-High Tree/Shrub, dark desert, and bright desert *(Loeb et al., 2003).*

Table 2.7 Cloud classifications in CERES ADMs (based on CERES ADMs' website and *Loeb et al., 2005*).

Scene		Cloud Optical Depth (COD)	Cloud Phase
Ocean		14 COD intervals: 0.01-1.0; 1.0-2.5; 2.5-5.0; 5.0-7.5; 7.5-10.0; 10.0-12.5; 12.5-15.0; 15.0-17.5; 17.5-20.0; 20.0-25.0; 25.0-30.0; 30.0-40.0; 40.0-50.0; COD>50.0	Liquid Water Cloud Ice Cloud
Low-Mod Shrub/Tree		6 COD intervals: 0.01-2.5; 2.5-6.0; 6.0-10.0; 10.0-18.0; 18.0-40.0; COD>40.0	Liquid Water Cloud Ice Cloud
Mod-High Shrub/Tree			
Desert	Bright Dark		
Permanent Snow	Bright Dark	2 COD intervals: COD>10.0 COD<=10.0	None
Fresh Snow	Bright Dark		
Sea Ice	Bright Dark		

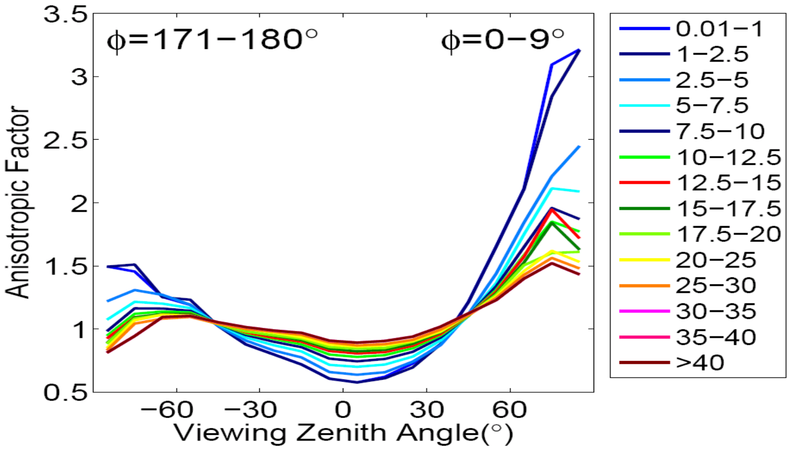

Figure 2.19 The CERES anisotropic factors for liquid water clouds over ocean as a function of cloud optical depth, viewing zenith angle, and relative azimuth angle in a solar zenith angle interval of 50°- 60° (based on CERES ADMs' website and *Loeb et al. (2005)).*

(2) Theoretical ADMs

The theoretical ADMs are based on model simulations. To derive the bi-directional distribution functions R (θ_0, θ, φ) from MODTRAN_3.7 simulated TOA radiance, there is a need to derive broadband hemispherical fluxes. The spectral radiances were derived by integrating the MODTRAN_3.7 simulated TOA spectral directional radiances over 48 viewing bins (*Table 2.3)* following *Kassabova et al. (2002):*

$$F_\lambda = \int_0^{2\pi} d\varphi \int_0^1 \mu I_\lambda(\mu,\varphi) d\mu \tag{2.9}$$

where F_λ is the spectral radiance; μ is the cosine of view zenith angle; φ is the azimuth angle; I_λ is the radiance in the given direction.

This integration is done by using Gaussian quadrature points which are given in the range of (0, 1). The abscissas and corresponding weights for azimuth angles and nadir angles are shown in *Table 2.8*. The spectral radiances were calculated as a weighted sum of radiances in the direction of the Gaussian angles *(Kassabova et al., 2002):*

$$F_\lambda = 4\pi \sum_{j=1}^{N} w_j \sum_{i=1}^{M} w_i \mu_i I_\lambda(\mu_i, 2\pi\varphi_i) \tag{2.10}$$

where M is the number of Gaussian points in the vertical; N is the number of Gaussian points in the horizontal; φ is the Gaussian angle; and w is the corresponding weight.

The SW broadband fluxes at TOA were calculated by integrating over wavelength in the entire SW spectral interval (0.2-4.0 μm) as follows:

$$F = \int_{0.2\lambda m}^{4\lambda m} F_\lambda d\lambda \tag{2.11}$$

The anisotropic factor $R\ (\theta_0,\ \theta,\ \varphi)$ was obtained at each angular bin as:

$$R(\theta_0, \theta, \phi) = \frac{\pi I(\theta_0, \theta, \phi)}{F} \tag{2.12}$$

Table 2.8 The abscissas and corresponding weights for viewing bins.

Nadir angle(°)	103.68	114.06	126.25	139.68	153.92	168.55		
Weight	0.237	0.408	0.592	0.763	0.898	0.980		
Azimuth angle(°)	1.91	9.97	24.18	44.02	68.78	97.55	129.31	162.89
Weight	0.136	0.311	0.476	0.623	0.748	0.846	0.913	0.947

(3) Issues related to the selection of optimal clear-sky ADMs

CERES-TRMM clear-sky ADM classification by surface types does not fully match the IGBP surface classification. For clear sky, CERES-TRMM ADMs have been developed for groups of several land types of IGBP resulting in only six surface types *(Table 2.9).* Generally, the CERES ADMs for an individual IGBP type within a group do not deviate significantly from each other or from the group mean value; larger differences do occur at high viewing zenith angles *(Loeb et al., 2003*). Needed are ADMs as appropriate for the twelve IGBP surface classifications, to be consistent with the classifications used in the n/b transformations. The simulated ADMs were developed for twelve land classifications based on IGBP, and there are differences between the observed and simulated ADMs for same surface types. An example of differences is illustrated for clear sky over a savannas scene in *Figures 2.20 (a) and (b).* Large differences occur at higher viewing angles. In order to derive consistent bi-directional corrections for IGBP land classifications and to improve the accuracy in the under-sampled angular bins, the two types of ADMs were synthesized to generate combined ADMs by weighting based on sample frequency. The methodology to generate the combined ADMs will be described in the following part.

Table 2.9 Surface classifications in clear-sky CERES-TRMM ADMs and the corresponding 12 IGBP surface scenes (based on *Loeb et al. (2003)*).

CERES surface scenes	IGBP surface scenes
Ocean	Water
Low-Mod Tree/Shrub	Savannas Grasslands Crops/ Mosaic
Mod-High Tree/Shrub	Needleleaf Forest Broadleaf Forest Mixed Forest Closed Shrubs Woody Savannas
Dark Desert	Open Shrubs
Bright Desert	Barren/Desert
Snow/Ice	Snow/Ice

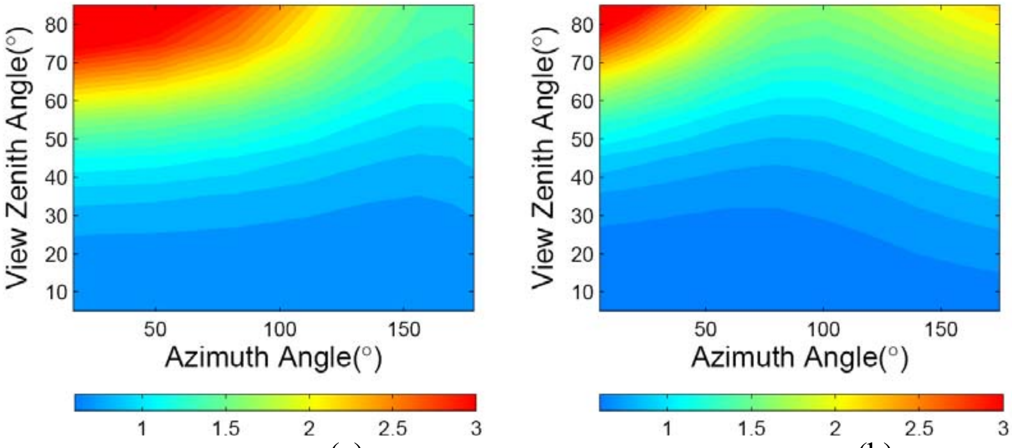

(a) (b)

Figure 2.20 Anisotropic Factors at SZA of 75.5° over savannas for clear sky conditions. (a) model simulations; (b) CERES observations.

(4) Development of synthesized clear-sky ADMs

The synthesized ADMs were generated from a combination of simulated and CERES observational anisotropic factors for each angular bin, using the following weighting:

$$\overline{R}(\theta_0,\theta,\phi)=\frac{1}{m+n}\left(mR_{CERES}(\theta_0,\theta,\phi)+nR_S(\theta_0,\theta,\phi)\right) \tag{2.13}$$

Where $\overline{R}$ (θ_0, θ, φ) are the synthesized ADMs at each angular bin; R_{CERES} are CERES ADMs; R_{S} are simulated ADMs; m is the number of samples at each angular bin in CERES ADMs; n is the number of samples at each angular bin in the simulated ADMs.

As an example, CERES Low-Mod Tree/Shrub ADMs were grouped from observations of the following three IGBP surface scenes: Savannas, Grassland, and Crops/Mosaic (*Loeb et al., 2003),* as shown in *Table 2.6*. The difference in the anisotropic factors between the synthesized and CERES ADMs for Savannas is shown in *Figures 2.21 (a) and (b).* At lower viewing zenith angles the percentage of differences is mostly within +/- 10% but the differences are much larger at higher viewing zenith angles.

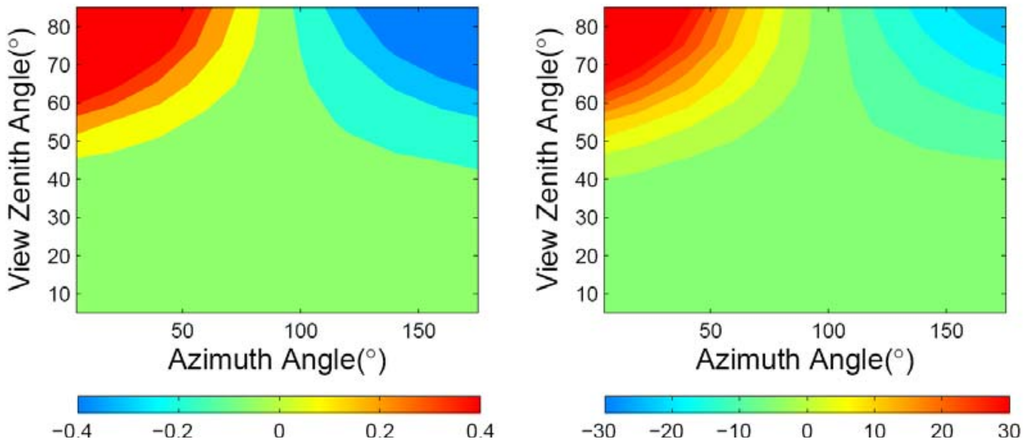

(a) (b)

Figure 2.21 Distribution patterns of the difference of the anisotropic factors between synthesized and CERES-only ADMs over Savannas for clear sky condition at SZA of 70-80° (a): Difference (synthesized – CERES ADMs) (b): Percentage of Difference (Difference/CERES ADMs).

2.5.4 Updates on n/b transformation for AVHRR at high latitudes

ISCCP_DX provides AVHRR narrowband radiance measurements at one shortwave band (0.6 µm wavelength). The visible radiances from different NOAA-series satellites have been normalized to the NOAA-9 instrument as the calibration reference standard *(Brest and Rossow, 1992).* Therefore, the n/b transformation for ISCCP_DX/AVHRR is based on NOAA-9 spectral response function at band 0.6 µm. The n/b transformation equation for AVHRR is:

$$\rho_{bb}^{est} = c\rho_{nb}(0.6) + d \tag{2.14}$$

Where c and d are coefficients and offsets.

For cloudy sky, the n/b transformations were applied according to Cloud Optical Depth (COD). The coefficients are based on ten COD intervals (0-0.8, 0.8-1.2, 1.2-1.8, 1.8-3.2, 3.2-5.8, 5.8-8.2, 8.2-15.8, 15.8-32.2, 32.2-50.0, >50.0). The information of cloud optical depth is from the ISCCP stage DX pixel level cloud products.

The oceans at high latitude have much lower surface albedo than snow or ice within the visible spectrum *(Figure 2.22).* The melting from snow/ice to water has an enormous effect on the ice-albedo feedback, which requires taking into account the variation of surface features for improvements in SWR estimates at high latitudes. A sensitivity tests were used to estimate the effect of the evolution of surface types on the SWR estimates.

The sensitivity test was based on the Santa Barbara Discrete ordinate Atmospheric Radiative Transfer Model (SBDART). The SBDART model combines the sophisticated discrete ordinate radiative transfer module, low-resolution atmospheric transmission model, and Mie scattering module *(Wang, 2007).* It is run with four streams for shortwave spectrum (0.2-4 μm) at 0.005 μm resolution for clear and cloudy conditions.

The surface albedo varies from 0.0 to 1.0 with specified sub-Arctic Summer atmosphere for (1) clear sky; (2) water cloudy sky with a uniform cloud layer placed between 1 and 5 km with cloud optical depth of 10.0 and cloud droplet effective radius of 8 μm; (3) ice cloudy sky with a thin ice cloud layer located between 10.5 and 11 km with cloud optical depth of 1.0 and cloud effective radius of 20 μm. The variation of surface downward and upward fluxes and TOA upward fluxes corresponding to different surface albedos are presented in *Figure 2.23* (a: clear sky; b: water cloud; c: ice cloud). For clear sky, when the surface albedo changes from 0.0 to 1.0, the surface downward SWR change about 25 Wm^{-2} (7% of mean value), and the surface upward and TOA downward SWR change about 340 Wm^{-2} (200%) and 297 Wm^{-2} (158%) respectively; for the water cloudy sky, the surface downward and upward SWR and TOA upward SWR change about 130 Wm^{-2} (78% of mean value), 245 Wm^{-2} (248%) and 102 Wm^{-2} (34%) respectively; and for the ice droplet cloud situation, the surface downward and upward SWR and TOA upward SWR change about 61 Wm^{-2} (25% of mean value), 271 Wm^{-2} (214%) and 192 Wm^{-2} (75%) respectively. It is expected that the variations in surface albedo have an enormous effect on surface upward SWR estimates (over 200% variation).

The SBDART was also run with different surface albedos for the 3 different surface types at high latitudes *(Figure 2.22):* snow, ice, and sea water. The output spectral radiances within the shortwave spectrum (0.2-4.0 μm) for surface downward, upward, and net radiances, and TOA upward radiances under the clear sky, water cloudy sky, and ice cloudy sky are shown in *Figures 2.24, 2.25, and 2.26,* respectively. For clear sky, the surface downward radiances at all spectra are similar for the three surface types but the surface upward radiances differ, which results in differences of surface net and TOA upward radiances. For water clouds, the comprehensive effect of absorption, reflection and scattering of water cloud droplets and surface albedo affected the variations in surface upward and net radiances for different surface types. There is not much difference in the TOA upward radiances because of the great effect of reflection of water cloud droplets. The results under ice cloudy sky are similar to clear sky but the amplitudes of the variations are smaller than clear sky.

The sensitivity tests indicate that changing surface albedos from snow/ice to sea water can greatly affect the SWR estimates. The melting of snow and sea ice during summer months can greatly change the surface albedos (from 0.8 to ~0.07); therefore there is a need to consider the evolution of surface types at high latitudes to improve the SWR estimates.

The new updates of n/b transformation and bi-directional corrections were also implemented with the DX_AVHRR observations at high latitudes by *Ma and Pinker (2011).* The pixel size is 30 km and the period of coverage is 1983 - 2006. Some days may be missing because of missing or invalid AVHRR data. The annual mean (1983-2005) surface downward SWR estimates from the updated UMD_AVHRR at a global scale and at the Arctic region are illustrated in *Figure 2.27*. The evaluation results against surface measurements will be discussed in detail in the *Chapter 3.*

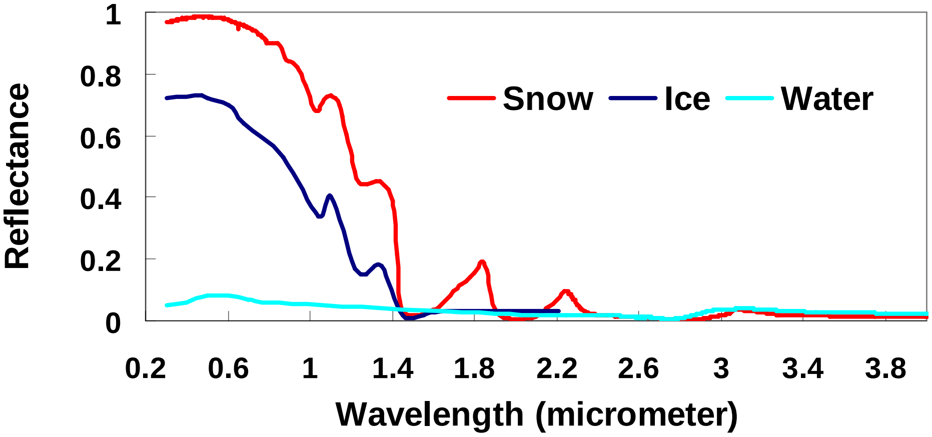

Figure 2.22 Spectral reflectance of different surface types (snow, ice, and water).

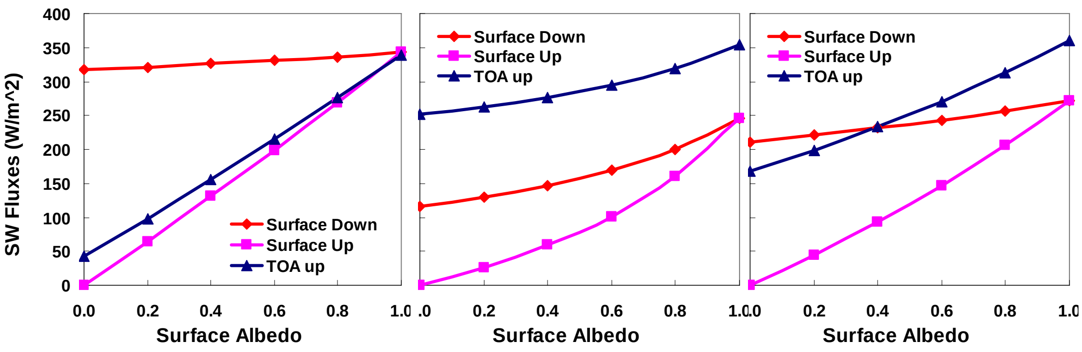

(a) (b) (c)

Figure 2.23 The surface downward SWR, upward SWR and TOA upward SWR corresponding to different surface albedos for: (a) clear sky; (b) water cloud sky; and (c) ice cloud sky conditions.

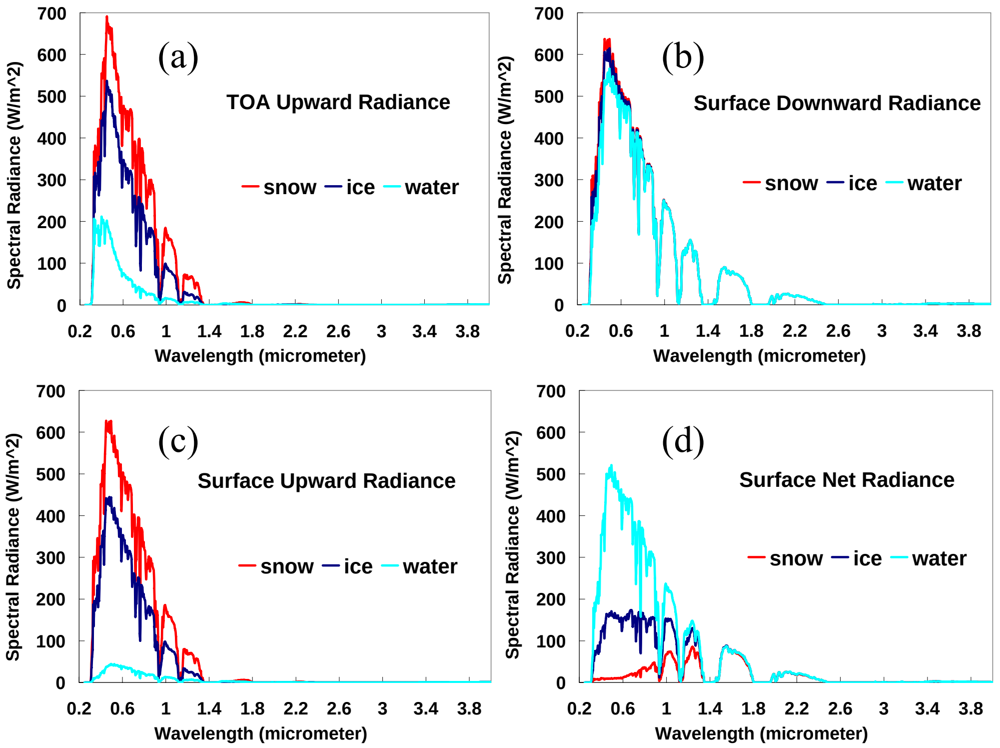

Figure 2.24 Spectral radiances for (a) TOA upward, (b) surface downward; (c) surface upward; and (d) surface net radiances over different surface types (snow, ice, and water) under clear sky.

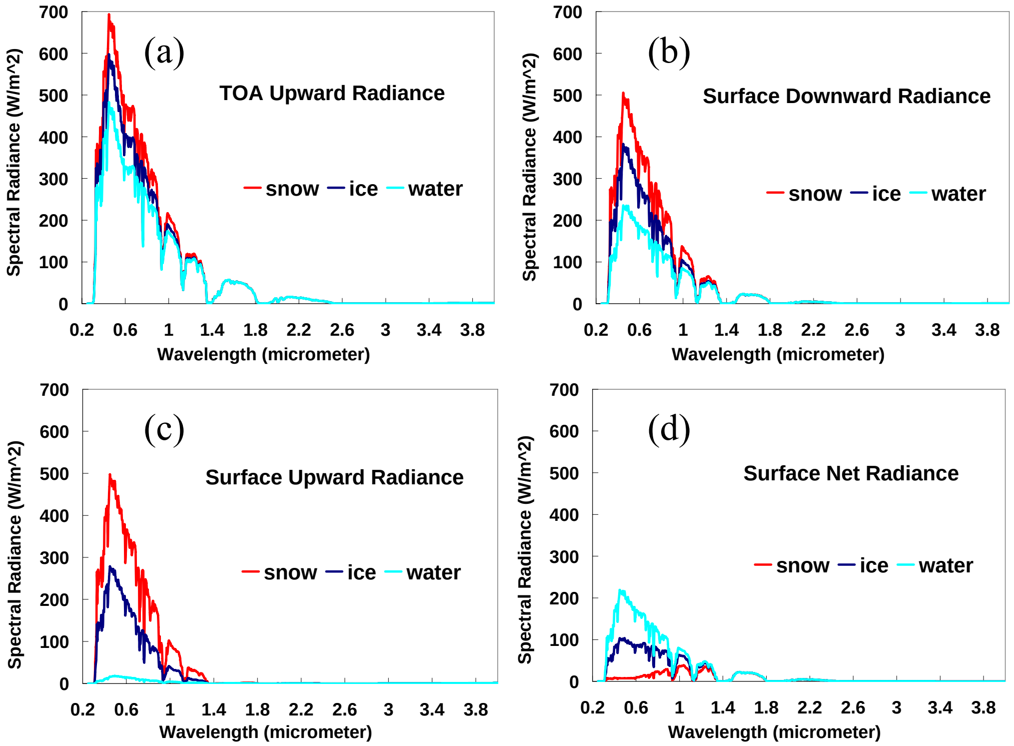

Figure 2.25 Spectral radiances for (a) TOA upward, (b) surface downward; (c) surface upward; and (d) surface net radiances over different surface types (snow, ice, and water) under water cloudy sky.

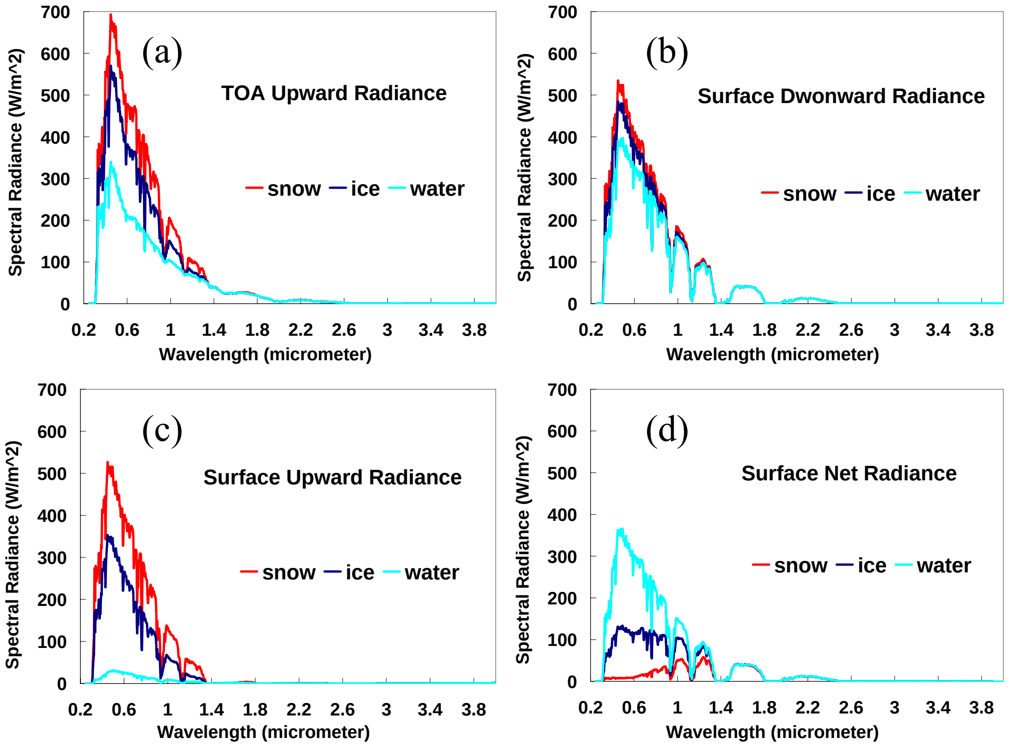

Figure 2.26 Spectral radiances for (a) TOA upward, (b) surface downward; (c) surface upward; and (d) surface net radiances over different surface types (snow, ice, and water) under ice cloudy sky.

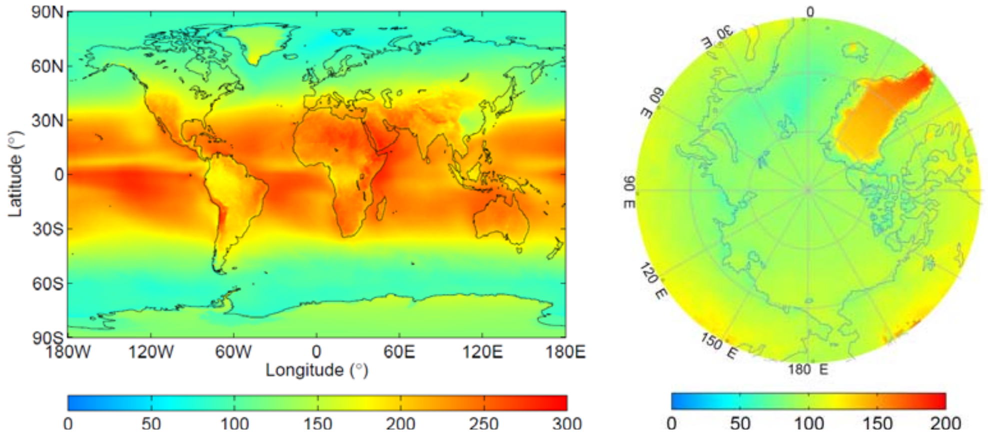

Figure 2.27 The annual mean (1983-2005) surface downward SWR (Wm-2) estimated from UMD_AVHRR at a global scale and at Arctic region (60° N-90° N).

Chapter 3: Results and Evaluations

Surface SWR estimates from the modified version of UMD_MODIS (at 1° for 2002-2010 and 5-km for 2007) were evaluated against measurements over land and buoy sites at high latitudes. Results from the UMD_AVHRR version (at 0.5° for 1983-2006) were also evaluated against measurements at land sites.

3.1 Evaluations of updated UMD_ MODIS model (1°)

3.1.1 Evaluations against land ground measurements

The updated UMD_MODIS model (1°) was evaluated against the high quality ground measurements from both the Baseline Surface Radiation Network (BSRN) *(Ohmura et al., 1998)* and form the Department of Energy Atmospheric Radiation Measurement Program (ARM) *(Stamnes et al., 1999; Ackerman and Stokes, 2003).*

(1) BSRN polar sites

The ground observations used in the evaluation process come from the BSRN observing stations (http://www.bsrn.awi.de/) *(Table 3.1).* The BSRN program was developed to provide earth's surface irradiance measurements for evaluation and improvement of satellite-based and climate model estimates of surface radiative fluxes *(Ohmura et al., 1998).* Over 40 stations distributed globally provide surface SWR measurements (direct and diffuse) at high accuracy and at high frequency (minutes). However, there are still a number of unsolved issues related to the performance of the broadband products. For instance, the uncorrected 'thermal offset problem', which refers to the detector sensitivity to the gradient of temperature within the instrument, can introduce a systematic 8~20 Wm^{-2} underestimation of diffuse sky radiation *(Philipona, 2002*). Not all of the BSRN stations are maintained at the same level of accuracy.

Six BSRN stations, considered of highest available quality, as listed in *Table 3.1* were used in the evaluation of the MODIS products. The evaluation was done for a three-year period, both at daily and monthly time scales *(Figure 3.1)*. For the monthly time scale, the correlation between the MODIS SWR estimates and BSRN observations is 0.98, the RMSE (Root-Mean-Square of error) is 22 Wm^{-2} (about 17% of the mean value), while the bias is -7.0 Wm^{-2} (about 5.5 % of mean value). At the daily time scale, the respective statistics are 0.97, 31 Wm^{-2} (23%) and -7.6 Wm^{-2} (5.6%). Results of evaluations after eliminating cases outside of 3 standard deviations (3-std) are presented in *Figure 3.2*. While quality control can be imposed on the ground measurements, it is more difficult to do so with the satellite observations. For various reasons, the data may include spurious errors. To eliminate these, the (3-std) limit is imposed which excludes only about 1~2% cases from the statistics and seems reasonable as shown in *Figures 3.1* and *3.2*. Results over land at daily time scale as reported in *Pinker et al. (2009)* for 18 land BSRN stations distributed over the globe had a bias of -3 Wm^{-2} and RMSE of 21 Wm^{-2}.

Table 3.1 Information on High Latitudes BSRN sites used.

BSRN Site	Abbrev.	Latitude	Longitude
NY-Ålesund, Spitsbergen	NYA	78.93° N	11.95° E
Barrow, Alaska	BAR	71.32° N	156.61° W
Georg von Neumayer, Antarctica	GVN	70.65° S	8.25° W
Syowa, Cosmonaut Sea	SYO	69.01° S	39.59° E
South Pole, Antarctica	SPO	89.98° S	24.80° W
Lerwick, United Kingdom	LER	60.13° N	1.18° W

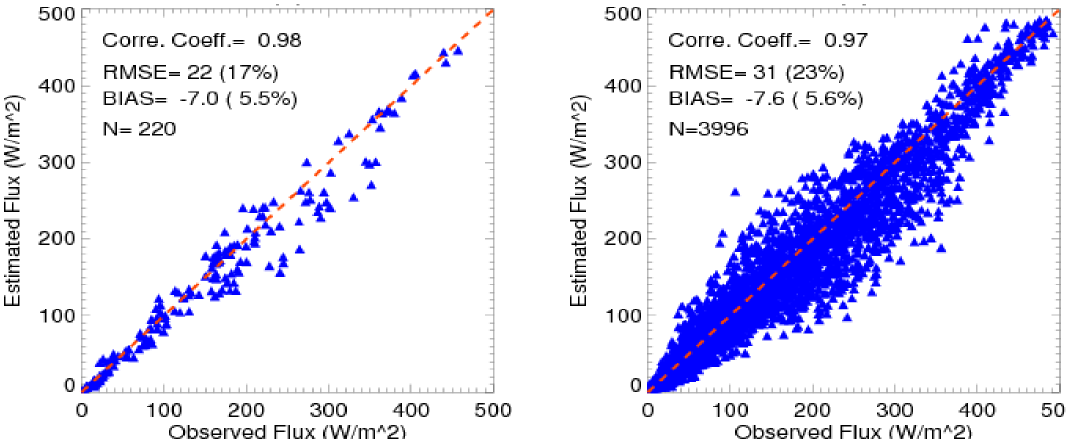

(a) (b)

Figure 3.1 (a) Evaluations of monthly mean downward SWR estimated from UMD_MODIS at six high latitude sites (N. Pole and S. Pole) as listed in *Table 3.1* for the period 2003-2006; (b) same as (a) for daily time scale.

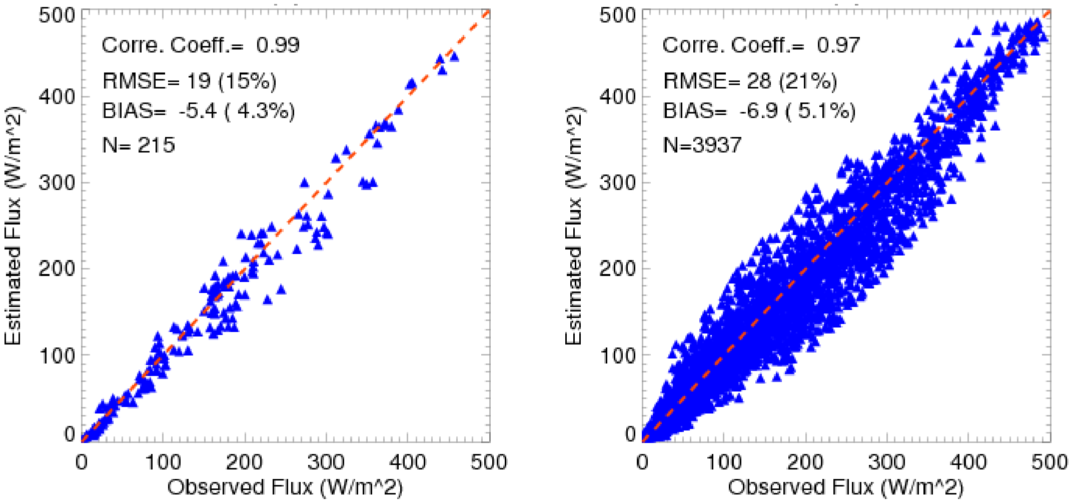

Figure 3.2 Same as *Figure 3.1* with removal of points outside 3-std (removed: 2.27% for monthly means and 1.47% for daily means).

(2) Summit site at Greenland

The Summit, Greenland site (72.58° N, 38.48° W) is at an elevation of 3208 m. Surface observations were taken under the International Arctic Systems for Observing the Atmosphere Observing Sites Project–Greenland Climate Network (GC-Net) available at: http://cires.colorado.edu/science/groups/steffen/gcnet/. More information on GC-NET can be found in *Steffen et al. (1996)*. These data were used for the evaluation of the MODIS SWR estimates for the period of 2003 – 2007 at a daily time scale *(Figure 3.3)*. The correlation is 0.99, the RMSE is 24.3 Wm^{-2} (about 14% of the mean value), while the bias is -5.7 Wm^{-2} (about 3.4 % of mean value).

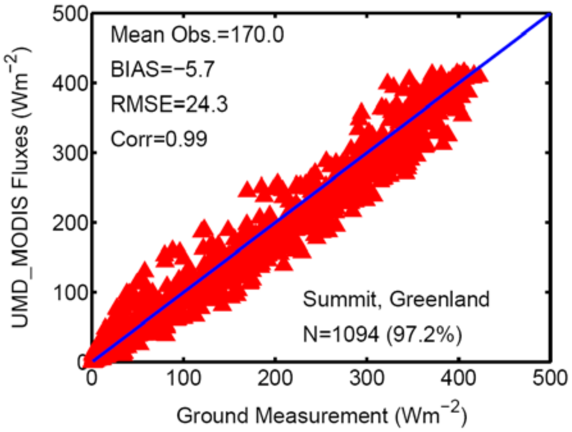

Figure 3.3 Evaluation of daily averaged surface downward SWR estimated from UMD_MODIS against ground observations at Summit, Greenland (72.58° N, 38.48° W) for the period of 2003-2007.

(3) ARM site (ARM_NSA) Barrow, AK

It has been documented that northern Alaska is one of the most significantly impacted regions by global warming. The evidence of environmental changes in the Arctic regions with a focus on Alaska has been summarized in *Hinzman et al. (2005).* Studies related to surface SWR in the Alaska region can be traced back to 1880s *(Ray, 1885)* while the first comprehensive measurement of SWR started in the early 1960s *(Maykut and Church, 1973; Zhang et al., 2003).* Numerous climate change related investigations over this region have been undertaken. In a comprehensive investigation using ten years of cloud and radiative flux observations collected at the Barrow site *Dong et al. (2010)* reported that the longwave cloud radiative forcing (CRF) has a high positive correlations (0.8-0.9) with cloud fraction, liquid water path, and radiating temperature while negative correlations for shortwave CRF. The variation patterns of the spectral ultraviolet and visible irradiances at Barrow for the period of 1991 to 2005 as related to the changes in ozone, cloudiness and surface albedo were dealt with in *Bernhard et al. (2007)*. CloudSat *(Stephens et al., 2002)* products illustrated that the reduced cloud fraction and enhanced downward SWR over the Western Arctic Ocean (120° W-180° W, 70° N +) from 2006 to 2007 contributed significantly to the 2007 record minimum sea ice extent (*Kay et al., 2008).* The complexity of understanding changes in the Alaskan region is due to the fact that the region is under the influence of both extra-tropical and Arctic synoptic activity and due to the many physical feedbacks in that region (such as ice-albedo feedback and cloud radiative feedback *(Stone et al., 2002, 2005)*).

The Department of Energy Atmospheric Radiation Measurement Program at North Slope of Alaska site (ARM_NSA) *(Stamnes et al., 1999; Ackerman and Stokes, 2003)* was designed to collect data on clouds and surface radiative processes. It has been maintaining an observational site at Barrow (71.32° N, 156.61° W) located at the northern most point in the United States since July 1997, 330 miles north of the Arctic Circle; it is a representative site for evaluating climate change in the western Arctic coastal zone *(Stone, 1997).* The monthly mean surface temperature ranges from -25° C during January-February to 4° C during July-August with an annual average of -11°C (based on 10 years of surface observations *(Dong et al., 2010)*). The focus of the measurements is on solar and thermal infrared radiation at the Earth's surface and relevant atmospheric parameters. Before the start of the ARM observations, many shorter term campaigns were conducted at high latitudes. One of the most notable programs in the Arctic Ocean was the Surface Heat Budget of the Arctic (SHEBA) experiment led by the National Science Foundation and the Office of Naval Research, for the period of October 1997 to October 1998.

The SWR at ARM_NSA site are collected from rotating shadowband radiometers and pyranometers. The multi-filter rotating shadowband radiometer (MFRSR) takes measurements of direct normal, diffuse horizontal and total horizontal components of the broadband solar irradiances using a silicon detector and these same parameters at six wavelengths at nominal wavelengths of 415, 500, 615, 673, 870, and 940 nm. A MFRSR head that is mounted to look vertically downward can measure upwelling spectral irradiances. The fundamental measurements are made in millivolts with accuracy of 0.06% of 250 millivolts and uncertainty of 0.06% of

250 millivolts *(Hodges and Michalsky, 2011).* An Eppley Precision Spectral Pyranometer (PSP) measures the hemispherical downward solar irradiance in the 280-2950 nm. The downward and upward SWR are based on these measurements that respond to radiation within a 2-pi steradian (hemispherical) field of view. The hourly mean observed SWR were generated by averaging the 60-minute observations and correcting to local time; and the daily mean SWR were obtained by summing the hourly values from sunrise to sunset and dividing by 24. The daily mean net SWR were computed as the difference of the downward and upward SWR, and the surface albedo was generated as a ratio of upward and downward SWR.

The information at the ARM_NSA is unique because it provides all the radiative components independently. This information is at high temporal resolution (from minutes to hours) but only at one location; satellite estimates can cover large regions but at much lower temporal resolution and at coarse spatial resolution (so far, satellite data utilized to derive SWR are from 25-km to 2.5°) *(Zhang et al., 2004; Wang and Key, 2005; Wang and Pinker, 2009).*

Eight years (July 2002-June 2010, Aqua started observations from 2002) of daily means SWR (down, up, and net) and surface albedo derived from the updated UMD_MODDIS (1°) were evaluated against the ground measurements at the ARM_NSA site. Results are presented in *Figure 3.4* after eliminating cases outside of 3-std (indicated in the figures as percentage of data eliminated). As evident, the bias is -5.3 Wm^{-2} (about -4% of mean values), -5.3 Wm^{-2} (-7%), 1.0 Wm^{-2} (1%), -0.001 (0%) for surface downward SWR, upward SWR, net SWR, and surface albedo, respectively. The values of the standard deviations (stds) are 22.9 Wm^{-2} (16%), 17.2 Wm^{-2} (24%), 15.8 Wm^{-2} (23%), and 0.077 (15%) for the four parameters. The correlations are 0.97. The UMD_MODIS values underestimate both the downward SWR and upward SWR, which reduces the bias of the net SWR.

The time series of eight year daily averaged downward SWR, upward SWR, and net SWR and surface albedo estimated from UMD_MODIS and as observed at the Barrow are shown in *Figure 3.5*. The UMD_MODIS estimates fit well with the observations and have the capability of capturing the seasonal variation of the properties in the margin areas of Arctic, which are generally considered as winter consistent (surface albedo of ~0.8), spring melt onset, summer consistent (surface albedo of ~0.2), and autumn freeze up. At Barrow, the downward SWR reaches a maximum during June (around the summer solstice); the upward SWR peaks about one month before the summer solstice when the surface albedo starts to fall as associated with the surface snow melt onset, which result in the increase of the net SWR; the surface net SWR reaches a peak around the summer solstice when the sun is higher and the albedo is lower than during the rest of the year; the surface albedo remains stable during the summer and start to increase around the autumnal equinox when the snow freezes up.

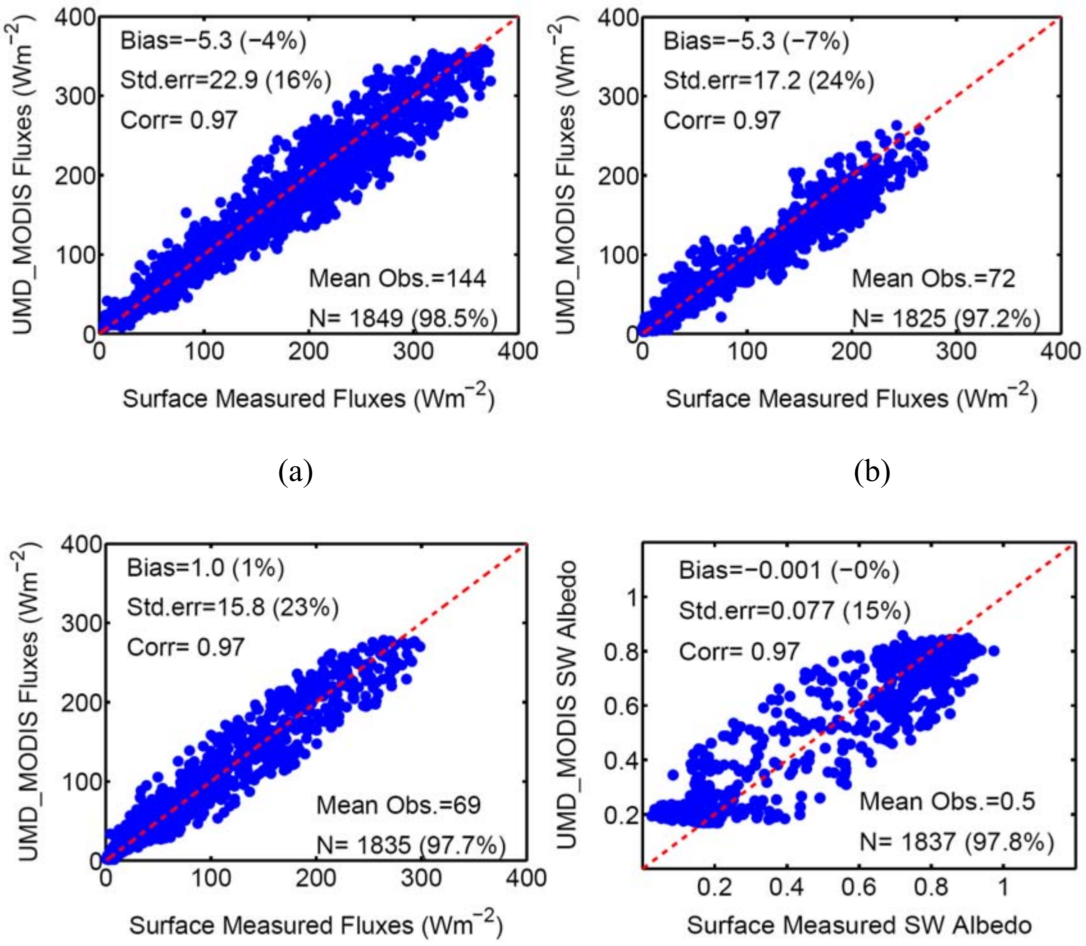

(a) (b)

(c) (d)

Figure 3.4 Evaluations of daily mean surface parameters from UMD_MODIS against surface measurements at Barrow from ARM_NSA for period of July 2002 to June 2010: (a) downward SWR; (b) upward SWR; (c) net SWR; (d): surface albedo.

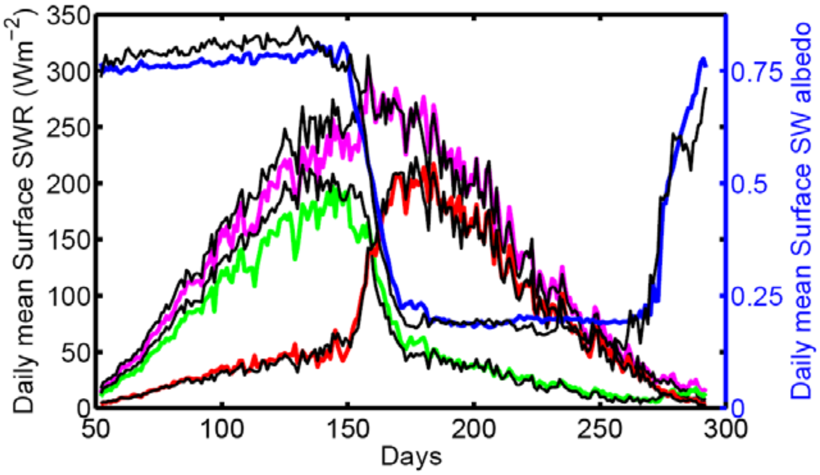

Figure 3.5 Time series of 8 years (July 2002-June 2010) of averaged daily mean surface parameters derived from UMD_MODIS (magenta: downward SWR; green: upward SWR; red: net SWR; blue: surface albedo) and from surface observations (black line) at ARM_NSA site.

Four satellite estimates (UMD_MODIS, NASA/LaRC, AVHRR, and UMD_D1) and NCEP/DOE II reanalysis (NCEP) and ERA_Interim reanalysis of SWR (down, up, and net) and surface albedo were evaluated against surface observations collected at ARM_NSA site for two years (2003-2004) at a daily scale when data from all sources are available. These products are described as follows.

(a) NASA/LaRC (1°)

The GEWEX Shortwave Radiation Budget (SRB) daily mean surface SWR (release-3.0, at 1° grid) for 1983-2007 were generated at NASA Langley Research Center (NASA/LaRC) and are available from: http://eosweb.larc.nasa.gov/PRODOCS/srb/table_srb.html#daily.

The data are derived with the shortwave algorithm of the NASA World Climate Research Programme/Global Energy and Water-Cycle Experiment (WCRP/GEWEX) Surface Radiation Budget (SRB) Project. The daily averaged values representative of local day are used since the surface daily observations are obtained at local time.

(b) AVHRR (25-km)

Information on SWR as generated from the Advanced Very High Resolution Radiometer (AVHRR) on-board NOAA polar-orbiting satellites is available. The specific data sets are the Extended AVHRR Polar Pathfinder (APP-x) project. The data are twice-daily composites for north and south Polar Regions *(Key and Schweiger, 1998; Key 2001; Wang and Key, 2003, 2005)*. The data cover the period 1982-2004 and as such, are of interest for long term needs. They are at a spatial resolution of 25-km for both Arctic and Antarctic (ftp://stratus.ssec.wisc.edu/pub/appx/).

The SWR were computed with the FluxNet model *(Key and Schweiger, 1998).* Evaluation of the hourly mean SWR against SHEBA field experiment data has yielded a bias of 12.5 Wm^{-2}, standard deviation (std) of 136.2 Wm^{-2}, and correlation of 0.95 for all seasons *(Liu et al., 2005).*

(c) UMD_D1 (2.5°)

The UMD_D1 radiative flux estimates are based on ISCCP stage D1 data *(Rossow et al. 1996)* as implemented with the University of Maryland Surface Radiation Budget Model (UMD/SRB) *(Liu and Pinker, 2008).* It utilizes shortwave radiances as observed from satellites at the TOA, transforms them into broadband fluxes, corrects for bi-directionality, estimates average optical properties of aerosols (from the clear sky radiances) and of clouds (from cloudy sky radiances) to be used in inferring the surface fluxes. It can be driven with satellite data from various sources such as the ISSCP D1 data, GOES, or METEOSAT. The UMD_D1 radiative estimates are provided globally at 2.5° spatial resolution, at 3 hourly, daily, and monthly time steps for 1983-2007.

(d) Reanalysis products (NCEP and ERA_Interim)

The NCEP/DOE AMIP-II Reanalysis (NCEP) products (provided by the NOAA/OAR/ESRL PSD, Boulder, Colorado, USA, from the website at: http://www.esrl.noaa.gov/psd/) are based on the NCEP/NCAR (National Centers for Environmental Prediction (NCEP) and National Center for Atmospheric Research (NCAR)) reanalysis by removing some errors and by updating the parameterizations of several physical processes. The products are global (T62 Gaussian grid) at temporal coverage of 4 times per day, daily mean, and monthly mean for the period of 1979 to 2010 *(Kanamitsu et al., 2002).* The surface downward and upward SWR is available at: http://www.esrl.noaa.gov/psd/data/gridded/data.ncep.reanalysis2.gaussian.html.

The ERA_Interim reanalysis product is a major improved version from ERA-40 undertaking by ECMWF (European Center for Medium-Range Weather Forecasts) with an improved atmospheric model and assimilation system. The ERA_Interim is based on 4-dimensional variational assimilation (4D-Var) rather than 3D-Var as in ERA-40. It also allowed higher resolution taking advantage of improved model physics. The dataset is available from 1982 to present and can be downloaded from either ECMWF website (http://data-portal.ecmwf.int/data/d/interim_daily/) or NCAR website (http://dss.ucar.edu/). The spatial and temporal resolution and the time period of all these products are shown in *Table 3.2*.

The evaluations of the daily averaged downward SWR from the satellites and from NCEP and ERA_Interim reanalysis products against ARM_NSA surface observations are presented in *Figure 3.6*. The results show that the bias is -3.6 Wm^{-2} (-2% of mean value), 7.0 Wm^{-2} (5%), 9.5 Wm^{-2} (6%), 10.9 Wm^{-2} (7%), 51.8 Wm^{-2} (34%), and -24.1 Wm^{-2} (-17%), respectively, for UMD_MODIS, NASA/LaRC, AVHRR, UMD_D1, NCEP, and ERA_Interim. The values of the stds are 22.6 Wm^{-2} (15%), 46.8 Wm^{-2} (31%), 51.0 Wm^{-2} (34%), 42.2 Wm^{-2} (28%), 51.4 Wm^{-2} (34%), and 43.4 Wm^{-2} (31%), and the correlations are 0.97, 0.88, 0.84, 0.89, 0.87, and 0.88 for UMD_MODIS, NASA/LaRC, AVHRR, UMD_D1, NCEP, and ERA_Interim. Compared to the other satellite and reanalysis products, the UMD_MODIS product has a lower bias and standard deviation and higher correlation. For the reanalysis products, NECP overestimate the SWR but ERA_Interim underestimate the SWR.

The time series of daily mean SWR (downward, upward, and net) and surface albedo at ARM_NSA site for the year 2003 is illustrated in *Figure 3.7*. The UMD_MODIS estimates are in good agreement with observations while the NCEP reanalysis results seem to have some problems, particularly during the snow-melt season. The statistics for the surface downward SWR, upward SWR, net SWR, and surface albedo are summarized in *Table 3.3*.

Table 3.2 Satellite and reanalysis products of SWR estimates.

Name of Data sets	Organization	Spatial Res.	Temporal Res.	Time Period
UMD_MODIS	Univ. of Maryland	1°	Twice per day; daily	2002-2010
NASA/LaRC	NASA/Langley	1°	3 hourly; daily; monthly	1983-2007
AVHRR	CIMSS/Polar Remote Sensing and Climatology Group	25 km	Twice per day; monthly	1982-2004
UMD_D1	Univ. of Maryland	2.5°	3 hourly; daily; monthly	1983-2007/06
NCEP	NOAA/NCEP-DOE Reanalysis	Global T62 grid	daily; monthly	1979-2010
ERA_Interim	ECMWF	1.5°	daily	1982-2011

Table 3.3 Evaluation of daily averaged surface parameters (downward SWR, upward SWR, net SWR, and surface albedo) from satellite estimates (UMD_MODIS, NASA/LaRC, AVHRR, and UMD_D1) and from NCEP reanalysis against ground measurements at ARM_NSA site for 2 years (2003-04).

	Data	**Mean obs.**	**Corr.**	**Std. (%)**	**Bias (%)**	**#cases**
SWR$^{\downarrow}$ (Wm^{-2})	MODIS	151	0.97	22.6 (15)	-3.6 (-2)	419
	NASA/LaRC	151	0.88	46.8 (31)	7.0 (5)	421
	AVHRR	151	0.84	51.0 (34)	9.5 (6)	422
	UMD_D1	152	0.89	42.2 (28)	10.9 (7)	421
	NCEP	152	0.87	51.4 (34)	51.8 (34)	419
SWR$^{\uparrow}$ (Wm^{-2})	MODIS	77	0.98	16.1 (21)	-5.2 (-7)	418
	NASA/LaRC	78	0.78	45.0 (58)	-14.6 (-19)	421
	AVHRR	77	0.81	42.7 (55)	-19.9 (-26)	422
	UMD_D1	78	0.88	35.2 (45)	4.9 (6)	420
	NCEP	78	0.76	63.9 (82)	44.3 (56)	419
Net SWR (Wm^{-2})	MODIS	72	0.97	16.0 (22)	2.5 (3)	419
	NASA/LaRC	69	0.92	25.0 (36)	24.7 (36)	413
	AVHRR	73	0.88	36.5 (50)	30.7 (42)	423
	UMD_D1	70	0.90	27.2 (39)	8.1 (12)	415
	NCEP	70	0.75	44.4 (63)	9.5 (13)	416
Surface Albedo	MODIS	0.5	0.98	0.07 (14)	-0.01 (-2)	416
	NASA/LaRC	0.5	0.76	0.20 (41)	-0.13 (-27)	422
	AVHRR	0.5	0.84	0.17 (35)	-0.12 (-24)	420
	UMD_D1	0.5	0.90	0.14 (29)	-0.0 (-0)	416
	NCEP	0.5	0.66	0.26 (53)	0.05 (10)	424

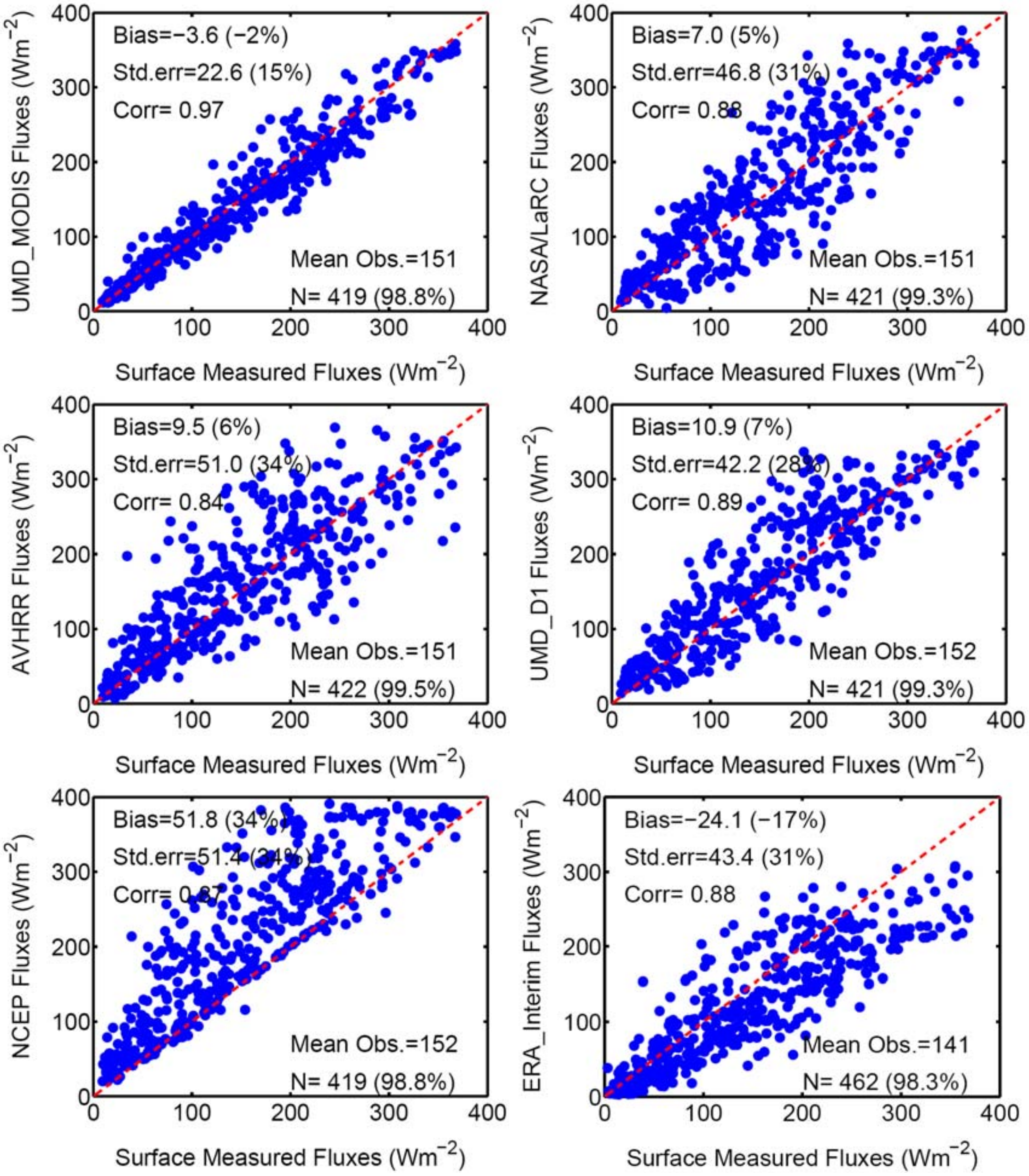

Figure 3.6 Evaluations of daily averaged surface downward SWR (Wm^{-2}) from satellite estimates (UMD_MODIS, NASA/LaRC, AVHRR, and UMD_D1) and from NCEP and ERA_Interim reanalysis against surface measurements at ARM_NSA site for 2 years (2003-04).

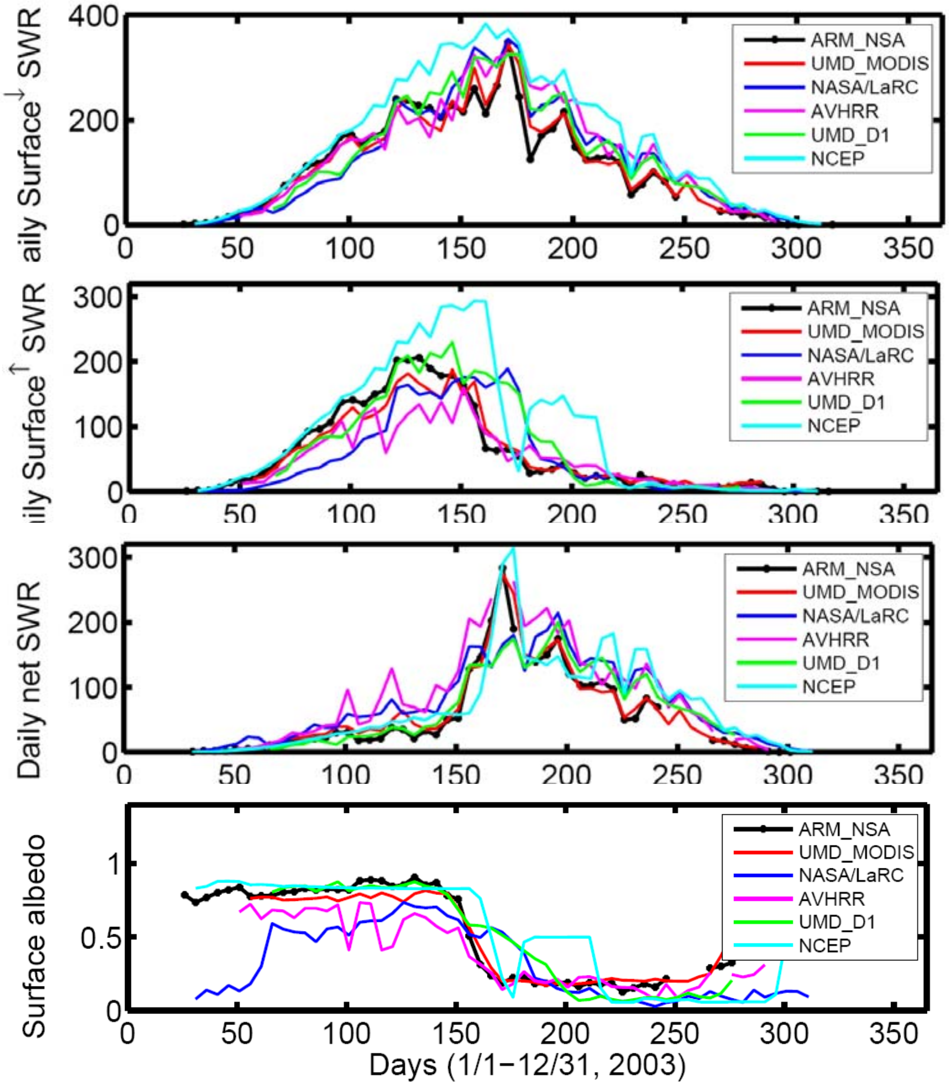

Figure 3.7 Time series of daily mean surface parameters (from Top to Bottom: SWR downward, upward, net, and surface albedo) derived from UMD_MODIS (red line), NASA/LaRC (blue line), AVHRR (magenta line), UMD_D1 (green line), and NCEP (cyan line) against surface observations (black line) at ARM_NSA site for period of January 1 to December 31 2003.

3.1.2 Evaluations against buoy measurements

Due to the lack of buoy observations at very high latitudes, observations “as far north as possible” were used. The following four buoys with observations on radiative fluxes were used:

1. KEO mooring site (http://www.pmel.noaa.gov/keo/index.html)

The NOAA Kuroshio Extension Observatory (KEO) moored buoy is located in the recirculation gyre south of the Kuroshio Extension at the nominal position of 144.6° E, 32.4° N. Data for the following periods will be used: Period 1: June 16, 2004 ~ Nov. 9, 2005; Period 2: May 27, 2006 ~ Apr. 16, 2007; Period 3: Sep. 26, 2007 ~ June 29, 2009 and Sep. 6 ~ 18, 2009.

2. JKEO mooring site (http://www.jamstec.go.jp/iorgc/ocorp/ktsfg/data/jkeo/).

The JAMSTEC Kuroshio Extension Observatory (JKEO) moored buoy is nominally located at 38° N, 146.5° E north of the Kuroshio Extension region (KEO). There are 4 phases of development for the buoys. For the phase 1, IORGC/JAMSTEC deployed a surface buoy (JKEO1) under collaboration with PMEL/NOAA.Data for the following periods will be used: Period 1: Feb. 18 ~ Sep. 15, 2007; Period 2: Oct. 5, 2007 ~ Jan. 25, 2008. For Phase 2, beginning Feb 29, 2008, IORGC/JAMSTEC replaced the PMEL-designed buoy with the K-TRITON developed by MARITEC/JAMSTEC. Data for the following periods will be used: Period 1: Feb. 29 ~ Sep. 4, 2008; Period 2: Nov. 12, 2008 ~ Aug. 27, 2009; Period 3: Aug. 29 ~ Dec. 31, 2009. The movement of the KEO and JKEO buoys is within the 1° footprint of the satellite data so no adjustments were made for the exact location.

3. CLIVAR Mode Water Dynamic Experiment (CLIMODE) buoys (http://uop.whoi.edu/projects/CLIMODE/climode.html). The CLIMODE buoy is located at 38° N, 65° W and the project aimed to study the dynamics of Eighteen Degree Water (EDW), the subtropical mode water of the North Atlantic. Data for the following periods will be used: Nov. 14, 2005 ~ Dec. 31, 2006.

4. PAPA mooring site (http://www.pmel.noaa.gov/stnP/index.html).

The Ocean Station Papa surface mooring was developed at the Pacific Marine Environmental Laboratory (PMEL) for the harsh conditions of the North Pacific region (http://www.pmel.noaa.gov/). The nominal position of this buoy was (50° N, 145° W). Data for the following periods will be used: Period 1: June 8, 2007 ~ Nov. 10, 2008; Period 2: June 15, 2009 ~ Dec. 31, 2009.

Evaluations of daily averaged surface downward SWR estimated from UMD_MODIS against surface observations at the KEO, JKEO, CLIMODE, and PAPA buoys are presented in *Figure 3.8*. Cases where estimates were outside the range of 3 stds were eliminated. The percentage of used observations is indicated in each figure. As evident, the bias is -2.4 Wm^{-2} (about 1.4% of mean value), 4.5 Wm^{-2} (3.2%), 7.3 Wm^{-2} (5.3%), and -6.8 Wm^{-2} (6.2%) for buoys of KEO, JKEO, CLIMODE, and PAPA, respectively. The RMSE values are 38.1, 29.6, 29.6, and 22.8 Wm^{-2} for the 4 buoys, which are about 21% of mean value. In *Figure 3.9* shown are the time series of daily averaged surface downward SWR estimated from UMD_MODIS and as observed at the KEO, JKEO, CLIMODE, and PAPA buoys. The variations of UMD_MODIS estimated fluxes fit well with the observations for the 4 buoys.

Tomita et al. (2010) conducted a comprehensive comparison of all the observed parameters from KEO and JKEO including radiative fluxes against the Japanese Ocean Flux data sets with use of Remote Sensing Observations (J-OFURO2). They found that the daily averaged downward SWR of J-OFUO2 for period of Jun. 2004 to Oct. 2006 (633 days) have small bias (0.3 Wm^{-2} for all days, -4.1 Wm^{-2} for winter, and 3.5 Wm^{-2} for summer) and have RMSE of 36.7 for all days, 21.4 for winter, and 43.3 Wm^{-2} for summer. *Kubota et al. (2008)* compared KEO observations against the National Centers for Environmental Prediction (NCEP)/National Center for Atmospheric Research (NCAR) reanalysis (NRA1), the NCEP/Department of Energy reanalysis (NRA2) data. They found that both re-analyses overestimated the daily averaged downward SWR with a bias of 17 Wm^{-2} for NRA1 and 4 Wm^{-2} for NRA2; RMSE of 52 for NRA1 and 41 Wm^{-2} for NRA2; and correlation of 0.8 for NRA1 and 0.88 for NRA2.

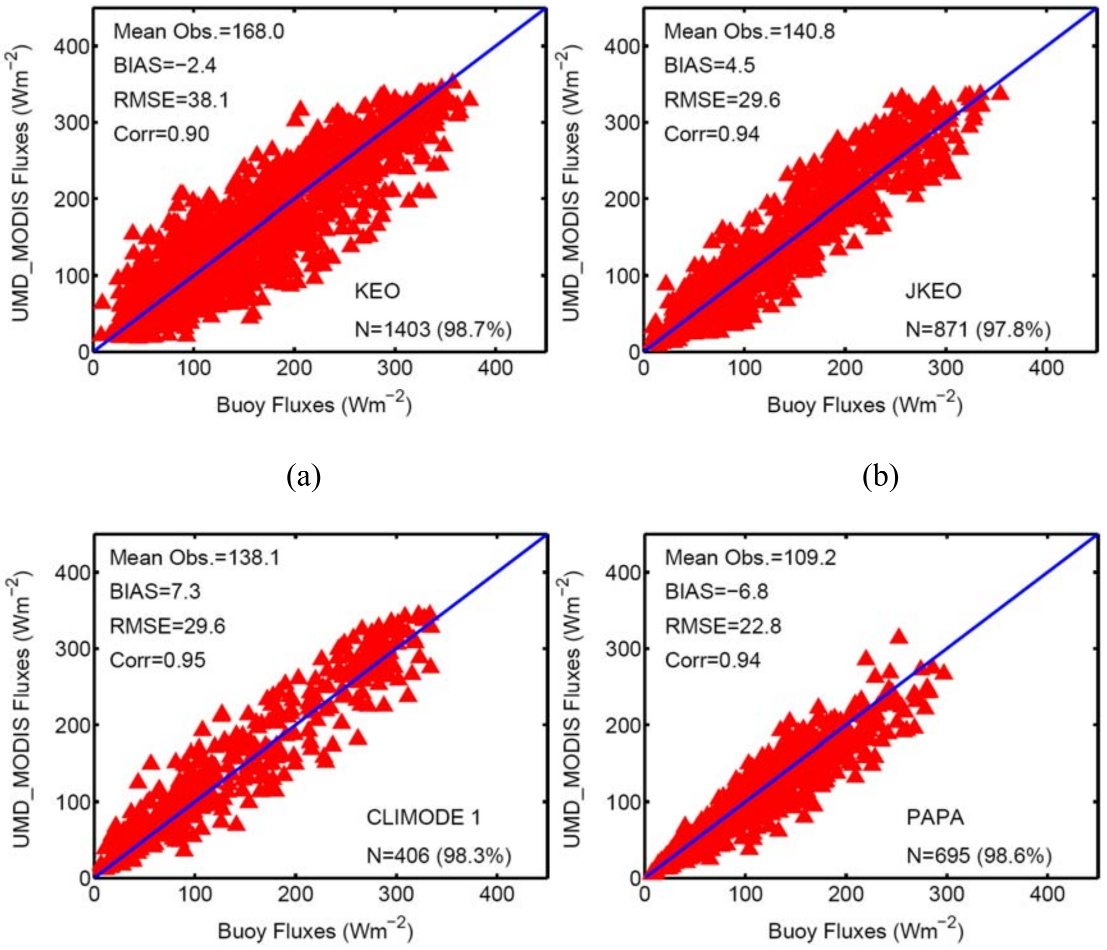

(a) (b)

(c) (d)

Figure 3.8 Evaluation of daily averaged surface downward SWR estimated from UMD_MODIS against buoy observations at (a): KEO (32° N, 145° E), (b): JKEO (38° N, 146.5° E), (c): CLIMODE (38° N, 65° W), and (d): PAPA (50° N, 145° W). Cases were eliminated when outside of 3 stds.

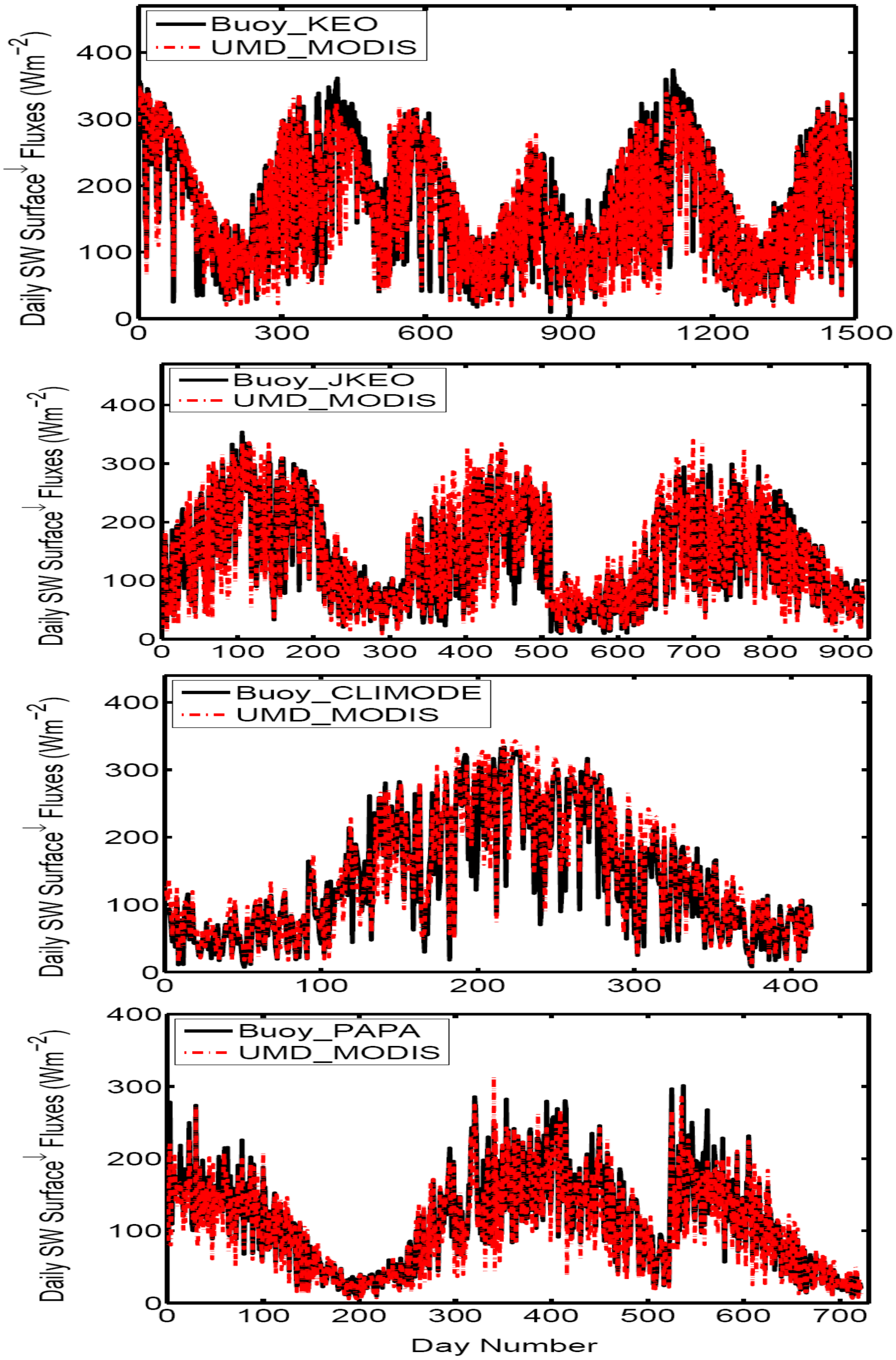

Figure 3.9 Time series of daily averaged surface downward SWR estimated from UMD_MODIS (red line) against buoy observations (black line) at KEO (32° N, 145° E), JKEO (38° N, 146.5° E), CLIMODE (38° N, 65° W), and PAPA (50° N, 145° W) from Top to Bottom.

3.2 Evaluations of UMD_MODIS (5-km) SWR estimates against ARM_NSA

The high resolution (5-km) surface SWR estimates from the UMD_MODIS model that accounts for the diurnal cycle were derived for the period of April – September 2007 over the Arctic Region (60° N-90° N). The procedure to compute the hourly and daily averaged SWR based on this product has been described in detail in the *Chapter 2*.

The evaluation of UMD_MODIS at 5-km resolution at hourly scale against ground measurements at the Barrow site for the period of March to September 2007 is shown in *Figure 3.10*. The results show a mean bias of 7.9 Wm^{-2} (3% of mean values), a standard deviation of error of 29.7 Wm^{-2} (17%), and a high correlation of 0.95. The evaluation at a daily scale shows a positive bias of 3.8 Wm^{-2} (2% of mean values), a standard deviation of error of 58.2 Wm^{-2} (23%), and a high correlation of 0.96. The SWR estimates at both hourly and daily scale overestimate the surface observations. The strong correlation (>=0.95) between MODIS based estimates and ground measurement is evident in *Figure 3.11*.

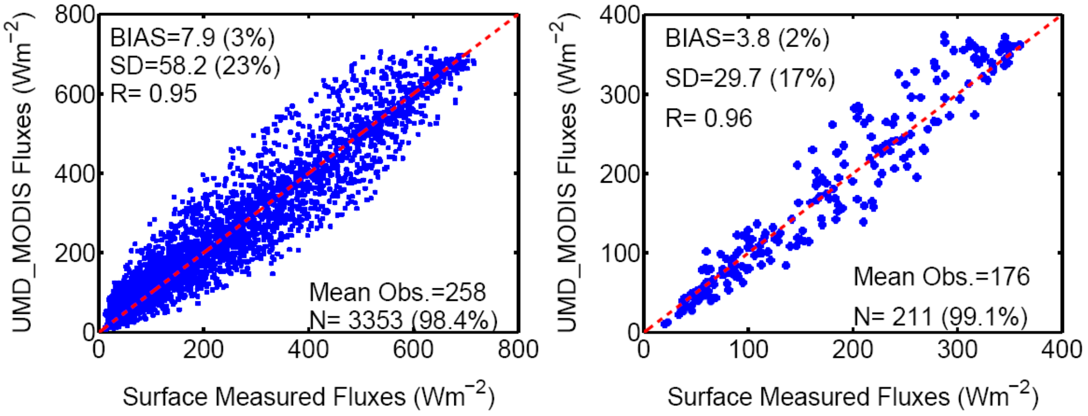

Figure 3.10 Evaluation of surface downward SWR estimated from UMD_MODIS (5-km) around Barrow site (71.32° N, 156.61° W) against ARM_NSA ground observations, for the period of March – September 2007. Cases were eliminated when outside of 3 stds.

(Left): at an hourly scale; (Right): at a daily scale.

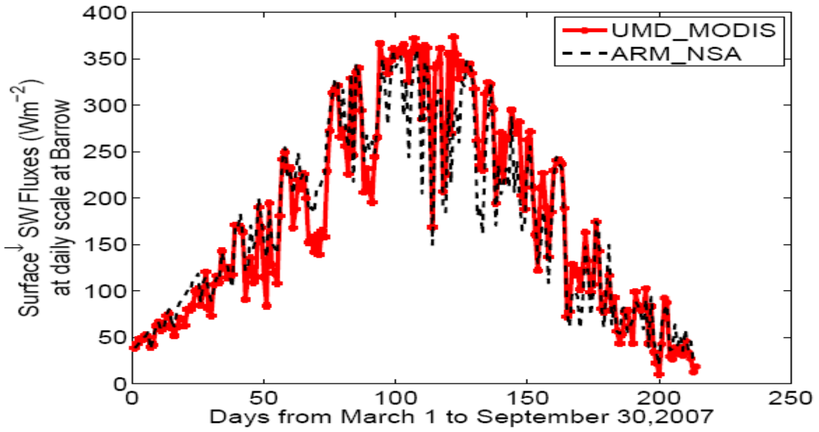

Figure 3.11 Time series of daily mean SWR estimated from UMD_MODIS (5-km; red line) around Barrow site and from ARM_NSA ground observations (black line), for the period of March to September 2007.

3.3 Evaluations of UMD_AVHRR and Extended AVHRR Polar Pathfinder (App-x) at ARM_NSA, Barrow, AK and BSRN sites

The UMD_AVHRR (30-km spatial resolution) and App-x products (25-km spatial resolution) are both based on AVHRR observations. These two products were first gridded to an equal-area grid map at 0.5° resolution. Evaluation results against surface observations at the ARM_NSA site at a daily time scale are shown in *Figure 3.12*. The UMD_AVHRR has a lower bias (-3% of the mean values) and smaller scatter (the stds are within 28% of the mean values) and has a higher correlation (0.9) than the App-x product (35% in stds; 0.83 in correlation).

The evaluations of monthly mean surface downward SWR estimates from UMD_AVHRR against surface observations from 32 BSRN sites for the period of 1992-2005 show good agreement with a bias (2.37 Wm^{-2}), standard deviation (18.6 Wm^{-2}), and high correlation (0.98) *(Figure 3.13).*

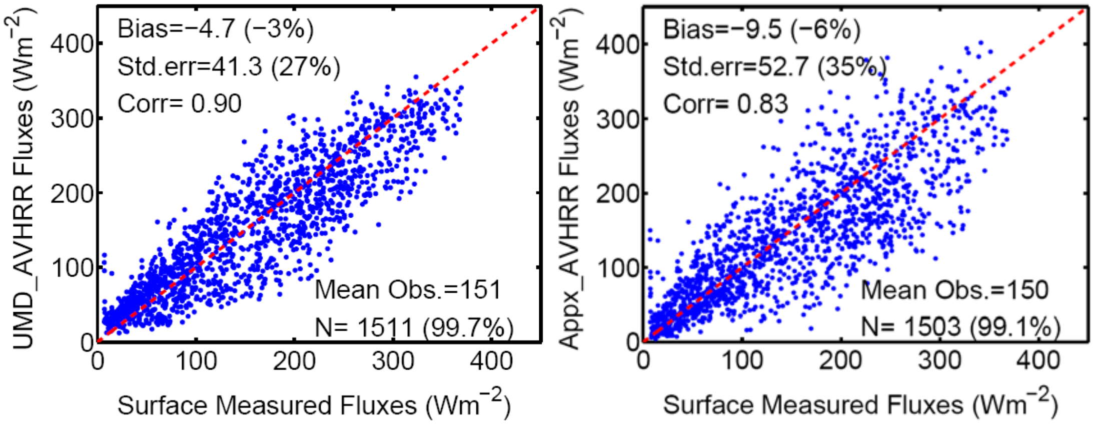

Figure 3.12 Evaluation of daily mean surface downward SWR estimated from UMD_AVHRR (left) and from App-x/AVHRR (right) against ARM_NSA ground observations at Barrow, for the period 1998-2004.

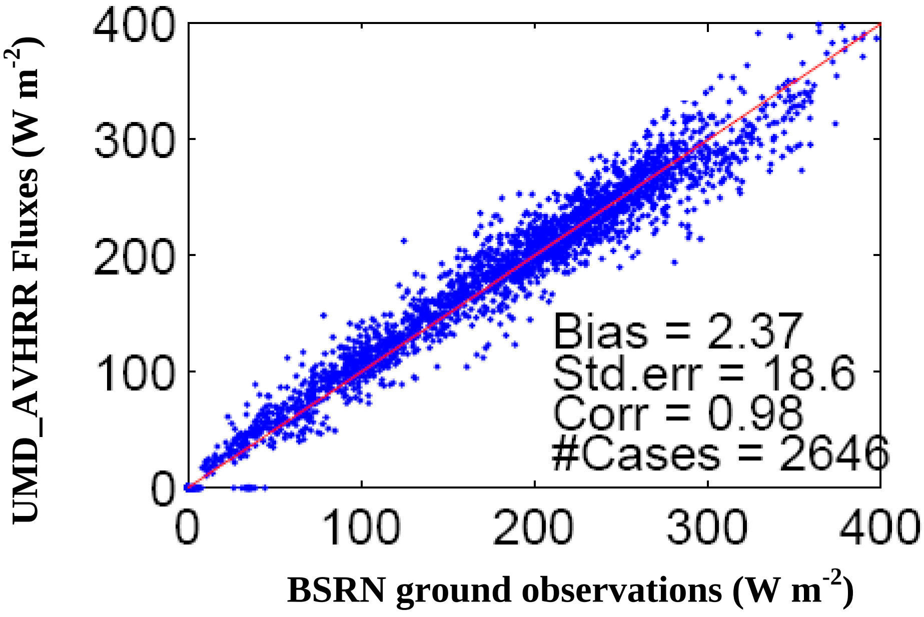

Figure 3.13 Evaluation of monthly mean surface downward SWR estimated from UMD_AVHRR against ground observations from 32 BSRN sites for the period 1992-2005 (courtesy of Y. Ma).

Chapter 4: Solar Heating of the Arctic Ocean in the Context of Ice-Albedo Feedback

The ice albedo feedback was proposed as a mechanism for polar amplification of warming in the Arctic *(Sellers, 1969; Hall, 2004).* Longwave cloud feedback *(Hall, 2004; Boe et al., 2009)* and energy transport from lower latitudes are also considered as factors for enhanced Arctic warming and sea ice loss in model simulations *(Holland and Bitz, 2003; Holland et al., 2006; Mahlstein and Knutti, 2011).* The discussion as to the mechanism that contributes most to the Arctic warming is still ongoing. A recent study by *Hwang et al. (2011)* has pointed out that model experiments show strong surface albedo and longwave cloud feedbacks in the 21st century climate simulations, but only weak increases in the energy transport from lower latitudes to the Arctic. It seems that local feedbacks are major contributors to the Arctic warming in recent decades. The updated Community Climate System model with improved sea ice physics and a new shortwave radiative transfer scheme has shown that aerosols and melting ice ponds influence the albedo and the corresponding feedback can play a role in 20th century Arctic sea ice reduction *(Holland, 2011).*

The ice-albedo feedback results from the large contrast between the surface albedo of sea ice (>0.6) and the open water (~0.07). Previous studies by *Perovich et al. (2007, 2008)* have utilized the SWR flux estimates from the ERA-40 Reanalysis and the operational European Center for Medium-Range Weather Forecast to calculate the solar heat input into the Arctic open water and discussed the effect of variations in solar heating in the context of ice-albedo feedback. Estimates of surface downward SWR derived from the UMD models (UMD_AVHRR; UMD_MODIS) based on satellite observations which have been comprehensively evaluated against surface observations *(Chapter 3)* are timely to improve estimates of solar heat input into the Arctic Ocean.

In this study such inputs have been estimated from improved satellite based estimates of SWR at both climatic (UMD_AVHRR model implemented at 0.5° resolution for 1984-2004) and at shorter time scales (UMD_MODIS model implemented at 1° resolution for 2003-2009). We have analyzed the trends and the relationship between the solar heat input into the Arctic Ocean and the open water fraction. Additionally, the extreme Arctic sea ice loss in 2007 has been investigated at higher spatial resolution using the SWR derived with the UMD_MODIS model as implemented at 5-km resolution.

4.1 Quantifying the ice-albedo feedback in the Arctic Ocean (0.5°)

According to the classic ice-albedo feedback mechanism, more open water leads to more solar heat absorption which results in more ice melt and more open water. The positive ice-albedo feedback can accelerate the reduction in the Arctic sea ice. In order to study the relationship of solar heat input into the Arctic open water and the variations of sea ice extent, the solar heat input was calculated from the improved satellite based SWR products developed in this study.

Previous investigations have shown that the increase in the summertime solar heat absorbed by the upper ocean water can trigger an ice-albedo feedback and is sufficient to accelerate the ice retreat, especially the ice bottom melting, and in the following year this can delay fall freeze-up by several weeks and reduce the winter ice growth *(Perovich et al. 2007, 2008).* Studies by *Perovich et al. (2007)* and *Steele et al. (2008)* have found that there was an increase of 150~200 MJ m^{-2}/year in solar energy absorbed at the ocean surface in 2007 in the northern Chukchi Sea. Assuming a complete transfer of heat to the sea ice, the decrease in winter ice growth is about:

$$\Delta h_{ice} = (150 \sim 200) MJm^{-2} / \rho_{ice} L_{ice} = 56 \sim 75 cm$$

Where ρ_{ice}=900 kg m^{-3} is sea ice density and L_{ice}=3×10^{5} J kg^{-1} is sea ice latent heat of fusion. The 56-75 cm smaller ice growth is a significant fraction of the ~2 m sea ice thickness in this part of the Arctic Ocean *(Zhang et al., 2000).*

If ocean-ice advection is small, the solar heating is simply lost to a gradually warming atmosphere before any ice forms, which implies a delay in fall freeze-up of

$$\Delta t = (150 \sim 200) MJm^{-2} / \rho_{air} cp_{air} ch_{aw} \Delta T_{aw} W_{10m} = 13 \sim 61 days$$

Where ρ_{air}=1.3 kg m^{-3} is air density, cp_{air}=10^{3} J kg^{-1}°C^{-1} is air heat capacity, ch_{aw}=10^{-3} is air-water heat exchange coefficient, ΔT_{aw}=5-10°C is air-water temperature difference and W_{10m}=5-10 m s^{-1} is the 10 m elevation wind speed.

The solar heating absorbed in the upper ocean is found to be the primary heat source for the extreme ice loss in year 2007 *(Perovich et al., 2008).* Observations of sea ice melting made from autonomous ice mass balance buoys have shown that there is an extraordinarily large amount of ice bottom melting in the Beaufort Sea in the summer of 2007 *(Figure 4.1).* The increase in the solar heating absorbed by the increasing open water can contribute to the bottom melting and ice retreat in 2007 *(Perovich et al., 2008).*

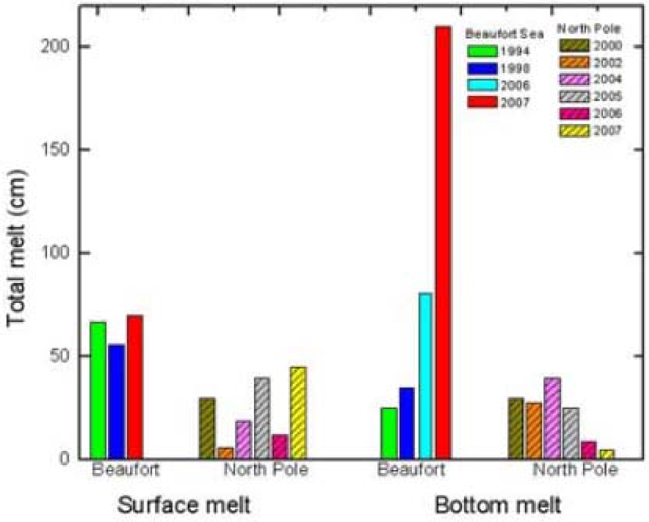

Figure 4.1 Observations of total surface and bottom melting in different years in the Beaufort Sea and North Pole regions *(Perovich et al., 2008).*

4.2 Methods to compute solar heat input into the Arctic Ocean

The solar heat input (surface net shortwave radiative fluxes) into the Arctic open water can be calculated as:

$$F(t) = F_s(t)(1-\alpha)(1-A) \tag{4.1}$$

Where F is the solar input into the ocean and adjacent seas, F_s is the surface downward solar irradiance, α is the albedo of open water (assumed as 0.07), and A is the ice or snow cover fraction.

Previous studies *(Perovich et al., 2007)* have investigated 27 years (1979-2005) of annual means and trends of the solar heat input into the Arctic Ocean by using daily solar irradiance from ERA-40 (1979-2001, 25-km), the operational European Center for Medium-Range Weather Forecasts products (2002-2005), and the ice concentration data from the satellite microwave observations using the NASA Team algorithm, as shown in *Figure 4.2*. The largest values of solar heating tend to occur in the seasonal ice zone, particularly in the Bering Sea, Davis Strait, and Greenland Sea, where ice retreat typically begins in late spring or early summer.

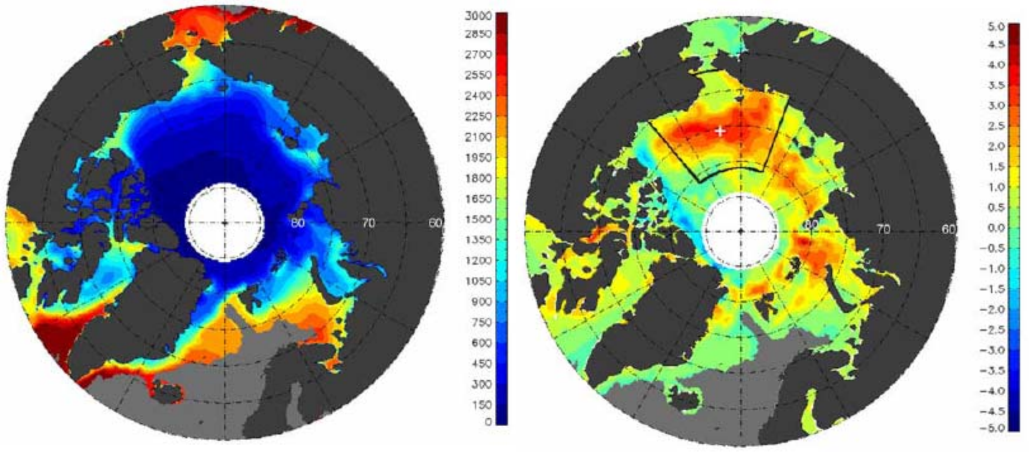

Figure 4.2 (Left) Mean total annual solar input to Arctic Ocean averaged over 1979-2005 (MJ m^{-2}/year); (Right) the linear trend of annual solar input to Arctic ocean (%/year) *(Perovich et al., 2007)*.

4.3 Solar heat input into the Arctic Ocean for 1984-2004 derived from AVHRR

We use the improved SWR estimates from UMD_AVHRR at a 0.5° equal-area resolution (about 50-km for each grid cell) during the period of 1984-2004 for the whole Arctic Ocean (60° N-90° N) where sea ice is present some time during the year, namely, it includes the perennial sea ice, annual sea ice, and relative low-latitude sea ice regions.

The area-averaged solar heat input is calculated as:

$$\overline{F} = \frac{\sum_i F_i S_i}{A} \tag{4.2}$$

Where $\overline{F}$ is the area-averaged solar input into the study region, F_i is the solar input into the ocean for each grid cell, S_i is the area of each grid cell, and A is the total area of the study region.

The sea ice fraction is calculated by using the daily and monthly mean sea ice concentration data from Nimbus-7 SMMR and DMSP SSM/I Passive Microwave Data generated with the NASA Team algorithm developed by the Oceans and Ice Branch, Laboratory for Hydrospheric Processes at NASA Goddard Space Flight Center (25-km) (from NSIDC: http://nsidc.org/data/nsidc-0051.html). The ice concentration data (25-km resolution) are gridded into 0.5° equal-area resolution.

The 21-year (1984-2004) averaged annual cumulative solar heat input into the Arctic Ocean is shown in *Figure 4.3 (left).* The highest values are along the seasonal ice zone at lower latitudes which can reach values of 1000-3000 MJ m^{-2}/year; lower values of a few hundred MJ m^{-2}/year can be found at higher latitudes where the perennial ice region is located. The distribution pattern is generally dependent on the latitudinal SWR associated with the ice location and concentration. The linear trends in the annual cumulative solar heating into the Arctic Ocean for 1984-2004 are illustrated in *Figure 4.3 (right).* Positive trends are found over much of the Arctic Ocean (~62% of all grid cells) and negative trends are for 38% of all grid cells. About 39% of all grid cells show modest magnitude of trends between -5%/year and 5%/year. The greatest increases (larger than 5% per year) in the solar heating trends are located in the seasonal ice zone, particularly near the East Siberian Sea (centered at 76° N, 150° E), Chukchi Sea (76° N, 165° W), and Beaufort Sea (76° N, 140° W), similar to previous studies *(Figure 4.2).*

The time series of open water fraction, annual cumulative solar heat input, and annual cumulative downwelling SWR from 1984 to 2004 are shown in *Figure 4.4* as percent anomalies (%). As *Eq. 4.1* shows, the solar heat input is a function of the

SWR and the sea ice concentration (open water fraction). There is almost no correlation (~0.1) between solar heat input and SWR for the 21 years. A negative linear trend in SWR (-0.5 Wm^{-2}/year) at a 99% confidence level (based on the t-test *(Wilks, 2006)*), which is similar to what was found in *Pinker et al. (2005),* who computed the first and second order trends in surface downward SWR averaged over the northern high latitude region (60° N-90° N) and reported a negative trend of -0.26 Wm^{-2}/year for period of 1983-2001. There is a correlation of (0.7) between the solar heat input and the open water fraction for 1984-2004 at a 75% confidence level as shown in *Figure 4.5*. The variation of the solar heat input follows closely with the variation of the open water fraction *(Figure 4.4).* The annual cumulative solar heat input into the Arctic Ocean shows a positive trend with a moderate magnitude of 0.15%/year, along with a positive trend (0.56%/year) for the open water fraction at a 99% confidence level.

Figure 4.6 shows a detailed insight into where the trends in the solar heat input have higher positive values for three selected regions: (1) a grid cell centered at (75.75° N, 134.75° E) at the East Siberian Sea; (2) a grid cell centered at (75.75° N, 179.75° W) at the Chukchi Sea; (3) a grid cell centered at (75.75° N, 139.75° W) at the Beaufort Sea. Results have shown that there is a strong correlation between the variation in solar heat input and the open water fraction (>=0.95) for the three regions. The linear trends for the anomalies in the solar heat input are 1.2%/year, 3.71%/year, and 2.53%/year for the East Siberian Sea, the Chukchi Sea, and the Beaufort Sea, respectively. These values are much higher than the area-averaged trend for the whole Arctic Ocean (0.15%/year). This indicates that the increased ice melting in such ice marginal areas leads to absorption of much more heat than in other regions due to the ice-albedo feedback, contributing to further ice melting. The linear trends for the anomalies in open water fraction are 1.26%/year, 2.83%/year, and 1.78%/year for the East Siberian Sea, the Chukchi Sea, and the Beaufort Sea, respectively, which are also larger than the area-averaged value (0.56%/year), indicating that the ice melting rate in the marginal area is also faster than at other locations in the Arctic Ocean. A similar conclusion for the Beaufort Sea has been reached from this study as shown in *Figure 4.6 (bottom)* compared to the study of *Perovich et al. (2007)* which used the ERA-40 data for the analysis.

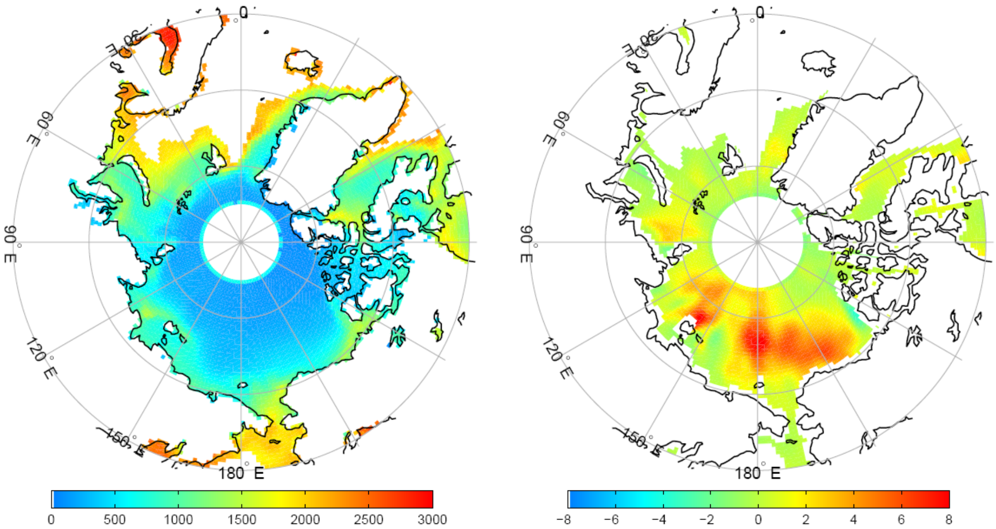

Figure 4.3 (Left）21-year (1984-2004) averaged total annual solar heat input to Arctic Ocean (MJ m^{-2}/year); (Right) linear trend (1984-2004) of annual solar input to Arctic ocean (%/year) calculated from UMD_AVHRR.

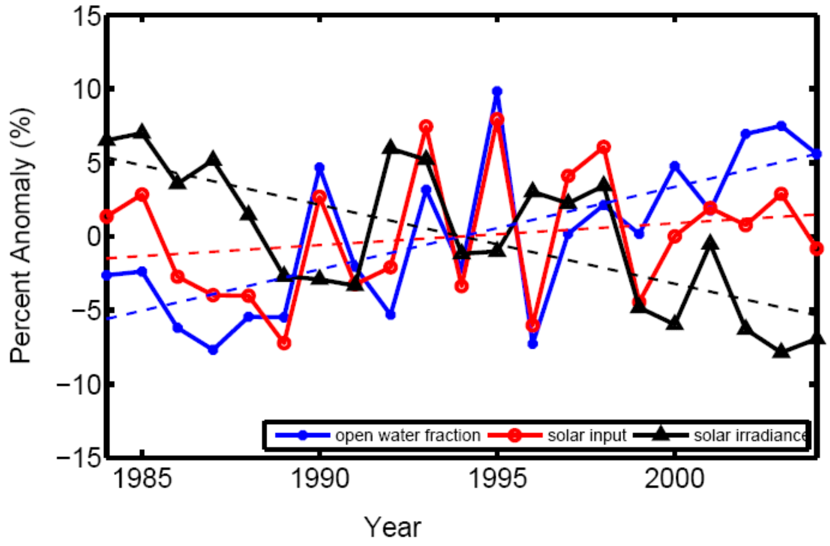

Figure 4.4 Anomaly (%) in open water fraction (blue solid line), annual solar heat input (red solid line), SWR (black solid line), and the corresponding linear trends (dash lines), for the whole Arctic Ocean (1984-2004).

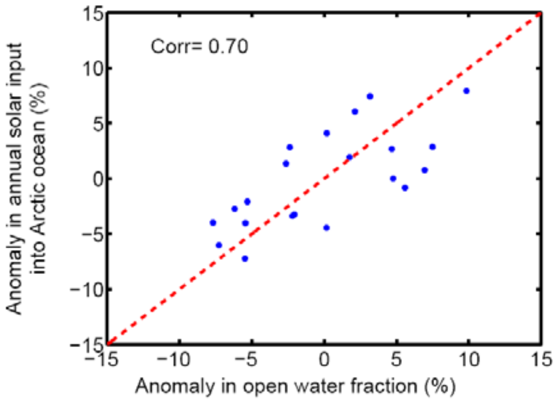

Figure 4.5 Correlation of anomaly in annual solar heat input and anomaly in open water fraction, based on the UMD_AVHRR SWR estimates (1984-2004) and the sea ice concentration data from Nimbus-7 SMMR and DMSP SSM/I Passive Microwave Data generated using the NASA Team algorithm from NSIDC (http://nsidc.org/data/nsidc-0051.html).

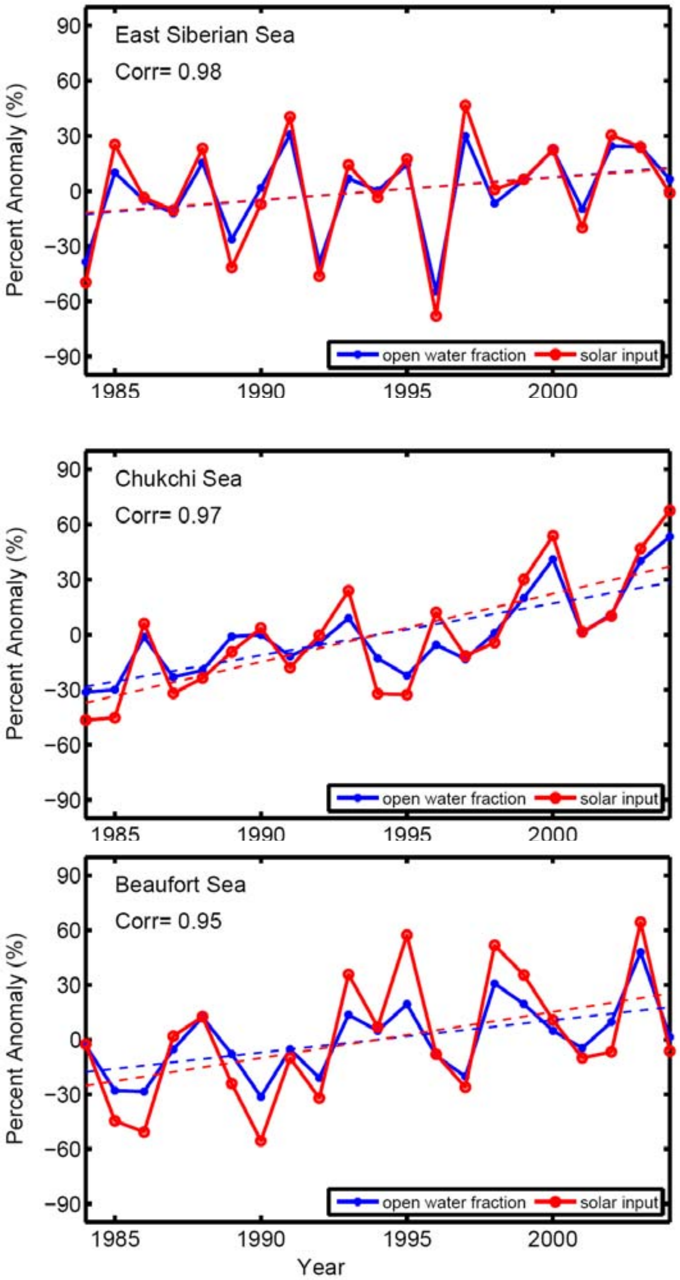

Figure 4.6 Anomaly in open water fraction (blue solid line), annual solar heat input (red solid line), and the corresponding linear trends (dash lines), for period of 1984-2004, for the regions centered at: (top) East Siberian Sea (75.75° N, 134.75° E); (middle) Chukchi Sea (75.75° N, 179.75° W); (bottom) Beaufort Sea (75.75° N, 139.75° W).

4.4 Solar heat input into the Arctic Ocean for 2003-2009 derived from MODIS (1°)

The evaluations of satellite and model based SWR estimates against ground measurements (land and ocean) have shown that the UMD_MODIS products provide the best estimates at high latitudes *(Chapter 3).* The other advantage of the UMD_MODIS product is that they are available from July 2002-June 2010 during which time the sea ice extent was at much lower levels than the climate mean values, especially for the recent years (2005 - 2009); it also includes the Arctic minimum sea ice record of September 2007 *(Figure 1.6).* It is meaningful to quantify the effect of the ice-albedo feedback on the Arctic ice loss in recent years using the high quality information. To be consistent with the resolution of UMD_MODIS (1°), the ice concentration data (25-km) were gridded into 1° resolution as shown in *Figure 4.7* as an example for monthly mean sea ice concentration for January 2003.

4.4.1 Solar heat input into the Arctic Ocean

The 7-year (2003-2009) averaged annual cumulative solar heat input to the Arctic Ocean is presented in *Figure 4.8 (left)*, showing a similar pattern but higher values as the one averaged over 21 years (1984-2004) *(Figure 4.3).* Namely, more solar energy has been absorbed by the Arctic open water in recent years, which may contribute to the acceleration of sea ice loss. The anomalies in the annual cumulative solar inputs into the Arctic Ocean for 2007 as compared with the mean values for 2003-2009 are illustrated in *Figure 4.8 (right).* The highest positive anomalies are located in the greatest 'melting area' as shown in *Figure 1.9*, including the East Siberian Sea, Chukchi Sea, and the Beaufort Sea.

For the period (2003-2009) the annual cumulative area-averaged solar heat input and solar irradiance are plotted in *Figure 4.9*. Although the solar energy absorbed by the Arctic Ocean in 2007 is at a maximum, the SWR reaching the ocean surface is about the average value for the other years. Following 2007, the annual cumulative solar heat input remains higher than average, associated with the lower ice cover in years 2008 and 2009. There is no significant correlation (0.1) between the solar heating into the Arctic Ocean and the SWR reaching the water surface. Therefore, the sea ice concentration is the dominant factor in determining the variation in solar heat input according to *Eq. 4.1*. This is evident from the way the solar heat input follows the variation of the open water fraction for the absolute value and the anomalies *(Figures 4.10 and Figure 4.11).* There is a strong correlation (0.99) between the two variables at a 75% confidence level; it is stronger than the correlation for period of 1984-2004 (0.7).

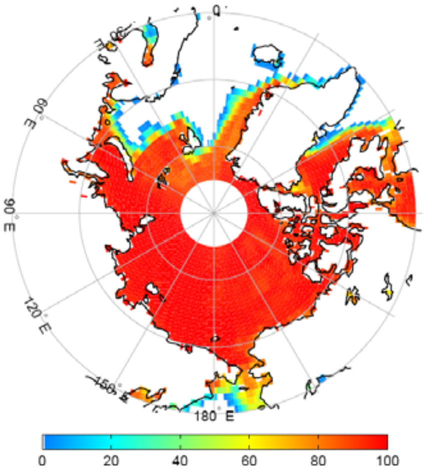

Figure 4.7 Monthly mean sea ice concentration (1°) for January 2003 based on the data from the NSIDC.

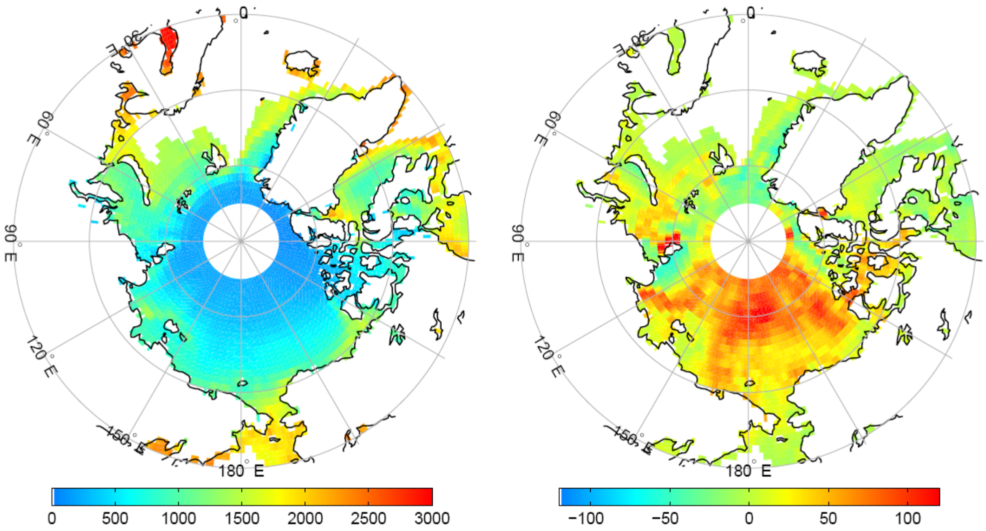

Figure 4.8 (Left) Mean total annual solar heat input into Arctic Ocean averaged over 2003-2009 (April– September) (in MJ m^{-2}/year); (Right) Percent anomaly in annual solar input into the Arctic Ocean for year 2007 as compared to 7-year (2003-2009) mean value. The largest increases occur in the greatest 'melting area'.

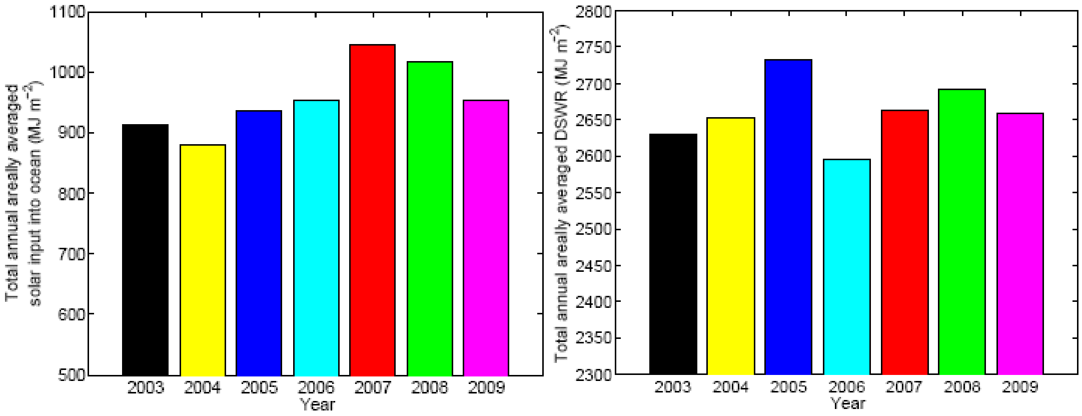

Figure 4.9 (Left) Annual cumulative area-averaged solar inputs (MJ m^{-2}/year); (Right) the surface solar incident irradiance (MJ m^{-2}/year) into the Arctic Ocean from April to September for period of 2003-2009. The area-averaged values are calculated by applying the area of each grid cell as a weight function and dividing by the total area.

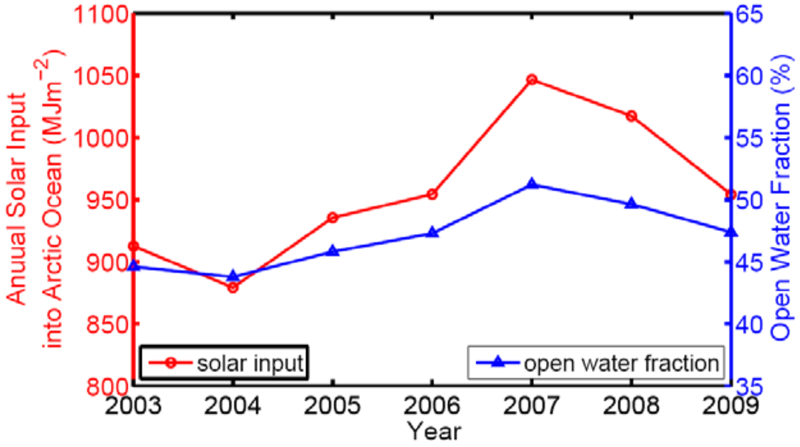

Figure 4.10 The time series of the total annual area-averaged solar input to Arctic Ocean and the annual mean open water fraction (%) for 2003-2009.

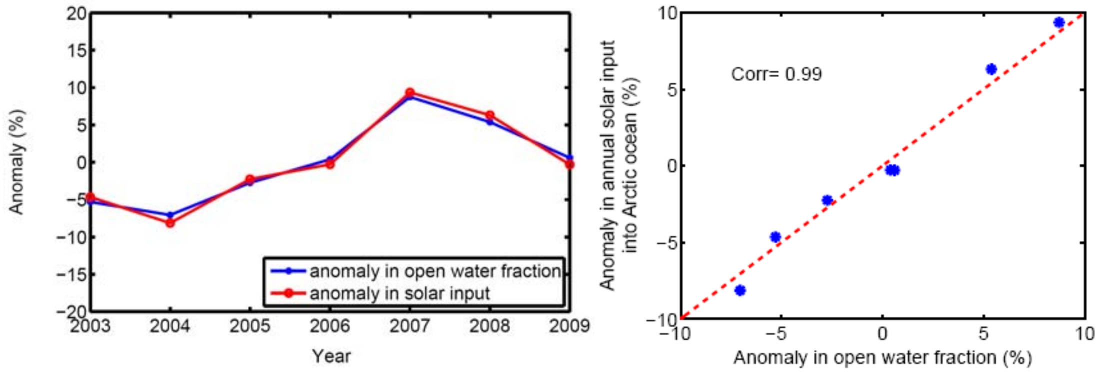

Figure 4.11 (Left) The time series of the percent anomalies for the annual cumulative solar heat input into the Arctic Ocean and for the annual mean open water fraction for 2003-2009; (Right) the correlation between the anomalies in the solar heat input and open water fraction.

4.4.2 Solar heat input into the Arctic ice-ocean system

The solar heat input to the ice-ocean system is the total solar energy absorbed by the open water and the sea ice together, which can be calculated as:

$$F(t) = F_s(t) - F_s(t)\overline{\alpha}(t) \tag{4.3}$$

Where, *F* is the solar input to ice-ocean system, *Fs* is the surface solar irradiance, and $\overline{\alpha}$ is the area-averaged albedo.

The area- averaged surface albedo is calculated as follows:

$$\overline{\alpha}(t) = \alpha_{ice}(t)A_{ice}(t) + \alpha_{ocean}A_{ocean}(t) \tag{4.4}$$

Where α_{ice} is the albedo of sea ice, α_{ocean} is the albedo of ocean (~0.07), A_{ice} is the ice cover fraction, and A_{ocean} is the open water fraction.

Based on previous studies *(Moody et al., 2005, 2007; Perovich et al., 2002; Arnold et al., 2002; Curry et al., 2000)*, the surface albedo over snow, sea ice, and open water is defined as follows:

(1) Snow covered ice surface: an albedo of 0.85 is assumed for the snow covered ice surface, therefore, the area-averaged albedo is:

$$\overline{\alpha_{snow}}(t) = \alpha_{snow}(t) A_{snow}(t)$$

(2) Sea ice: an albedo of 0.73 is assumed for sea ice, so the area-averaged albedo over sea ice is:

$$\overline{\alpha_{ice}}(t) = \alpha_{ice}(t) A_{ice}(t)$$

(3) Open water: an albedo of 0.07 is assumed for the open water surface, so the area-averaged albedo over open water is:

$$\overline{\alpha_{ocean}}(t) = \alpha_{ocean}(t) A_{ocean}(t)$$

The area averaged surface albedo is the sum of the albedos as defined above.

Based on the UMD_MODIS (1°) SWR estimates, the annual cumulative solar heat input to the Arctic ice-ocean system averaged from 2003 to 2009 is shown in *Figure 4.12 (left);* the maximum values are located along the coastline where the sea ice is much easier to melt. The solar input to the Arctic ice-ocean system for the 7 years is illustrated in *Figure 4.12 (right),* in which the value for 2007 is the maximum.

The variation of solar heating into the Arctic ice-ocean system is correlated to sea ice loss. The ice loss is defined in two ways: (1) Arctic sea ice extent loss during the entire melt season (March monthly mean minus September monthly mean) and (2) Arctic sea ice extent loss during the summer melt season (June monthly mean minus September monthly mean). The ice extent is defined as the area with a 15% or higher ice concentration. An example showing the time series of Arctic sea ice loss during the entire melt season and during the summer melt season from 1979 to 2008 is shown in *Figure 4.13* (*Kay and Gettelman, 2009*). For the period of 2003-09, the solar heat input into the Arctic ice-ocean system follows closely the track of the sea ice loss during the entire melt season with a correlation of 0.95; it also follows well the sea ice loss during the summer months with a correlation of 0.91 *(Figure 4.14).*

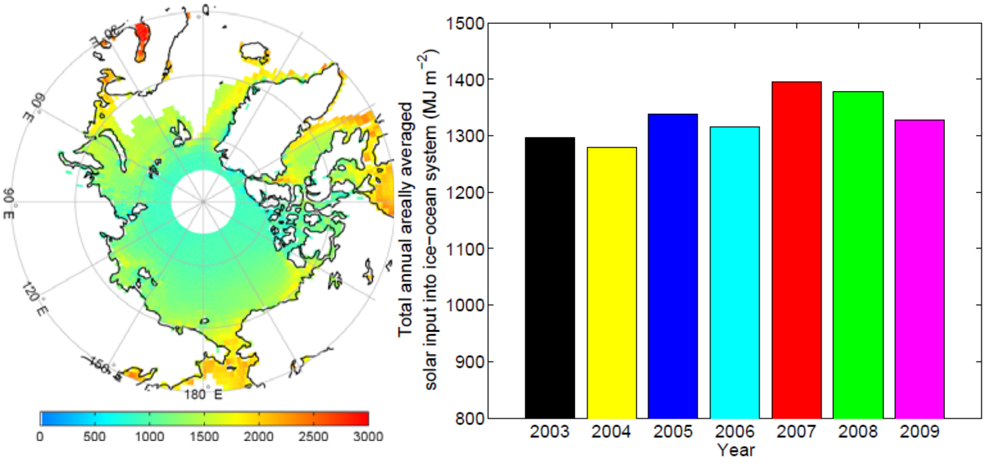

Figure 4.12 (Left) The 7-year (2003-09) averaged annual cumulative solar heat input into the Arctic ice-ocean system (60° N-90° N); (Right) Time series of the total annual solar heat input into the Arctic ice-ocean system 2003-2009 (MJ m^{-2}/year).

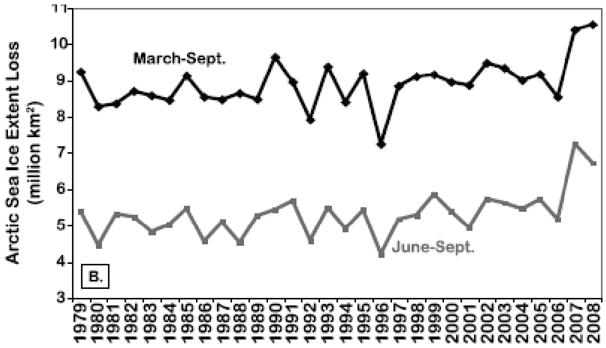

Figure 4.13 Time series of Arctic sea ice loss during the entire melt season and during the summer melt season (*Kay and Gettelman, 2009*).

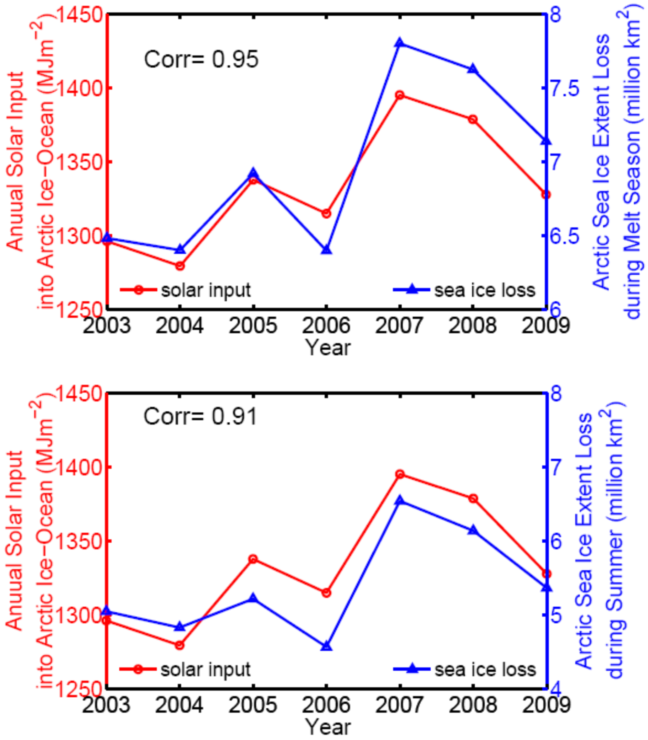

Figure 4.14 The correlation of the anomaly in the total annual solar heat input into Arctic ice-ocean system and Arctic sea ice extent loss during melt season (top) or during summer months (bottom).

4.5 Solar heat input into the Arctic Ocean for 1984-2009

There is an overlaps between UMD_MODIS and UMD_AVHRR products for the years 2003 and 2004. No discontinuities are detected in the time series of these two products for period of 1984-2009 and the detailed information for 2003-2004 (the overlap years) is shown in *Figure 4.15*. Therefore, it is possible to use the combined product for longer term trend analysis of solar heat input into the Arctic Ocean from 1984 to 2009, as shown in *Figure 4.16*. The black dash lines are the linear trends of the solar heat input into the ocean and the open water fraction for 1984-2009. Both have positive trends: 0.3%/year for solar heat input and 0.8% for open water fraction at a 99% confidence level. There is an obvious transition region separating the 26 years into two periods: (1) one with moderate change: 1984-2002; (2) one with an abrupt growth in both solar heat input and open water fraction: 2003-2009. This is consistent with the findings of *Stroeve et al. (2011)* stating that the period from 2002 onwards has a series of extreme September ice extent minima. The trends are also computed separately for the two periods, showing much higher values for the second period (2.0%/year for solar heat input and 1.9%/year for the open water fraction, at a 75% confidence level) than the first one (0.2%/year for solar heat input and 0.5%/year for the open water fraction, at a 99% confidence level).

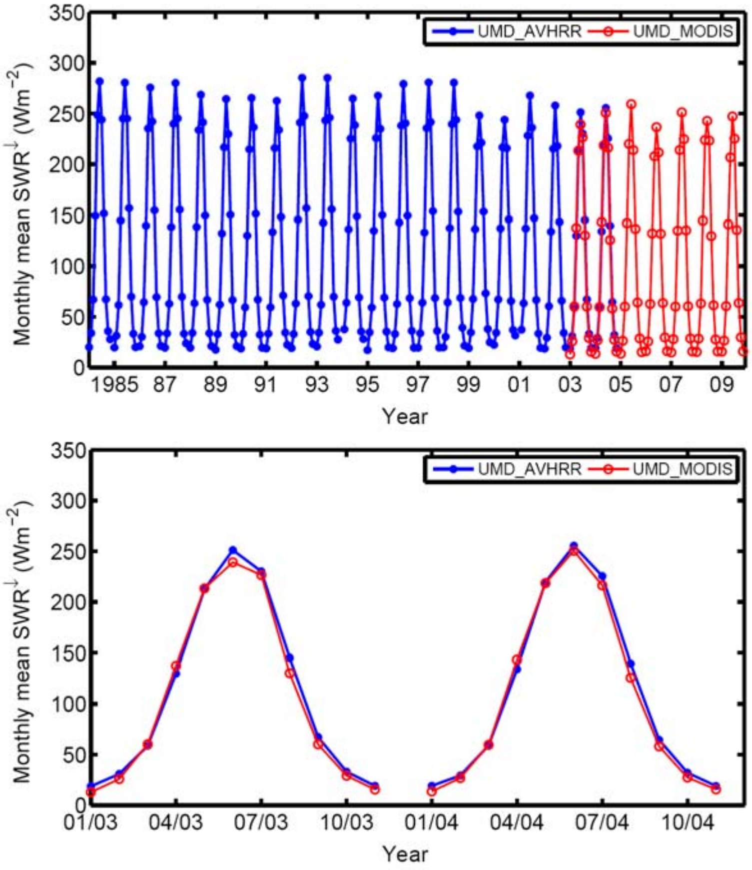

Figure 4.15 Monthly mean surface down SWR (Wm^{-2}) from UMD_AVHRR (blue line) and UMD_MODIS (red line) averaged over the Northern Polar Region (60° N - 90° N) for (top) 1984-2009 and (bottom) 2003-2004.

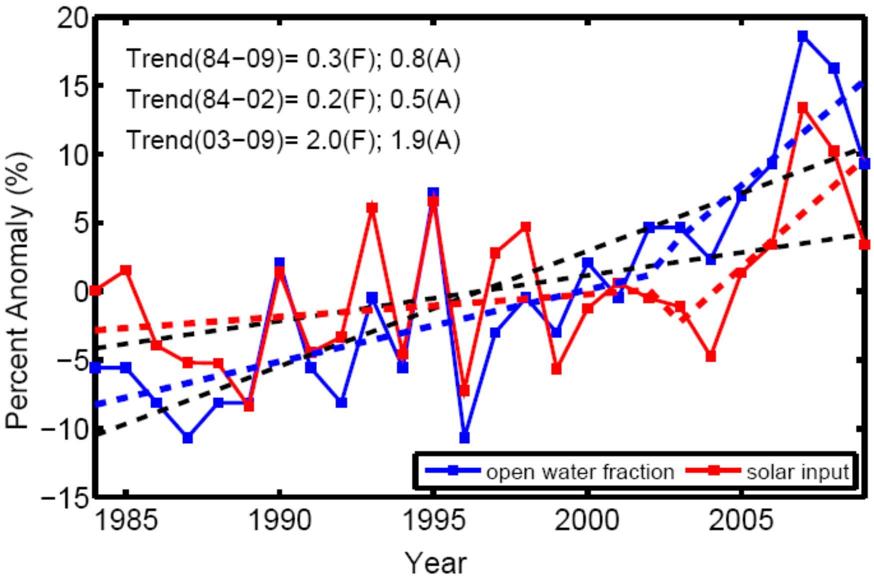

Figure 4.16 Anomaly in open water fraction (blue solid line) and annual solar heat input (red solid line), and the corresponding linear trends (dash lines):

(1) black dash lines: the trends for period of 1984-2009 (0.3%/year for solar input marked as 'F' and 0.8%/year for open water fraction marked as 'A' in the map);

(2) red dash lines: the trends (0.2%/year for 1984-2002 and 2.0%/year for 2003-2009) for the solar heat input ('F');

(3) blue dash lines: the trends (0.5%/year for 1984-2002 and 1.9%/year for 2003-2009) for the open water fraction ('A').

The correlation is 0.81 for the whole period of 1984-2009.

4.6 Extreme sea ice loss in 2007 from MODIS, 5-km

One year of high resolution product (5-km) was generated with the UMD_MODIS model for the spring and summer months (March – September) of 2007; evaluation of this product is presented in *Chapter 3*. Such data can be utilized to improve heat input estimates into the sea marginal areas, where the 0.5° or 1°

resolution data may mask the smaller scale variability in surface conditions. The MODIS 5-km data are gridded into 0.25° equal-area grids (equal to 25-km) for the computation of solar heat input into the Arctic Ocean in order to keep consistent with the sea ice concentration products from NSIDC provided at 25-km resolution.

4.6.1 Differences in solar heat input due to spatial resolution (UMD_MODIS)

It is expected that there is a difference in the calculated solar heat input into the ocean for grid cells with large melting of sea ice if calculated at different spatial resolutions (UMD_MODIS 1° and 5-km). Such regions are located along the seasonal sea ice zone as marked by black circles *(Figure 4.17).* The grid cells within one of the circles (75° N-76° N; 120° E-135° E) were selected to study the differences due to spatial resolutions. The MODIS 5-km data were aggregated into 25-km equal-area units to be consistent with the ice concentration. The distribution of monthly mean ice concentration and monthly cumulative solar heat input for May 2007 from these two spatial resolutions data (1° and 25-km) are demonstrated in *Figures 4.18 and 4.19*. One grid cell in this region centered (75.5° N, 122.5° E) was selected for detailed investigation, which includes four grid cells at 25-km resolution centered (75.875° N, 122.5° E), (75.625° N, 122.5° E), (75.375° N, 122.5° E), and (75.125° N, 122.5° E). At the latitude of 75.5° N, the length of one grid (1°) is 110-km in latitude and 25-km in longitude and one grid (25-km) is 25-km in latitude and longitude (there are four grid cells within one 1° grid cell) as shown in *Figure 4.18.* The daily solar heat input computed from the 1° grid cell and the corresponding four high resolution grid cells for May 2007 is illustrated in *Figure 4.20*. The black line represents the time series of the solar heating computed from 1° grid cell, and the color lines (except the red one) represent the results from four high resolution grid cells showing that the maximum difference can reach up to 10 MJ m^{-2}/day. The averaged values from the four high resolution grid cells are shown as a red line. The difference in the monthly mean ice concentration and monthly cumulative solar heat input for May 2007 from the two different spatial resolution grid cells are summarized in *Table 4.1* and *Table 4.2*. From the 1° grid cell, the ice concentration is 64.4%, but from the four high resolution grid cells, the values of the ice concentration are 86.6%, 78.1%, 58.1%, and 36.8%, respectively. For the 1° grid cell, the monthly cumulative solar heat input is 164.9 MJ m^{-2}/month and for the four corresponding high resolution grid cells, the solar heat input is 58.0, 93.0, 189.3 and 296.4 MJ m^{-2}/month, respectively. Similar to the situation with ice concentration, the lower resolution data do not fully represent the higher resolution information within the grid cell. The high-resolution UMD_MODIS SWR estimates provide an opportunity to look into details along the seasonal ice zone.

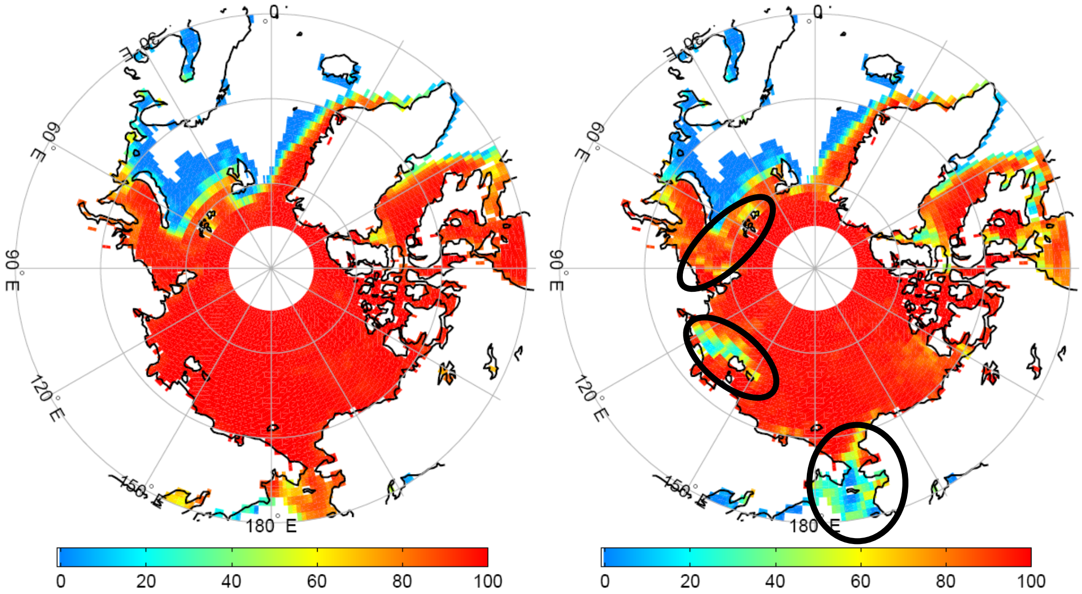

Figure 4.17 The monthly mean sea ice concentration (25-km) for January 2007 (Left) and for May 2007 (Right) (the black circles show the region with large melting).

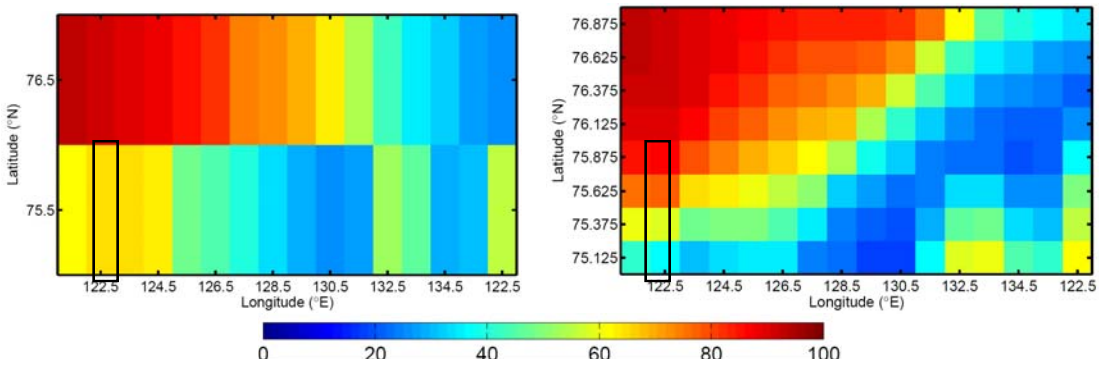

Figure 4.18 Monthly mean sea ice concentration for May 2007 for the region (75° N-76° N; 120° E-135° E) from the NSIDC products gridded into: (left) one grid cell at 1° resolution represents ~110-km in latitude × ~25-km in longitude, and (right) one grid cell represents ~25-km in latitude and longitude.

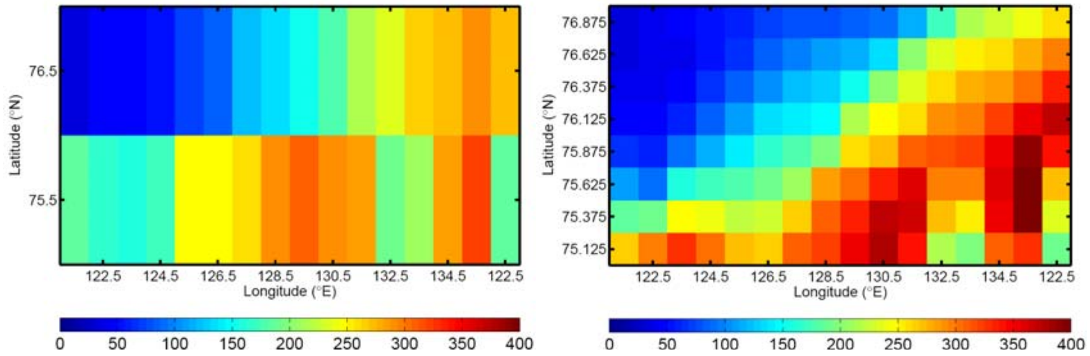

Figure 4.19 The monthly cumulative solar heat input into ocean calculated from two spatial resolution (1°; 25-km) data for the region (75° N-76° N; 120° E-135° E) for May 2007 (MJ m^{-2}/month).

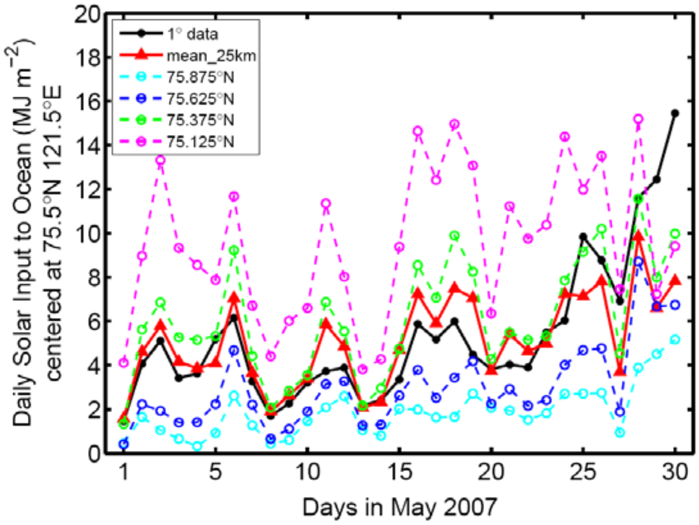

Figure 4.20 The black solid line is the daily solar heat input into a grid cell centered at (75.5° N, 122.5° E) for May 2007 (MJ m^{-2}/day) calculated from 1° product; the colored (cyan, blue, green, and magenta) dashed lines are the inputs from each grid of 25-km and the red line is the solar input averaged from four grids from the 25-km product.

Table 4.1 Monthly mean ice concentration (%) for grid cells at 1° and 25-km for May 2007.

Grid resolution	Grid position	Monthly mean ice concentration (%)
1°	centered at 75.5°N	64.4
25-km	centered at 75.875 °N	86.6
	centered at 75.625 °N	78.1
	centered at 75.375 °N	58.1
	centered at 75.125 °N	36.8

Table 4.2 Monthly cumulative solar heat input (MJ m^{-2}/month) for the grid cells at 1° and 25-km for May 2007.

Grid resolution	Grid position	Solar heating into ocean (MJ m^{-2}/month)
1°	centered at 75.5°N	164.9
25-km	centered at 75.875 °N	58.0
	centered at 75.625 °N	93.0
	centered at 75.375 °N	189.3
	centered at 75.125 °N	296.4

4.6.2 Solar heat input into the Arctic Ocean in 2007

The additional solar energy absorbed in the upper ocean during the summertime due to the increase in open water can accelerate the adjacent sea ice melting *(Perovich et al., 2008)* and is sufficient to reduce the following winter's ice growth by as much as several cm and delay a fall freeze-up from two weeks to two months as described in *the Section 4.1* (*Steele et al., 2008*). Temperature anomalies in 2007 are much higher than in any other year and the sea ice extent reached a historical minimum in the Arctic. The sea ice extent in the years of 2008-2010 still remains low as described in *Chapter 1.*

Calculations of the monthly cumulative solar heating for the summer months (June, July, and August) for 2007 and the mean values averaged from 1984 to 2004 are illustrated in *Figure 4.21* and *Figure 4.22*. The distribution for 2007 is shown in the left column of *Figure 4.21* for June, July, and August from top to bottom; the right column shows the corresponding values from the 21-year mean. For each summer month, the absolute values of the solar heat input into Arctic Ocean from 2007 are much higher than the mean values, which can be seen from *Figure 4.22 (left)* given as the percent anomaly in 2007 for each month. The anomalies can reach more than 300% compared to the 21-year mean values. The maximum anomalies are located at the same location as the open water fraction anomalies with maximum increase in area as shown in *Figure 4.22 (right).* The locations of the maximum values also correspond to similar places where the surface temperature anomaly is higher than the mean values (*Steele et al., 2008). Stroeve et al. (2011)* used similar techniques to estimate the anomalies in absorbed shortwave radiation over the Arctic

Ocean for 2005-2010 based on monthly means from the Japan Meteorological Agency reanalysis (JRA-25) interpolated to a 100-km equal area grid. It was pointed out that the positive anomalies grow in both magnitude and extent through the melt season (May-August) which is also strongly evident in the Beaufort, Chukchi, and East Siberian Seas. A model study (*Zhang et al, 2008)* also pointed to the wind and the ice-albedo feedback anomalies as the main responsible factors for the retreat of sea ice in 2007.

The anomalies in the annual cumulative solar heating of the Arctic Ocean in 2007 as compared with the 21-year mean values (1984-2004) are shown in *Figure 4.23*. *Perovich et al. (2008)* reported similar patterns for the year 2007 with greatest positive anomalies at the Beaufort Sea as compared to the 27-year mean (1979-2005) *(Figure 4.24)*.

The solar heat input into the Arctic Ocean based on the UMD_MODIS 5-km SWR provides information how much solar energy into the ocean can contribute to accelerate the sea ice loss in 2007. Solar radiation absorbed in the upper open water can provide more than adequate heat for the ice bottom melting and sea ice retreat in 2007. An abrupt increase in the open water fraction resulted in maximum anomalies in solar heating to the upper ocean of over 300%, triggering an ice-albedo feedback and contributing to further melting the sea ice. Such positive ice-albedo feedback can accelerate the reduction in Arctic sea ice and delay the re-formation of winter ice along the seasonal ice zone.

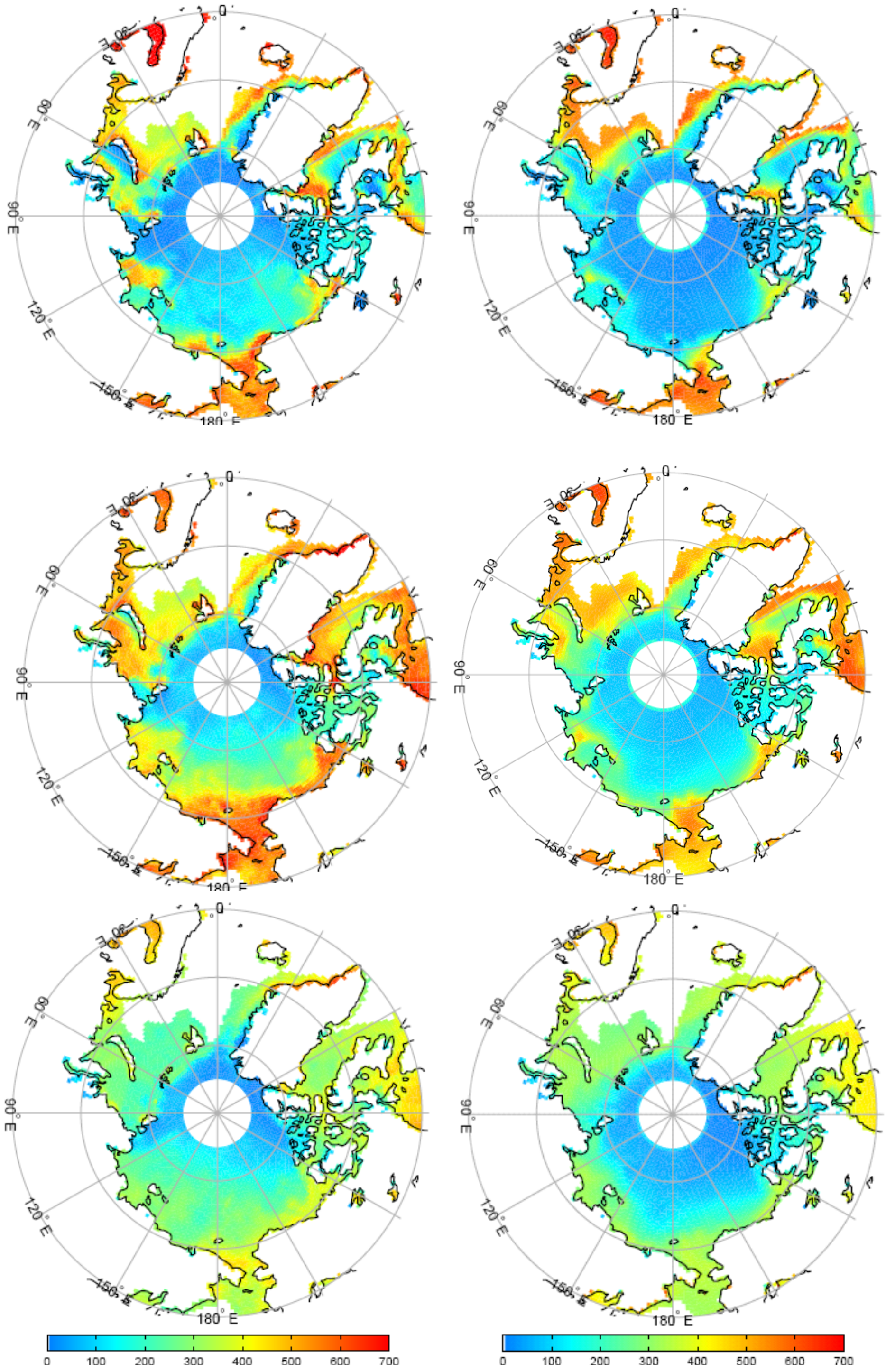

Figure 4.21 Monthly cumulative solar heat input (MJ m^{-2}/month) for: (left) 2007; (right) 1984-2004 mean (Top (June); Middle (July); Bottom (August)).

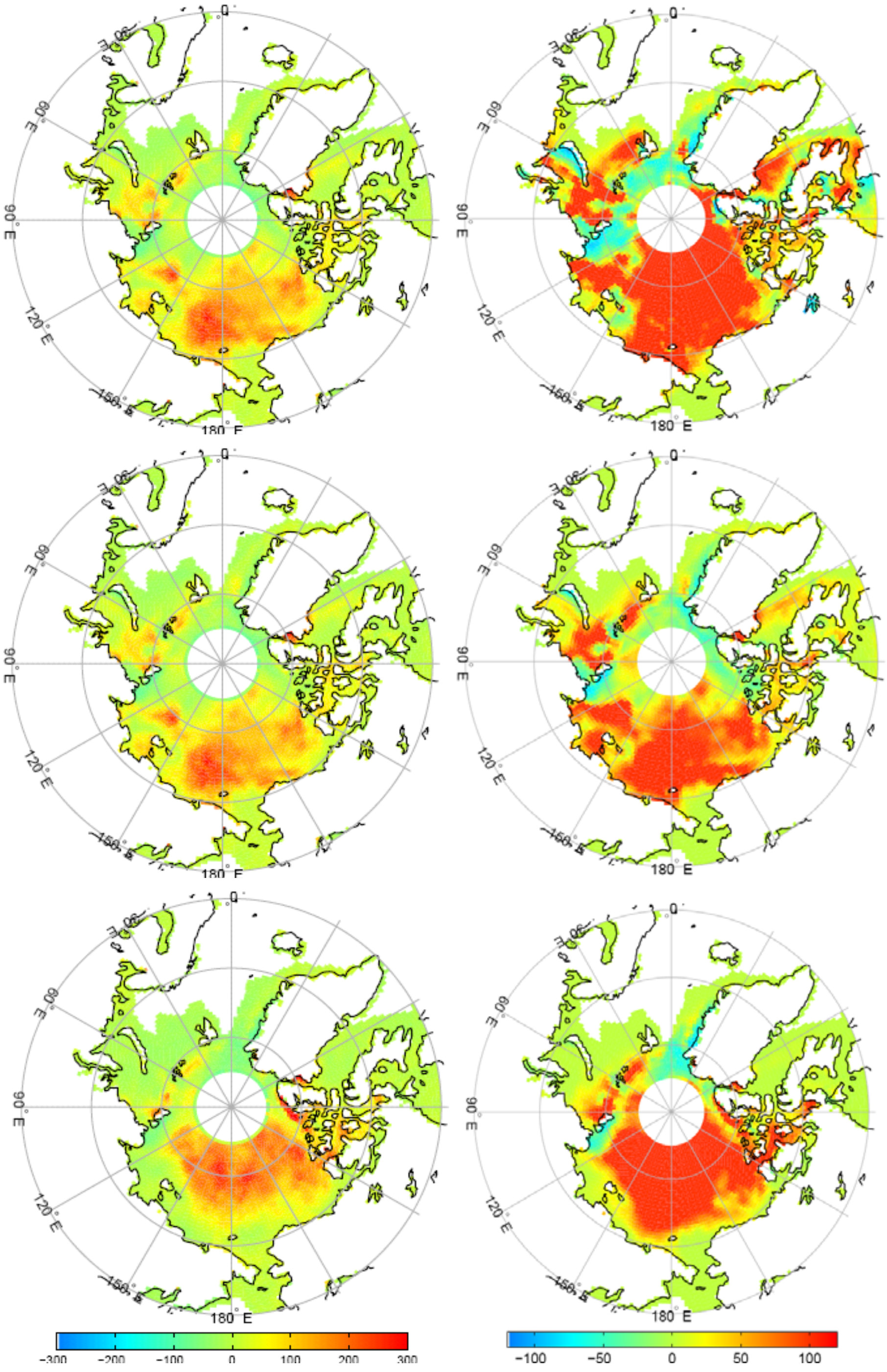

Figure 4.22 Percent anomaly (%) of year 2007 compared to 1984-2004 mean in: (left) monthly cumulative solar heat input; (right) in open water fraction (Top (June); Middle (July); Bottom (August)).

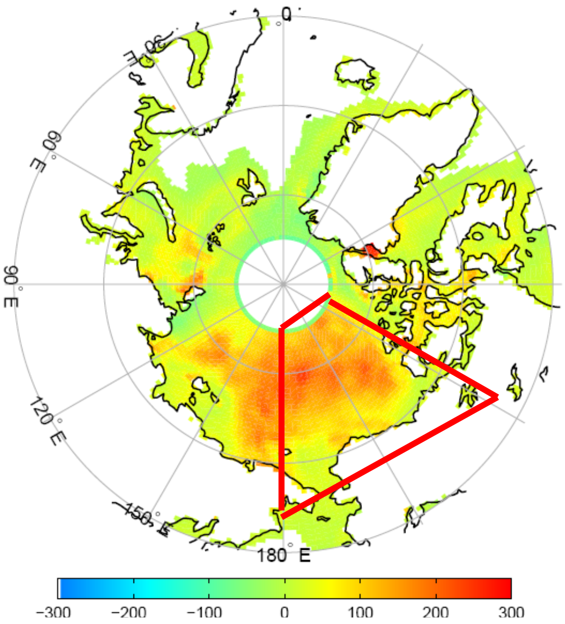

Figure 4.23 Percent anomaly (%) in annual cumulative solar heat input into the Arctic Ocean for 2007 compared with the 21-year (1984-2004) mean values. The region within read lines is the same region as shown in *Figure 4.24*.

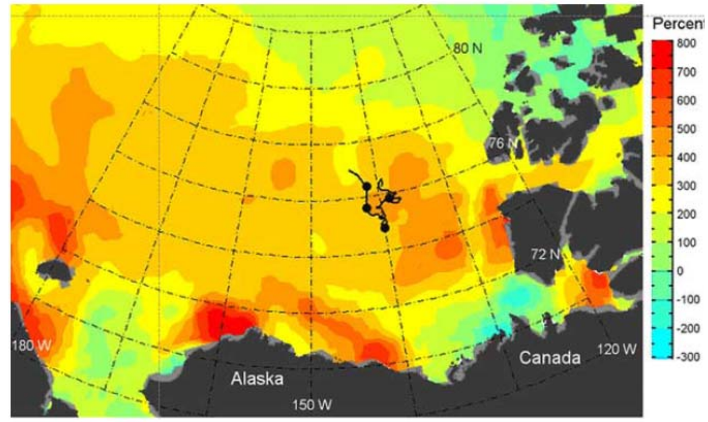

Figure 4.24 Anomaly of 2007 total (1 January through 21 September) cumulative solar heat input directly into the ocean compared to the average from 1979 to 2005 *(Perovich et al., 2008)*.

4.6.3 Solar heating contributing to the bottom melting at the Beaufort Sea in 2007

Studies by *Perovich et al. (2008)* have shown that the 2.1 m of sea ice bottom melt in 2007 in the Beaufort Sea is more than six times the annual average value of 0.34 m for the 1990s and 2.5 times the 2006 value, which is a major contributor to the 2007 extreme sea ice loss in this area. The rapid bottom melting starts in early June and reaches an average of 4 cm/day in August and the maximum of 11 cm/day during the last week of August 2007 *(Figure 2) (Perovich et al., 2008)*. Previous studies have stressed the importance of solar heat input to the upper ocean surface on the ice bottom melting *(Maykut and Mcphee, 1995; Perovich et al., 2005 and 2008)*. The ice cover thinned by excessive bottom melting can transmit more solar heat to the ocean than the thicker sea ice cover, which helps to absorb more solar energy in the ocean and cause more ice melting, triggering the ice-albedo feedback mechanism. For the Beaufort Sea, the increase in the solar heat input into the Arctic Ocean in 2007 as a result of sea ice melting is sufficient in magnitude and in timing to accelerate the bottom melting of the sea ice as shown in *Figure 4.25,* in which the dashed line represents the heat required for the bottom ice melting *(Perovich et al., 2008)*. In this study, a similar computation has been performed for the Beaufort Sea based on the high resolution MODIS products (5-km). The solar heat input into the grid cell centered at (75° N, -140° W) at the Beaufort Sea for year 2007 and for the average from 1984-2004 are presented in *Figure 4.26*. There is twice as much solar heating absorbed in the ocean in 2007 than the required heating for bottom melting and the 21-year mean. It should be noted that regions like the Beaufort Sea along the seasonal ice zone at lower latitudes are the lower bound on the solar energy absorbed in the

Arctic Ocean. This can contribute to the sea ice becoming thinner and accelerate the ice-albedo feedback at the Arctic Ocean.

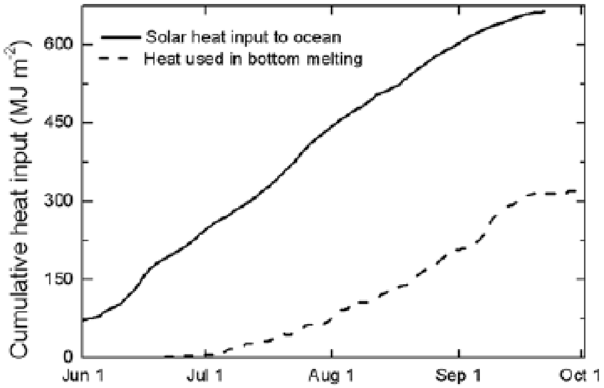

Figure 4.25 Time series of the heat required for the bottom melting around Beaufort Sea (dash line), and the daily cumulative solar heat input to the ocean in 2007 based on the European Center for Medium Range Weather Forecast products *(Perovich et al., 2008).*

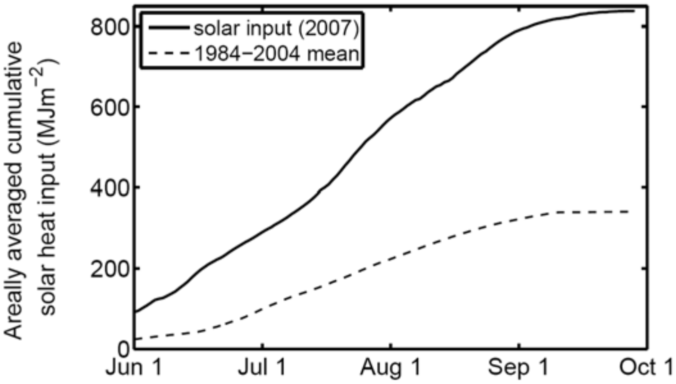

Figure 4.26 The daily cumulative solar heat input directly to the ocean centered at (75° N, -140° W, located within the Beaufort Sea) in 2007 (solid line) and the mean values for period of 1984-2004 (dash line).

4.6.4 Lead-lag correlation between open water fraction and solar heating in 2007

The area-averaged solar heat input to the Arctic Ocean associated with the open water fraction for 2007 and for the 21-year mean (1984-2004) are shown in *Figure 4.27*. The areas of open water in 2007 can absorb more solar energy in 2007 as compared with the 21-year mean and contribute to further sea ice loss. There is a correlation of (0.99) between the solar heating and the open water fraction. There may be a lead or lag in time for the variations of open water and solar heating into the ocean. The lead-lag-correlation (based on *(Wilks, 2006)*) has been studied for the anomalies in 2007 compared with the 21-year (1984-2004) mean as shown in *Figure 4.28*. The lead or lag days represent days when open water fraction varies ahead of or behind the solar heating. The correlation reaches a maximum in the 16th leading day and the values decrease on both sides around this day. The ice melting about half month ahead of the solar heating contributes to the absorption of solar energy into the ocean and further ice retreat in 2007.

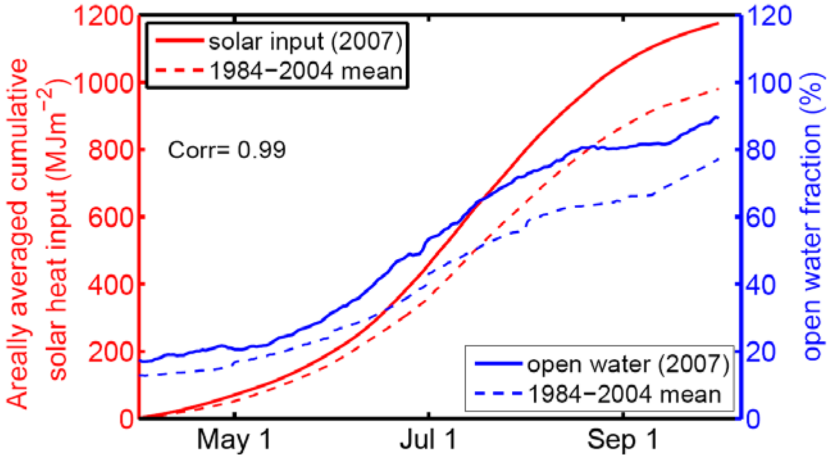

Figure 4.27 Time series of the area-averaged daily cumulative solar heating to the Arctic Ocean (red solid line) and open water fraction (blue solid line) in 2007 and the corresponding values for 1984-2004 (dash lines).

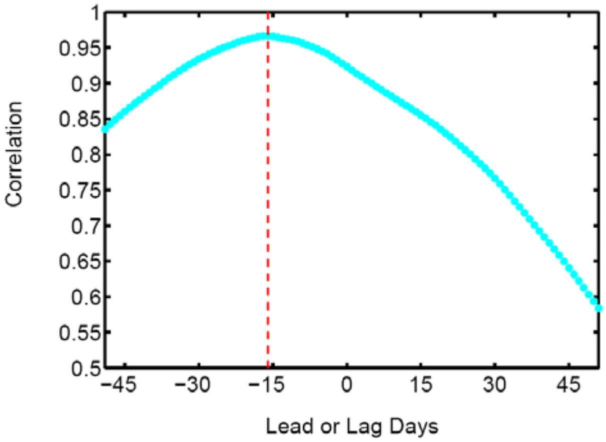

Figure 4.28 Lead-lag-correlation of anomalies in open water and daily cumulative solar heating to the Arctic Ocean for 2007 compared with the 21-year (1984-2004) mean. The x-axis represents the days when open water fraction varies ahead of or behind the solar heating. The red dash line is the location where the correlation has the maximum value (~0.97) at the 16th leading day.

Chapter 5: Summary and Discussion

The primary motivation for this study was to advance the quality of currently available information on SWR at high latitude so that available estimates of heat input into the polar oceans can be improved. Accurate information is also needed for investigating and quantifying the effect of the ice-albedo feedback on the extreme sea ice retreat in the Arctic Ocean during the past decade and for investigating long term trends between fractional open water and heat input into the Arctic Ocean. The following steps were taken:

1. Improve inference schemes for estimating SWR from satellite observations at high latitudes so that newly available information can be utilized; implement these schemes with improved auxiliary information on aerosols, clouds, and surface properties (e.g. albedo). This was done for models to be driven with MODIS observations at 1° resolution for the period of 2002-2010, and with MODIS observations at 5-km resolution for summer months of 2007). Inference schemes to be driven with AVHRR observations were also modified and implemented at 0.5° resolution for 1983-2006.

2. Evaluate the new updated SWR estimates based on satellite observations against ground measurements (land and ocean).

3. Apply the newly-derived high quality information to re-evaluate the influence of ice-albedo feedback on Arctic ice loss during the past decade, especially for the extreme ice loss year of 2007.

The two models (UMD_MODIS and UMD_AVHRR) were updated to meet the special challenges of high latitudes. The new inference schemes incorporate newly-developed narrow-to-broadband transformations for specific surface conditions at high latitudes; detailed angular corrections from CERES observations and model simulations; and used high quality information on water and ice clouds and surface properties taking into account the ice melting phases as available from MODIS and microwave products at high resolution.

Evaluations of the new schemes against high quality surface measurements from the ARM program at Barrow, AK, and against ground observations from BSRN sites (land) and buoy measurements (ocean) as far north as possible (due to the lack of oceanic observation at very high latitudes), have shown that the UMD_MODIS provides the best SWR estimates at high latitudes as compared to other satellite-based and reanalysis products. The bias of MODIS daily estimates against ground measurements at Barrow, AK made by the ARM program for 2002-2010 is -5.3 Wm^{-2} (about -4% of mean values), -5.3 Wm^{-2} (-7%), 1.0 Wm^{-2} (1%), -0.001 (0%) for surface downward SWR, upward SWR, net SWR, and surface albedo, respectively; bias is within 6% of mean observations for buoy measurements. It has been demonstrated that the surface albedo derived from the updated MODIS inference scheme can simulate the sea ice melting and freezing-up along the Arctic coastline very well as compared to ground observations. The MODIS observations are available only from 2002 on. Longer term record (1981-present) is available from AVHRR. Estimates from AVHRR were derived at 0.5° from 1983-2006. The evaluation results have shown that the AVHRR product agrees well with ground measurements. For instance, the bias against Barrow observations at a daily scale is

-4.7 Wm^{-2} (3% of mean values) and 2.37 Wm^{-2} compared to 32 BSRN sites at a monthly scale, although it has higher standard deviation than MODIS.

For the first time, the contribution of ice-albedo feedback to the sea ice loss in the Arctic Ocean, and particularly to the extreme losses in recent years have been quantitatively analyzed using the highest quality satellite-based radiation products from MODIS for the shorter term and AVHRR for the longer term. The results from this study give answers to the questions posed in *Chapter 1:*

- There is a positive trend in solar heat input directly into the Arctic Ocean (0.3% per year) and in open water fraction (0.8% per year) for the period of 1984-2009 at a 99% confidence level. The solar heat input is controlled by two factors: solar irradiance and open water fraction. There is a slight negative trend in the surface solar incident irradiance reaching the Arctic Ocean (60° N-90° N) which is consistent with the previous findings in the Arctic Region. The increases in open water fraction (decrease in sea ice extent) are found to be the main factor resulting in a positive trend in solar heat input into the Arctic Ocean for 1984-2009.
- There is a transition in the 26-year trend for two periods: (1) 1984-2002 with a slight positive trend in solar heat input (0.2% per year) and in open water fraction (0.5% per year) at a 99% confidence level; (2) 2003-2009 with an abrupt growth in trends for solar heat input (2.0% per year) and for open water fraction (1.9% per year) at a 75% confidence level, in which there is the extreme ice loss year in 2007.

- There is a positive correlation (0.7; 75% confidence level) between the variation of solar heat input into the Arctic Ocean and the open water fraction averaged from the Arctic Ocean for the period of 1984-2004; the correlation values become higher at the marginal seas (e.g., >0.95 for the East Siberian Sea, the Chukchi Sea, and the Beaufort Sea).
- For the recent years (2003-2009) with an obvious decrease in the sea ice extent (minimum in Sep. 2007), the correlation between the solar heating in the Arctic Ocean and the open water fraction reaches 0.99, and the correlation between the solar heat input into the Arctic ice-ocean system and Arctic sea ice loss during either melt season or summer months are 0.95 and 0.91 (75% confidence level).
- The computations from the high resolution MODIS products (5-km) show that the magnitude of the solar heating into the Arctic Ocean in 2007 is much higher than the mean value from 1984-2004 (maximum value of 300%), which most likely contributes to accelerated melting of the surface and bottom in sea ice and delays the winter freeze up.
- The maximum anomalous high values of the solar heat input into the Arctic Ocean are located at the same places as the maximum sea ice retreat.
- The lag correlation analysis has indicated that the melting in sea ice is about half a month ahead of the solar energy into the Arctic Ocean which results in the more solar energy into the ocean and further ice retreat in 2007.

In this study we developed the methodologies to improve the satellite based SWR estimates for high latitudes that can be used as tools for quantifying the local regional-scale ice-albedo feedback. Its potential uses are much wider. Future direction of this work includes:

- Further evaluations to include more available observation networks and datasets from the International Polar Year (IPY) 2007-08.
- Addition of ice melting information (ponds formation process) into surface properties of the inference scheme to account for more detailed sea ice variation.
- Extending the high resolution 5-km MODIS products to longer time records to be utilized for much wider studies, since it can provide the detailed information and also the diurnal cycle for the solar radiation.
- Incorporation of improved information on clouds and aerosols and their vertical distribution based on observations from A-train satellites, including the CLOUD SATellite (CloudSat) and Cloud-Aerosol Lidar and Infrared Pathfinder Satellite Observation (CALIPSO).Using these data, a better understanding of solar radiation budget at high latitudes is anticipated because the clouds play a very important role at these places.
- Improving our understanding of the mechanisms of sea ice loss in the Arctic Ocean by using the newly updated solar radiation products (UMD_AVHRR, UMD_MODIS) as forcing or validation data for model simulations.

Publications and presentations resulting from work:

Niu, X., and R. T. Pinker, 2011: Radiative fluxes at Barrow, Alaska: a satellite view. *Journal of Climate*, **24**, doi: 10.1175/JCLI-D-11-00062.1, 5494-5505.

Niu, X., and R. T. Pinker, 2011: Revisiting satellite radiative flux computations at the top of the atmosphere. *International Journal of Remote Sensing*, doi: 10.1080/01431161.2011.571298, 1-17.

Niu, X., R. T. Pinker, and M. F. Cronin, 2010: Radiative fluxes at high latitudes. *Geophysical Research Letters*, **37**, L20811, 1-5, doi: 10.1029/2010GL044606.

Pinker, R. T. and X. Niu, 2010: Radiative fluxes at high latitudes. *U. S. Climate Variability and Predictability (CLIVAR)*, *VARIATIONS*, 8 (1), 13-15.

Pinker, R. T., X. Niu, and Y. Ma, 2011: Radiative fluxes at high latitudes: Implications for climate research. WCRP Conference, Denver, Colorado, Oct. 24 -28, 2011.

Pinker, R. T., X. Niu, and Y. Ma, 2011: High-Latitude Surface Radiative Fluxes: Challenges for Climate Research. EGU General Assembly conference, Vol. 13, EGU2011-12610, 2011.

Niu, X., R. T. Pinker, and M. Wonsick, 2009: Development of Narrow-to-Broadband Transformations and Angular Dependence Models (ADM) for ABI onboard GOES-R. GOES-R AWG and Risk Reduction Review Meeting, July 2009, University of Maryland, College Park, MD, USA.

Wonsick, M., X. Niu, and R. T. Pinker, 2009: Evaluation of Narrow-to-Broadband Transformations and Angular Dependence Models (ADM) for ABI using

SEVIRI, GERB, and CERES. GOES-R AWG and Risk Reduction Review Meeting in July 2009, University of Maryland, College Park, MD, USA.

Niu, X., and R. T. Pinker, 2008: Synthesis of Angular Distribution Models (ADMs) for use in Radiative Flux Estimates from the Advanced Baseline Imager (ABI). 5th GOES User's Conference - 88th AMS meeting in January 20-24 2008, New Orleans, LA, USA.

Niu, X., R. T. Pinker, and M. Wonsick, 2010: Towards improved estimates of radiative fluxes at high latitudes. US CLIVAR/SeaFlux Workshop, March 17-19 2010, NCAR, Boulder, Colorado, USA.

Pinker, R. T., X. Niu, Y. Ma, and M. Wonsick, 2010: Surface and Top of the atmosphere radiative fluxes at high latitudes. US CLIVAR/SeaFlux Workshop, March 17-19 2010, NCAR, Boulder, Colorado.

Niu, X., R. T. Pinker, M. Wonsick, Y. Ma, and C. Li, 2009: Updated on narrow-to-broadband transformations and anisotropic corrections. NASA/GEWEX and UMD SRB Meeting, June 9-10, 2009, University of Maryland, College Park, MD, USA.

Niu, X., and R. T. Pinker, 2009: Impact of Improved Narrow-to-Broadband Transformations and Anisotropic Corrections on Satellite Estimates of Radiative Fluxes. International Conference on Land Surface Radiation and Energy Budgets held in March 18-20 2009, Beijing, China.

Niu, X., and R. T. Pinker, 2009: Radiative flux assessment activity at the University of Maryland. Institute of Tibetan Plateau Research, Chinese Academy of Sciences, March 27 2009, Beijing, China. *Invited*

Appendices

A.1 Test new methodologies with observations from METEOSAT-8/SEVIRI

The newly developed n/b transformations and synthesized ADMs mentioned in *Chapter 2* have been implemented with observations from SEVIRI on METEOSAT-8 *(Schmetz et al., 2002)* to derive TOA fluxes (called "SEVIRI fluxes") and have been evaluated against CERES TOA SW upward fluxes (SRBAVG products from Terra, called "CERES fluxes") *(Niu and Pinker, 2011).*

A.1.1 Updates of n/b transformation for SEVIRI

Previous attempts have been made on n/b conversion for SEVIRI (e.g., *Clerbaux et al., 2001, Cros et al., 2006, Clerbaux et al., 2008, Dewitte et al., 2008).* The methodology for the n/b conversion is either empirical or theoretical. The empirical method is statistical and based on specific satellite sensor. Studies of *Cros et al. (2006)* show -1% of bias and 6% RMSE of the mean radiance in the conversion of SEVIRI radiances in two visible channels into broadband radiances, which are not dependent on either surface type or the solar zenith angle. The theoretical ones are based on radiative transfer model simulations. *Clerbaux et al. (2008)* utilized the Santa Barbara discrete ordinate radiative transfer (DISORT) Atmospheric Radiative Transfer Model (SBDART, *Ricchiazzi et al., 1998)* associated with 750 different atmospheric conditions. The derived n/b conversions are dependent only on the Solar Zenith Angle (SZA) and do not include dependence on other viewing angles, surface types or cloudiness. In this study the n/b transformations are based on MODTRAN-3.7 simulations and dependent on SZA, viewing angles, surface types, and cloud phase and cloud optical depth. Compared with previously proposed methodologies, the n/b transformation coefficients developed in this study include viewing geometry corrections stratified by cloud information that have not been considered as before.

Previous studies on bi-directional corrections for METEOSAT have utilized the CERES-TRMM ADMs *(Bertrand et al., 2005, 2006; Dewitte et al., 2008),* classified according to surface types. These include: ocean, low to moderate tree/shrubs, moderate to high tree/shrubs, bright desert, and dark desert. In this study the CERES-TRMM surface type ADMs were extended to include all IGBP classification to be consistent with the n/b transformation formulation. Theoretical simulations of all cases were also performed and results were merged with the observational ADMs to improve the representation of under-sampled angular bins. The newly developed ADMs are a synergy of information from both observations and theoretical simulations since the CERES ADMs are under-sampled at higher viewing angles which are now augmented with the theoretical ones.

A.1.2 Evaluations of "SEVIRI fluxes" at TOA

The all-sky TOA upward SW SEVIRI fluxes on July 2004 at both instantaneous and daily time scales are illustrated in *Figures A.1 (a)* and *(b).* This study focused on the center region of the whole image, so that the issues of the distortion did not complicate the interpolation of the results. The *Figures A.2 (a)* and *(b)* show the monthly mean TOA upward SW fluxes from CERES observations (SRBAVG product, 1° resolution) and from SEVIRI fluxes (1/8° resolution), both of which have consistent distribution patterns (the differences between the two when reduced to 1° resolution is in the range of -10 to + 10 Wm^{-2}). Four months of SEVIRI fluxes (April-July, 2004) have been evaluated against CERES observations. The scatter plots *(Figures A.3 (a)* and *(b))* compare SEVIRI fluxes against CERES observations for both clear sky and all sky. The SEVIRI fluxes slightly overestimate by 4.8 Wm^{-2} for clear sky and slightly underestimate by 2.5 Wm^{-2} for all sky compared to CERES observations. The RMSE of SEVIRI fluxes are 5.9 Wm^{-2} and the correlation is 0.98 for both clear and all sky. Cases where estimates were outside the range of 3 standard deviations (std) were eliminated. As an example, using several IGBP surface types (water, desert, grassland, open shrubs, savannas, and crops) for all sky, scatter plots show that the bias of SEVIRI fluxes are -2~-7 Wm^{-2} and the RMSE are about 6 Wm^{-2} compare to CERES observations. The evaluations of all sky fluxes for the other months in 2004 are similar to these four months: bias of -3.2 Wm^{-2} and RMSE of 6.5 Wm^{-2} for February and March; bias of -2.7 Wm^{-2} and RMSE of 6.9 Wm^{-2} for period of August to December. Further evaluations at TOA will be performed with Geostationary Earth Radiation Budget Experiment (GERB) which is onboard METEOSAT-8 and has co-located observations with SEVIRI *(Niu and Pinker, 2011).*

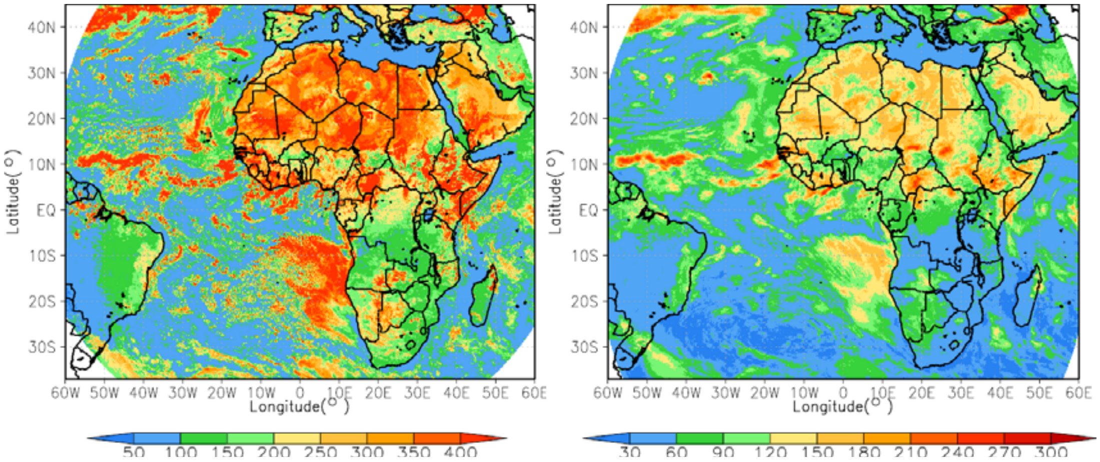

(a) (b)

Figure A.1 All sky TOA upward SW SEVIRI fluxes (Wm^{-2}) at time scales of: (a) instantaneous (13 UTC, July 1, 2004) and (b) daily averaged (July 1, 2004).

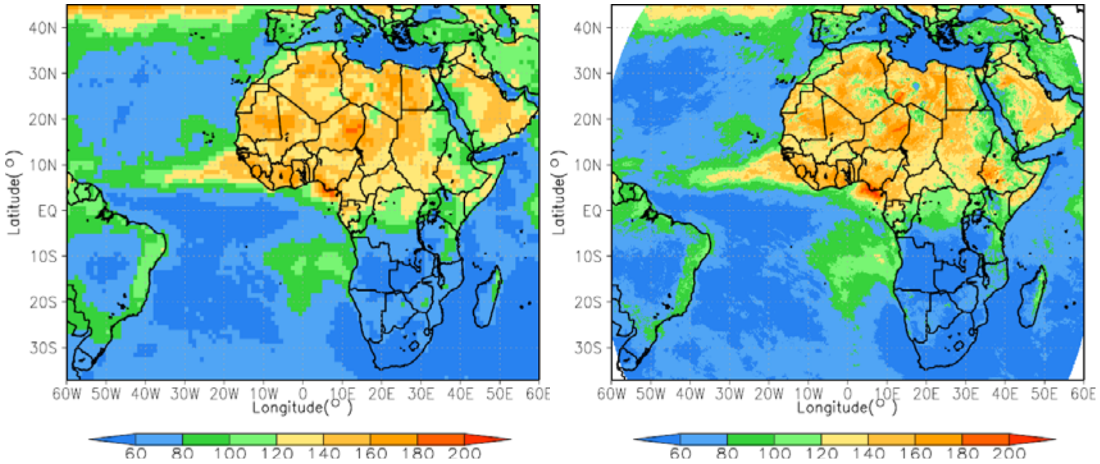

(a) (b)

Figure A.2 All sky monthly mean TOA SW upward fluxes (Wm^{-2}) from (a) CERES observations (SRBAVG product) at 1° resolution and from (b) SEVIRI fluxes at 1/8° resolution for July 2004.

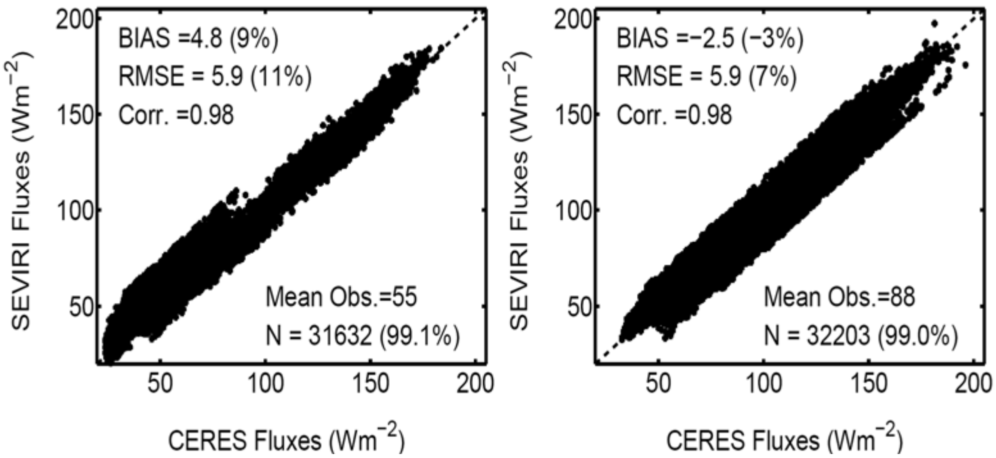

(a) (b)

Figure A.3 Evaluation of all sky monthly mean TOA upward SW SEVIRI fluxes against CERES observations for clear sky (a) and all sky (b), for 4 months (April – July), 2004. Cases outside of 3 std were eliminated (0.9% for clear sky and 1.0% for all sky).

Bibliography

Arctic Climate Impact Assessment, 2004: Impacts of a Warming Arctic: Arctic Climate Impact Assessment. Cambridge Univ. Press, New York, 139.

Ackerman, T. P., and G. M. Stokes, 2003: The atmospheric radiation measurement program. *Physics Today*, **56** (1), 38-44.

Armstrong, R. L., and M. J. Brodzik, 2001: Recent Northern Hemisphere Snow Extent: a Comparison of Data Derived from Visible and Microwave Sensors. *Geophysical Research Letters*, **28** (19), 3673-3676.

Arnold, G. T., S.-C. Tsay, M. D. King, J. Y. Li, and P. F. Soulen, 2002: Airborne spectral measurements of surface-atmosphere anisotropy for arctic sea ice and tundra. *International Journal of Remote Sensing*, **23** (18), 3763-3781.

Bäumer, D., B. Vogel, S. Versick, R. Rinke, O. Möhler, and M. Schmaiter, 2008: Relationship of visibility, aerosol optical thickness and aerosol size distribution in an ageing air mass over South-West Germany. *Atmospheric Environment*, **42**, 989-998.

Belchansky, G. I., D. C. Douglas, and N. G. Platonov, 2004: Duration of the Arctic Sea Ice Melt Season: Regional and Interannual Variability, 1979-2001. *Journal of Climate*, **17**, 67-80.

Berk, A., L. S. Bernstein, and D. C. Robertson, 1983: MODTRAN: A moderate resolution model for LOWTRAN 7. Philips Laboratory, Report AFGL-TR-83-0187, Hanscom AFB, MA.

Bernhard, G., C. R. Booth, J. C. Ehramjian, R. Stone, and E. G. Dutton, 2007: Ultraviolet and visible radiation at Barrow, Alaska: Climatology and influencing factors on the basis of version 2 National Science Foundation network data. *Journal of Geophysical Research*, **112**, D09101, doi:10.1029/2006JD007865, 1-19.

Bertrand, C., N. Clerbaux, A. Ipe, S. Dewitte, and L. Gonzalez, 2005: Angular distribution models, anisotropic correction factors, and mixed clear-scene types: A sensitivity study. *IEEE Transactions on Geoscience and Remote Sensing*, **43** (1), pp. 92-102.

Bertrand, C., N. Clerbaux, A. Ipe, S. Dewitte, and L. Gonzalez, 2006: Angular distribution models anisotropic correction factors and sun glint: a sensitivity study. *International Journal of Remote Sensing*, **27** (9-10), pp. 1741-1757.

Boe, J., A. Hall, and X. Qu, 2009: Current gcms unrealistic negative feedback in the Arctic. *Journal of Climate*, **19** (11), 2437-2450.

Brest, C. L., and W. B. Rossow, 1992: Radiometric calibration and monitoring of NOAA AVHRR data for ISCCP. *International Journal of Remote Sensing*, **13**, 235-273.

Briegleb, B. P., P. Minnis, V. Ramanathan, and E. Harrison, 1986: Comparison of regional clear-sky albedos inferred from satellite observations and model calculations. *Journal of Climate and Applied Meteorology*, **25**, 214-226.

Briegleb, B. P., and D. H. Bromwich, 1998: Polar Radiation Budgets of the NCAR CCM3. *Journal of Climate*, **11**, 1246-1269.

Brown, R., C. Derksen, and L. Wang, 2010: A multi-data set analysis of variability and change in Arctic spring snow cover extent, 1967-2008. *Journal of Geophysical Research*, **115**, D16111, doi:10.1029/2010JD013975, 1-16.

Byrkjedal, Ø., I. Esau, and N. G. KvamstØ, 2008: Sensitivity of simulated wintertime Arctic atmosphere to vertical resolution in the ARPEGE/IFS model. *Climate Dynamics*, **30**, 687-701, doi: 10.1007/s00382-007-0316-z.

Cassano, E. N., A. H. Lynch, J. J. Cassano, M. R. Koslow, 2006: Classification of synoptic patterns in the western Arctic associated with extreme events at Barrow, Alaska, USA. *Climate Research*, **30**, 83-97.

Cavalieri, D., C. Parkinson, P. Gloersen, and H. J. Zwally, 1996, updated 2008: Sea ice concentrations from Nimbus-7 SMMR and DMSP SSM/I passive microwave data, [2007]. Boulder, Colorado USA: National Snow and Ice Data Center. Digital media.

Chapin III, F. S., and coauthor, 2005: Role of Land-Surface Changes in Arctic Summer Warming. *Science*, **310** (28 October 2005), no. 5748, 657-660.

Chedin, A., N. A. Scott, C. Wahiche, and P. Moulinier, 1985: The improved initialization inversion method: a high resolution physical method for temperature retrievals from satellites of the TIROS-N series. *Journal of Climate and Applied Meteorology*, **24**, 128-143.

Clerbaux., N., S. Dewitte, L. Gonzalez, A. Ipe, and B. Nicula, 2001: Derivation of the Top of the Atmosphere Radiative Fluxes from SEVIRI: Methodology, Accuracy and Perspectives. In Proc. of the 2001 EUMESAT Meteorological Satellite Data User's Conference, Antalya, 69-76.

Clerbaux., N., S. Dewitte, C. Bertrand, D. Caprion, B. De Paepe, L. Gonzalez, and A. Ipe, 2008: Unfiltering of the Geostationary Earth Radiation Budget (GERB) data. Part I: Shortwave radiation. *Journal of Atmospheric and Oceanic Technology*, **25** (7), 1087-1105.

Comiso, J. C., 2003: Warming trends in the Arctic from clear sky satellite observations. *J. Climate*, **16**, 3498-3510.

Comiso, J. C., C. L. Parkinson, R. Gersten, and L. Stock, 2008: Accelerated decline in the Arctic sea ice cover. *Geophysical Research Letters*, **35**, L01703, doi:10.1029/2007GL031972, 1-6.

Croll, J., 1875: Climate and Time in their Geological Relations, a Theory of Secular Change of the Earth's Climate, Daldy, Ibister & Co., London, 577.

Cros, S., M. Albuisson, and L. Wald, 2006: Simulating Meteosat-7 broadband radiances using two visible channels of Meteosat-8. *Solar Energy*, **80**, 361-367.

Curry, J. A., and E. E. Ebert, 1992: Annual cycle of radiation fluxes over the Arctic Ocean: Sensitivity to cloud optical properties. *Journal of Climate*, **5**, 1267-1280.

Curry, J. A., and J. L. Schramm, 1995: Sea Ice-Albedo Climate Feedback Mechanism. *Journal of Climate*, **8**, 240-247.

Curry, J. A., P. V. Hobbs, M. D. King, D. A. Randall, and P. Minnis, 2000: PIRE Arctic Clouds Experiment. *Bulletin of the American Meteorological Society*, **81** (1), 5-29.

Curry, J. A. and J. L. Schramm, 2001: Applications of SHEBA/FIRE data to evaluation of snow/ice albedo parameterizations. *Journal of Geophysical Research*, **106**, NO. D14, 15345-15355.

Dewitte, S., L. Gonzalez, N. Clerbaux, A. Ipe, C. Bertrand, and B. De Paepe, 2008: The geostationary earth radiation budget edition 1 data processing algorithms. *Advances in Space Research*, **41** (11), 1906-1913.

Dingman, S. L., R. G. Barry, G. Weller, C. Benson, E. F. LeDrew, and C. W. Goodwin, 1980: Climate, snow cover, microclimate, and hydrology. An Arctic Ecosystem: The coastal tundra at Barrow, Alaska, J. Brown et al., Eds., Institute of Ecology, 30-65.

Dong, X., B. Xi, K. Crosby, C. N. Long, R. S. Stone, and M. D. Shupe, 2010: A 10 year climatology of Arctic cloud fraction and radiative forcing at Barrow, Alaska. *Journal of Geophysical Research*, **115**, D17212, doi: 10.1029/2009JD013489, 1-14.

Geier, E. B., R. N. Green, D. P. Kratz, P. Minnis, W. F. Miller, S. K. Nolan, and C. B. Franklin, 2003: Single satellite footprint TOA/surface fluxes and clouds (SSF) collection document Release 2 Version 1, from NASA Langley Research Center Climate Science Branch Science Directorate, Hampton, VA. [The document is available online at http://science.larc.nasa.gov/ceres/collet_guide/pdf/SSF_CG._R2V1.pdf]

Gillespie, A., S. Rokugawa, T. Matsunaga, J. S. Cothern, S. Hook, and A. B. Kahle, 1998: A temperature and emissivity separation algorithm for Advanced Spaceborne Thermal Emission and Reflection Radiometer (ASTER) images. *IEEE Transactions on Geoscience Remote Sensing*, **36**, 1113-1126.

Gupta, S. K., D. P. Kratz, P. W. Stackhouse Jr., and A. C. Wilber, 2001: The Langley parameterized shortwave algorithm for surface radiation budget studies (Vers. 1.0). *NASA/TP-2001-211272*, 31 pp.

Gutman, G. and A. Ignatov, 1998: The derivation of the green vegetation fraction from NOAA/AVHRR data for use in numerical weather prediction models. *International Journal of Remote Sensing*, **19** (8), 1533-1543.

Francis, J. A., and E. Hunter, 2006: New insight into the disappearing Arctic sea ice. *Eos Trans. of AGU*, **87**, 509-524.

Hall, A., 2004: The Role of Surface Albedo Feedback in Climate. *Journal of Climate*, **17**, 1550-1568.

Hall, D. K., G. A. Riggs, and V. V. Salomonson, 2006: updated daily. MODIS/Terra Snow Cover Daily L3 Global 0.05deg CMG V005, [January 2002 to June 2010]. Boulder, Colorado USA: National Snow and Ice Data Center. Digital media.

Hansen, M. C., R. S. Defries, J. R. G. Townshend, and R. Solhberg, 2000: Global land cover classification at 1 km spatial resolution using a classification tree approach. *International Journal of Remote Sensing*, **21**, Issue 6-7, 1331-1364.

Hinzman, L. D., N. D., Bettez, W. R. Bolton, F. S. Chapin, M. B. Dyurgerov, C. L. Fastie, B. Griffith, R. D. Hollister, A. Hope, H. P. Huntington, A. M. Jensen, G. J. Jia, T. Jorgenson, D. L. Kane, D. R. Klein, G. Kofinas, A. H. Lynch, A. H. Lloyd, A. D. McGuire, F. E. Nelson, W. C. Oechel, T. E. Osterkamp, C. H. Racine, V. E. Romanovsky, R. S. Stone, D. A. Stow, M. Sturm, C. E. Tweedie, G. L. Vourlitis, M. D. Walker, D. A. Walker, P. J. Webber, J. M. Welker, K. S.

Winker, K. Yoshikawa, 2005: Evidence and implications of recent climate change in northern Alaska and other arctic regions. *Climatic Change*, **72**, 251-298.

Hodges, G. B. and J. J. Michalsky, 2011: Multifilter Rotating Shadowband Radiometer, Multifilter Radiometer, and Normal Incidence Multifilter Radiometer Handbook. DOE/SC-ARM/TR-059, January 2011, 1-13.

Holland, M. M., and C. Bitz, 2003: Polar amplification of climate change in the coupled model intercomparison project. *Clim. Dyn.*, **21**, 221-232.

Holland, M. M., C. M. Bitz, and B. Tremblay, 2006: Future abrupt reductions in the summer Arctic sea ice. *Geophys. Res. Lett.*, **33**, L23503, doi:10.1029/2006GL028024.

Holland, M. M., M. C. Serreze, and J. Stroeve, 2008: The sea ice mass budget of the Arctic and its future change as simulated by coupled climate models. *Climate Dynamics*, **34**, DOI: 10.1007/s00382-008-0493-4, 185-200.

Holland, M. M., D. A. Bailey, and B. P. Briegleb, 2011: Improved sea ice shortwave radiation physics in CCSM4: the impact of melt ponds and aerosols on Arctic sea ice. *Journal of Climate*, in press.

Houghton, J. T., and coauthors, 2001: Climate Change 2001: The Scientific Basis. The Intergovernmental Panel on Climate Change (IPCC) 2001.

Hwang, Y., D. M. W. Frierson, and J. E. Kay, 2011: Coupling between Arctic feedbacks and changes in poleward energy transport. *Geophysical Research Letters*, **38**, L17704, doi:10.1029/2011GL048546, 1-5.

IGBP, 1993: The International Geosphere Biosphere Programme's task force on global analysis, interpretation and modeling (GAIM). IGBP Report, Stockholm.

Intrieri, J. M., C. W. Fairall, M. D. Shupe, P. O. G. Persson, E. L. Andreas, P. S. Guest, and R. E. Moritz, 2002: An annual cycle of Arctic surface cloud forcing at SHEBA. *Journal of Geophysical Research*, **107**, NO.C10, 8039, doi: 10.1029/2000JC000439.

Inoue, J., J. Liu, J. O. Pinto, and J. A. Curry, 2006: Intercomparison of Arctic Regional Climate Models: Modeling Clouds and Radiation for SHEBA in May 1998. *Journal of Climate*, 4167-4178.

Jin, Z., K. Stamnes, and W. F. Weeks, 1994: The effect of sea ice on the solar energy budget in the atmosphere-sea ice-ocean system: A model study. *Journal of Geophysical Research*, **99**, NO. C12, 25281-25294.

Kanamitsu, M., W. Ebisuzaki, J. Woollen, S-K Yang, J. J. Hnilo, M. Fiorino, and G. L. Potter, 2002: NCEP-DEO AMIP-II Reanalysis (R-2). *Bulletin of the American Meteorology Society,* November 2002, 1631-1643.

Kassabova, T., R. T. Pinker, and I. Laszlo, 2002: Updated surface spectral reflectance models compatible with current global land cover classifications. This is a paper presented at a conference. In 11th AMS Conference on Atmospheric Radiation, 3-7 June 2002, Ogden, Utah.

Kay, J. E., T. L'Ecuyer, A. Gettelman, G. Stephens, and C. O'Dell, 2008: The contribution of cloud and radiation anomalies to the 2007 Arctic sea ice extent minimum. *Geophysical Research Letters*, **35**, L08503, doi: 10.1029/2008GL033451.

Kay, J. E., and A. Gettelman, 2009: Cloud influence on and response to seasonal Arctic sea ice loss. *Journal of Geophysical Research*, **114**, D18204, doi:10.1029/2009JD011773, 1-18.

Key, J. R., and A. J. Schweiger, 1998: Tools for atmospheric radiative transfer: Streamer and FluxNet. *Comput. Geosci.*, **24**, 443-451.

Key, J. R., 2001: The Cloud and Surface Parameter Retrieval (CASPR) System for Polar AVHRR Data User's Guide. *Space Science and Engineering Center*, University of Wisconsin, Madison, WI, pp. 62.

Key, J. R., 2002a: The cloud and surface parameter retrieval (CASPR) system for polar AVHRR. Cooperative Institute for Meteorological Satellite Studies, University of Wisconsin-Madison, 59 pp. (available online at http://stratus.ssec.wisc.edu/caspr/documentation.html.).

Key, J. R., 2002b: Streamer user's guide. Cooperative Institute for Meteorological Satellite Studies, University of Wisconsin-Madison, 107 pp. (available online at http://stratus.ssec.wisc.edu/caspr/documentation.html.).

Key, J. R., D. Santek, C. S. Velden, N. Bormann, J. Thépaut, L. P. Riishojgaard, Y. Zhu, and W. P. Menzel, 2003: Cloud-Drift and Water Vapor Winds in the Polar Regions from MODIS. *IEEE Transactions on Geoscience and Remote Sensing*, **41** (2), 482-492.

King, M. D., Y. J. Kaufman, W. P. Menzel, and D. Tanré, 1992: Remote Sensing of Cloud, Aerosol, and Water Properties from the Moderate Resolution Imaging Spectrometer (MODIS). *IEEE Transactions on Geoscience and Remote Sensing*, **30** (1), 2-27.

King, M. D., Member, IEEE, W. P. Menzel, Y. J. Kaufman, D. Tanré, B.-C. Gao, S. Platnick, S. A. Ackerman, L. A. Remer, R. Pincus, and P. A. Hubanks, 2003: Cloud and Aerosol Properties, Precipitable Water, and Profiles of Temperature and Water Vapor from MODIS. *IEEE Transactions on Geoscience and Remote Sensing*, **41** (2), 442-458.

Kubota, M., N. Iwabe, M. F. Cronin, and H. Tomita, 2008: Surface heat fluxes from the NCEP/NCAR and NCEP/DOE reanalyses at the Kuroshio Extension Observatory buoy site. *J. Geophys. Res.,* **113**, C02009, doi:10.1029/2007JC004338.

Lindsay, R.W., and J. Zhang, 2005: The Thinning of Arctic Sea Ice, 1998-2003: Have we reached the tipping point? Paper presented at 8th Conferece on Polar Meteor. And Oceanog., Amer. Meteor. Soc., San Diego, Calif.

Linkin, M. E., 2008: NORTH PACIFIC CLIMATE VARIABILITY AND ARCTIC SEA ICE. Ph. D. dissertation. Department of Atmospheric and Oceanic Science, University of Maryland, College Park, MD. Advisor: Professor Sumant Nigam, Department of Atmospheric and Oceanic Science.

Liu, H. and R. T. Pinker, 2008: Radiative Fluxes from Satellites: Focus on Aerosols. *Journal of Geophysical Research*, **113**, D08208, doi: 10.1029/2007JD008736, 1-10.

Liu, J. and J. A. Curry, 2004: Recent Arctic Sea Ice variability: connections to the Arctic Oscillation and the ENSO. *Geophysical Research Letters*, **31**, L09211, doi: 10.1029/2004GL019858.

Liu, J., J. A. Curry, W. B. Rossow, J. R. Key, and X. Wang, 2005: Comparison of surface radiative flux data sets over the Arctic Ocean. *Journal of Geophysical Research*, **110**, C02015, doi: 10.1029/2004JC002381, 1-13.

Loeb, N. G., N. M. Smith, S. Kato, W. F. Miller, S. K. Gupta, P. Minnis, and B. A. Wielicki, 2003: Angular distribution models for top-of-atmosphere radiative flux estimation from the Clouds and the Earth's Radiant Energy System Instrument on the Tropical Rainfall Measuring Mission Satellite. Part I: Methodology. *Journal of Applied Meteorology*, **42**, 240-265.

Loeb, N. G., S. Kato, K. Loukachine, and N. Manalo-Smith, 2005: Angular distribution models for top-of-atmosphere radiative flux estimation from the Clouds and the Earth's Radiant Energy System Instrument on the Terra Satellite. Part I: Methodology. *Journal of Atmospheric and Oceanic Technology*, **22**, 338-351.

Ma, Y., and R. T. Pinker, 2011: Shortwave Radiatiev Fluxes from Satellites: An update. *JGR-Atmospheres*, submitted.

Mahlstein, I., and R. Knutti, 2011: Ocean heat transport as a cause for model uncertainty in projected arctic warming. *Journal of Climate*, **24** (5), 1451-1460.

Manabe, S., M. J. Spelman, and R. J. Stouffer, 1992: Transient responses of a coupled ocean-atmosphere model to gradual changes of atmospheric CO_2. Part II: Seasonal response. *J. Climate*, **5**, 105-126.

Maslanik, J., S. Drobot, C. Fowler, W. Emery, and R. Barry, 2007: On the Arctic climate paradox and the continuing role of atmospheric circulation in affecting sea ice conditions. *Geophysical Research Letters*, **34**, L03711, doi: 10.1029/2006GL028269.

Maykut, G. A., and P. E. Church, 1973: Radiation climate of Barrow, Alaska: 1962-1966. *Journal of Applied Meteorology*, **12**, 620-628.

Maykut, G. A., and M. G. McPhee, 1995: Solar heating of the Arctic mixed layer. *Journal of Geophysical Research*, **100**, 24, 691-24,703.

Menge, J. R., S. Nghiem, D. Perovich, and I. Rigor, 2007: Sea Ice Cover, Arctic Report Card 2007, October, 2007.

Moddy, E. G, M. D. King, S. Platnick, C. B. Schaaf, and F. Gao, 2005: Spatial complete global spectral surface albedos: value-added datasets derived from Terra MODIS land produts. *IEEE Transactions on Geoscience and Remote Sensing*, **43** (1), 144-158.

Moody, E. G., M. D. King, C. B. Schaaf, D. K. Hall, and S. Platnick, 2007: North Hemisphere five-year average (2000-2004) spectral albedos of surface in the presence of snow: statistics computed from Terra MODIS land products. *Remote Sensing of Environment*, **111**, 337-345.

Nghiem, S. V., I. G. Rigor, D. K. Perovich, P. Clemente-Colón, J. W. Weatherly, and G. Neumann, 2007: Rapid reduction of Arctic perennial sea ice. *Geophysical Research Letters*, **34**, L19504, doi: 10.1029/2007GL031138.

Niu, X., and R. T. Pinker, 2011: Revisiting satellite radiative flux computations at the top of the atmosphere. *International Journal of Remote Sensing*, doi: 10.1080/01431161.2011.571298, 1-17.

Niu, X., and R. T. Pinker, 2011: Radiative fluxes at Barrow, Alaska: a satellite view. *Journal of Climate*, **24**, doi: 10.1175/JCLI-D-11-00062.1, 5494-5505.

Niu, X., and R. T. Pinker, and M. F. Cronin, 2010: Radiative fluxes at high latitudes. *Geophysical Research Letters*, **37**, L20811, 1-5, doi: 10.1029/2010GL044606.

Ogi, M., and J. M. Wallace, 2007: Sumer minimum Arctic sea ice extent and the associated summer atmospheric circulation. *Geophysical Research Letters*, **34**, L12705, doi: 10.1029/2007GL029897.

Ohmura, A., and Coauthors, 1998: Baseline surface radiation network (BSRN/WCRP): New precision radiometry for climate research. *Bull. Amer. Meteor. Soc.*, **79**, 2115-2136.

Overland, J., L. Bengtsson, R. Przybylak, and J. Walsh, 2007: Atmosphere, Arctic Report Card 2007, October, 2007.

Overpeck, J., and Coauthors, 1997: Arctic environmental change of the last four centuries. *Science*, **278**, 1251-1256.

Parry, M. L., O. F. Canziani, J. P. Palutikof, P. J. van der Linden, and C. E. Hanson, ed., 2007: IPCC AR4 WG2 (2007), Climate Change 2007: Impacts, Adaptation and Vulnerability, Contribution of Working Group II to the Fourth Assessment Report of the Intergovernmental Panel on Climate Change, Cambridge University Press, ISBN 978-0-521-88010-7, http://www.ipcc.ch/publications_and_data/ar4/wg2/en/contents.html (pb: 978-0-521-70597-4).

Parkinson, C. L., 1992: Spatial patterns of increases and decreases in the length of the sea ice season in the marginal ice zone. *J. Geophys. Res.*, **92** (C7), 6825-6835.

Perovich, D. K., E. L. Andreas, J. A. Curry, H. Eiken, C. W. Fairall, T. C. Grenfell, P. S. Guest, J. Intrieri, D. Kadko, R. W. Lindsay, M. G. Mcphee, H. Morison, R. E. Moritz, C. A. Paulson, W. S. Pegau, P. O. G. Persson, R. Pinkel, J. A. Richter-Menge, T. Stanton, H. Stern, M. Sturm, W. B. Tucker III, and T. Uttal, 1999: Year on ice gives climate insights. *Eos Trans. AGU*, **80** (41), 481, 485-486.

Perovich, D. K., T. C. Grenfell, B. Light, and P. V. Hobbs, 2002: Seasonal evolution of the albedo of multiyear Arctic sea ice. *Journal of Geophysical Research*, **107**, No. C10, 8044, doi: 10.1029/2000JC00438.

Perovich, D. K., S. V. Nghiem, T. Markus, and A. Schweiger, 2007: Seasonal evolution and interannual variability of the local solar energy absorbed by the Arctic sea ice-ocean system. *Journal of Geophysical Research*, **112**, C03005, doi: 10.1029/2006JC003558.

Perovich, D. K., B. Light, H. Eicken, K. F. Jones, K. Runciman, and S. V. Nghiem, 2007: Increasing solar heating of the Arctic Ocean and adjacent seas, 1979-2005: Attributing and role in the ice-albedo feedback. *Geophysical Research Letters*, **34**, L19505, doi: 10.1029/2007GL031480.

Perovich, D. K., J. A. Richter-Menge, K. F. Jones, and B. Light, 2008: Sunlight, water, and ice: Extreme Arctic sea ice melt during the summer of 2007. *Geophysical Research Letters*, **35**, L11501, doi: 10.1029/2008GL034007, 1-4.

Persson, P. O. G., C. W. Fairall, E. Andreas, P. Guest, and D. K. Perovich, 2002: Measurements near the atmospheric surface flux group tower at SHEBA: Near-surface conditions and surface energy budget. *J. Geophys. Res.*, **107** (C10), 8045, doi: 10.1029/2000JC000705.

Philipona, R., 2002: Underestimation of solar global and diffuse radiation measured at Earth's surface. *J. Geophys. Res.*, **107** (D22), 4654, doi: 10.1029/2002JD002396.

Pinker, R. T., and J. A. Ewing, 1985: Modeling Surface Solar Radiation: Model Formulation and Validation. *Journal of Climate and Applied Meteorology*, **24** (5), 389-401.

Pinker, R. T., and I. Laszlo, 1992: Modeling Surface Solar Irradiance for Satellite Applications on a Global Scale. *Journal of Applied Meteorology*, **31** (February 1992), 194-211.

Pinker, R. T., J. D. Tarpley, I. Laszlo, K. E. Mitchell, et al., 2003: Surface Radiation Budgets in Support of the GEWEX Continental Scale International Project (GCIP) and the GEWEX Americas Prediction Project (GAPP), including the North American Land Data Assimilation System (NLDAS) Project. *J. Geophys. Res.*, **108** (D22), 8844, doi:10.1029/2002JD003301.

Pinker, R. T., Wang, H., King, M. D., and Platnick, S., 2003: The First Use of MODIS Data to Cross-Calibrate with GEWEX/SRB Data Sets. *GEWEX NEWS*, **13** (4).

Pinker, R. T., B. Zhang, and E. G. Dutton, 2005: Do satellites detect trends in surface solar radiation? *Science*, **308**, 850-854.

Pinker R. T., X. Li, W. Meng, and E. A. Yegorova, 2007: Toward improved satellite estimates of short-wave radiative fluxes—Focus on cloud detection over snow: 2. Results. *J. Geophys. Res.*, **112**, D09204, doi:10.1029/2005JD006699.

Pinker, R. T., H. Wang, and S. A. Grodsky, 2009: How good are ocean buoy observations of radiative fluxes? *Geophysical Research Letters*, **36**, L10811, 1-5.

Platnick, S., M. D. King, S. A. Ackerman, W. P. Menzel, B. A. Baum, J. C. Riédi, and R. A. Frey, 2003: The MODIS cloud products: Algorithms and examples from Terra. *IEEE Trans. Geosci. Remote Sensing*, **41**, 459-473.

Ray, P., 1885: Report of the international polar expedition to point Barrow, Alaska. U. S. Government Printing Office, Washington, DC, pp. 686.

Ricchiazzi, P., S. Yang, C. Gautier, and D. Sowle, 1998: SBDART: A research and teaching software tool for plane-parallel radiative transfer in the earth's atmosphere. *Bulletin of the American Meteorological Society*, **79**, 2101-2114.

Rinke, A., et al., 2006: Evaluation of an ensemble of Arctic regional climate models: spatiotemporal fields during the SHEBA year. *Climate Dynamics*, **26**, 459-472, doi: 10.1007/s00382-005-0095-3.

Rossow, W. B., and R. A. Schiffer, 1991: ISCCP Cloud Data Products. *Bull. Amer. Meteor. Soc.*, **71**, 2-20.

Rossow, W. B., A. W. Walker, D. E. Beuschel, and M. D. Roiter, 1996: International Satellite Cloud Climatology Project (ISCCP) Documentation of New Cloud Datasets. WMO/TD-No. 737, World Meteorological Organization, 115 pp.

Schmetz, J., P. Pili., S. Tjemkes, D. Just, J. Kerkmann, S. Rota, and A. Ratier, 2002: An Introduction to METEOSAT Second Generation (MSG). *Bulletin of the American Meteorological Society*, **83**, 977-992.

Screen, J. A. and I. Simmonds, 2010: The central role of diminishing sea ice in recent Arctic temperature amplification. *Nature*, **464**, 29 April 2010, doi:10.1038/nature09051, 1334-1337.

Screen, J. A. and I. Simmonds, 2010: Increasing fall-winter energy loss from the Arctic Ocean and its role in Arctic temperature amplification. *Geophysical Research Letters*, **37**, L16707, doi:10.1029/2010GL044136, 1-5.

Sellers, W. D., 1969: A global climatic model based on energy balance of the Earth-atmosphere system. *J. Appl. Meteorol.*, **8**, 392-400.

Serreze, M. C., and Coauthors, 2000: Observational evidence of recent change in the northern high-latitude environment. *Climatic Change*, **46**, 159-207.

Serreze, M. C., and J. A. Francis, 2006: The Arctic Amplification Debate. *Climate Change*, **76**, 241-264, Doi: 10.1007/s10584-005-9017-y.

Serreze, M. C., A. P. Barrett, J. C. Stroeve, D. N. Kindig, and M. M. Holland, 2009: The emergence of surface-based Arctic amplification. *The Cryosphere*, **3**, 11-19.

Sorteberg, A., W. Kattsov, J. E. Walsh, and T. Pavlova, 2007: The Arctic Surface Energy Budget as Simulated with the IPCC AR4 AOGCMs. *Climate Dynamics*, **29**, 131-156, doi: 10.1007/s00382-006-022209.

Stackhouse, P. W., S. K. Gupta, S. J. Cox, J. C. Mikovitz, T. Zhang, M. Chiacchio, 2004: 12-year surface radiation budget data set. *GEWEX News*, **14**, 10-12.

Stamnes, K., S.-C. Tsay., W. Wiscombe, and K. Jayaweer, 1988: Numerically stable algorithm for discrete-ordinate-method radiative transfer in multiple scattering and emitting layered media. *Applied Optics*, **27**, no. 12, pp. 2502-2509.

Stamnes, L., R. G. Ellingson, J. A. Curry, J. E. Walsh, and B. D. Zak, 1999: Review of science issues, development strategy, and status for the ARM North Slope of Alaska-Adjacent Arctic Ocean climate research site. *Journal of Climate*, **12**, 46-63.

Steele, M., W. Ermold, and J. Zhang, 2008: Arctic Ocean surface warming trends over the past 100 years. *Geophysical Research Letters*, **35**, L102614, doi:10.1029/2007GL031651, 1-6.

Steffen, K., J. E. Box, and W. Abdalati, 1996: "Greenland Climate Network: GC-Net", in Colbeck, S. C. Ed. CRREL 96-27 Special Report on Glaciers, Ice Sheets and Volcanoes, trib. to M. Meier, pp. 98-103.

Stephens, G. L., D. G. Vane, R. J. Boain, G. G. Mace, K. Sassen, Z. Wang, A. J. Illingworth, E. J. O'Connor, W. B. Rossow, S. L. Durden, S. D. Miller, R. T. Austin, A. Benedetti, C. Mitrescu, and the CloudSat Science Team, 2002: The CloudSat mission and the A-Train: A new dimension of spacebased observations of clouds and precipitation. *Bulletin of the American Meteorology Society*, **83**, 1771-1790.

Stone, R. S., 1997: Variations in western Arctic temperatures in response to cloud radiative and synoptic-scale influences. *Journal of Geophysical Research*, **102**, 21769-21776, doi: 10.1029/97JD01840.

Stone, R. S., E. G. Dutton, J. M. Harris, and D. Longenecker, 2002: Earlier spring snowmelt in northern Alaska as an indicator of climate change. *Journal of Geophysical Research*, **107**, 1-14, No. D10, 4089, doi: 10.1029/2000JD000286.

Stone, R. S., D. C. Douglas, G. I. Belchansky, S. D. Drobot, and J. Harris, 2005: Cause and effect of variations in western Arctic snow and sea ice cover. In the 8th Conference on Polar Meteorology and Oceanography, Session 8, the Cryosphere-Sea Ice Extent, San Diego, CA, 12 January 2005.

Stroeve, J., M. Serezze, S. Drobot, S. Gearheard, M. Holland, J. Maslanik, W. Meier, and T. Scambos, 2008: Arctic sea ice plummets in 2007. *EOS Trans. AGU*, **89**, 13.

Stroeve, J. C., M. C. Serreze, M. M. Holland, J. E. Kay, J. Malanik, and A. P. Barrett, 2011: The Arctic's rapidly shrinking sea ice cover: a research synthesis. *Climate Change*, doi: 10.1007/s10584-011-0101-1.

Sturm, M., 2000: Arctic winter and snow cover: Five distinct stages with implications for living things. *Eos, Trans. Amer. Geophys*. Union, **81**, F232.

Suttles, J. T., B. A. Wielicki, and S. Vemury, 1992: Top-of-atmosphere radiative fluxes: validation of ERBE scanner inversion algorithm using Nimbus-7 ERB data. *Journal of Applied Meteorology*, **31**, 784-796.

Su, H., E. F. Wood, H. Wang, and R. T. Pinker, 2008: Spatial and temporal scaling behavior of surface shortwave downward radiation based on MODIS and in situ measurements. *IEEE Geoscience and Remote Sensing Letters*, **5** (3), 542-546.

Tomita, H., M. Kubota, M. F. Cronin, S. Iwasaki, M. Konda, and H. Ichikawa, 2010: An assessment of surface heat fluxes from J-OFURO2 at the KEO and JKEO sites. *Journal of Geophysical Research,* **115**, C03018, doi:10.1029/2009JC005545.

Walsh, J. E., W. L. Chapman, and D. H. Portis, 2009: Arctic cloud fraction and radiative fluxes in atmospheric reanalyses. *Journal of Climate*, **22** (9), 2316-2334, doi:10.1175/2008JCLI2213.1.

Wang, H., 2007: Inferring Radiative fluxes from a new generation of satellites: Model Updates. Ph. D. dissertation. Department of Atmospheric and Oceanic Science, University of Maryland, College Park, MD. Advisor: Professor Rachel T. Pinker, Department of Atmospheric and Oceanic Science.

Wang, H., and R. T. Pinker, 2009: Shortwave radiative fluxes from MODIS: Model development and implementation. *Journal of Geophysical Research*, **114**, D20201, doi:10.1029/2008JD010442, 1-17.

Wang, X., and J. R. Key, 2003: Recent Trends in Arctic surface, cloud, and radiation properties from space. *Science*, **299**, 1725-1728.

Wang, X., and J. Key, 2005: Arctic surface, cloud, and radiation properties based on the AVHRR Polar Pathfinder data set. Part I: Spatial and temporal characteristics. *J. Climate*, **18** (14), 2558-2574.

Wang, X., and J. Key, 2005: Arctic surface, cloud, and radiation properties based on the AVHRR Polar Pathfinder data set. Part II: Recent trends. *J. Climate*, **18** (14), 2575-2593.

Wang, M., J. Overland, V. Kattsov, J. E. Walsh, X. Zhang, and T. Pavlova, 2007: Intrinsic verus forced variation in coupled climate model simulations over the Arctic during the 20th century. *J. Climate*, **20**, 1084-1098.

Wielicki, B. A., B. R. Barkstrom, E. F. Harrison, R. B. Lee III, G. L. Smith, and J. E. Cooper, 1996: Clouds and the Earth's Radiant Energy System (CERES): An Earth Observing System Experiment. *Bull. Amer. Meteor. Soc.*, **77**, 853-868.

Wielicki, B. A., 2005: CERES Status. This is a talk presented at a conference. In Aqua Status Meeting, 23 August, 2005, NASA HQ.

Wilks, D., 2006: Statistic Methods in the Atmospheric Sciences Academic Press. ISBN 13:978-0-12751966-1 (second edition) or ISBN 0-12-751966-1 (first edition).

Wiscombe, W. J., 1977: The delta-Eddington approximation for a vertically inhomogeneous atmosphere. Tech. Note TN-121+STR, National Center for Atmospheric Research, Boulder, CO, 66 pp.

Witze, A., 2008: Losing Greenland. *Nature*, **452**, 17 April 2008, 798-802.

Xiong, X., and W. Barnes, 2006: An overview of MODIS radiometric calibration and characterization. *Advances in Atmospheric Sciences*, **23** (1), 69-79.

Yannuzzi, V. T., E. E. Clothiaux, J. Y. Harrington, and J. Verlinde, 2009: Statistical analysis of forecasting models across the North Slope of Alaska during the Mixed-Phase Arctic Clouds Experiment. *Weather and Forecasting*, **24** (6), 1644- 1663, doi:10.1175/2009WAF2222218.1.

Zhang, J., D. Rothrock, and M. Steele, 2000: Recent changes in Arctic sea ice: The interplay between ice dynamics and thermodynamics. *J. Clim.*, **13**, 3099-3114.

Zhang, J., R. Lindsay, M. Steele, and A. Schweiger, 2008: What drove the dramatic retreat of arctic sea ice during summer 2007? *Geophysical research letters*, **35**, L11505, doi: 10.1029/2008GL034005, 1-5.

Zhang, T., T. Scambos, T. Haran, L. D. Hinzman, R. G. Barry, and D. L. Kane, 2003: Ground-based and satellite-derived measurements of surface albedo on the North Slope of Alaska. *Journal of Hydrometeorology*, **4**, 77-91.

Zhang, Y.-C., W. B. Rossow, and A. A. Lacis, 1995: Calculation of surface and top of atmosphere radiative fluxes from physical quantities based on ISCCP data sets: 1. Method and Sensitivity to input data uncertainties. *J. Geophys. Res.*, **100**, 1149-1165.

Zhang, Y.-C., W. B. Rossow, A. A. Lacis, V. Oinas, and M. I. Mishchenko, 2004: Calculation of radiative fluxes from the surface to top of atmosphere based on ISCCP and other global data sets: Refinements of the radiative transfer model and the input data. *J. Geophys. Res.*, **109**, D19105, doi: 10.1029/2003JD004457.